STARLING

39^{th} Annual VFS Student Design Competition

All-Electric Accessible VTOL Air Taxi

Sponsored by Bell

Alfred Gessow Rotorcraft Center
Department of Aerospace Engineering
University of Maryland
College Park, MD 20742 U.S.A.

UNIVERSITY OF MARYLAND

Alfred Gessow Rotorcraft Center
Department of Aerospace Engineering
University of Maryland
College Park, MD 20742

Matthew Arace
Graduate Student (Team Lead)
marace@umd.edu

Peter Ryseck
Graduate Student
pryseck@umd.edu

Paulo Arias
Graduate Student
pariasj@umd.edu

John Soong
Graduate Student
jsoong1@umd.edu

Akinola Akinwale
Graduate Student
aakinwal@umd.edu

Eric Greenbaum
Graduate Student
egreen98@umd.edu

Dr. Inderjit Chopra
Faculty Advisor
chopra@umd.edu

Dr. Vengalatore Nagaraj
Faculty Advisor
vnagaraj@umd.edu

Dr. Anubhav Datta
Faculty Advisor
datta@umd.edu

ENAE634: Helicopter Design (3 credits)

ACKNOWLEDGEMENTS

The design team wishes to acknowledge the following people for their invaluable discussion, guidance, and support throughout the course of this project.

Industry Professionals

Andreas Bernhard — Director, Aircraft Design at Sikorsky Aircraft

Ananth Sridharan — Principal, VTOL Analytics, LLC

University of Maryland Faculty

Dr. Inderjit Chopra — Distinguished University Professor and Alfred Gessow Professor, Director of Alfred Gessow Rotorcraft Center (AGRC), Department of Aerospace Engineering, University of Maryland, College Park

Dr. Vengalattore T. Nagaraj — Research Scientist, Department of Aerospace Engineering, University of Maryland, College Park

Dr. James D. Baeder — Professor, Department of Aerospace Engineering, University of Maryland, College Park

Dr. Anubhav Datta — Associate Professor, Department of Aerospace Engineering, University of Maryland, College Park

Alfred Gessow Rotocraft Research Center Graduate Students

Cheng Chi

Emily Fisler

Seyhan Gul

Dilhara Jayasundara

Ravi Lumba

Shashank Maurya

Mrinalgouda Patil

Abhishek Shastry

James Sutherland

Fredrick Tsai

Alfred Gessow Rotorcraft Center
Department of Aerospace Engineering
University of Maryland
College Park, MD 20742 U.S.A.

To the Vertical Flight Society:

The members of the University of Maryland Graduate Student Design Team hereby grant VFS full permission to distribute the enclosed Executive Summary and Final Proposal for the 39th Annual Design Competition as they see fit.

Thank you,

The UMD Graduate Design Team

Contents

List of Figures

List of Tables

RFP Deliverables and 14 CFR 29 Title 14 Compliance

RFP Deliverable	Source	Section
Trade Study	RFP	4
Aerodynamics	RFP	6, 10
Baggage Compartment	RFP	5, 11
	14 CFR 29.785	5
	14 CFR 29.787	5
Cabin and Accessibility	RFP	5, 11
	14 CFR 29.783	5
	14 CFR 29.785	5
	14 CFR 29.803	5
	14 CFR 29.807	5
	14 CFR 29.809	5
	14 CFR 29.811	5
	14 CFR 29.812	5
	14 CFR 29.813	5
	14 CFR 29.815	5
Cockpit	RFP	5, 13, 14
	14 CFR 29.771	5
	14 CFR 29.773	5
	14 CFR 29.775	5
	14 CFR 29.777	13
	14 CFR 29.779	13
Control System	RFP	13, 14
Electrical/Avionics	RFP	9, 14
Loads/Structures	RFP	5, 7, 8, 10, 11
	14 CFR 25.337	5
	14 CFR 25.341	11
	14 CFR 29.337	5
	14 CFR 29.341	11
	14 CFR 29.801	5
Mass Properties (mass, weight, inertia, etc.)	RFP	12
Performance	RFP	2, 16
Rotors	RFP	6, 7, 8

1 Introduction

Since Ubercab was founded in 2009 and sidecar launched its ride-share app in 2011, on-demand mobility and ride-sharing have become a common means of transportation at an affordable price. Concurrently, rapid advancements in Lithium batteries and permanent magnet motors by electric cars, mobile computing and autonomy by the cell phone industry, and manufacturing capabilities have brought to fruition the feasibility of electric aircraft. Together, a new market for vertical lift passenger transport has emerged. Electric vertical take-off and landing vehicles, eVTOL, have the potential to decongest cities, connect remote islands, de-carbonize aviation, and radicalize high speed transportation across city centers. However, it is imperative that they are made accessible to people of reduced mobility and supportive of individuals with different needs from the beginning. For equitable access, consideration must be taken during the conceptual design stage to incorporate meaningful, effective solutions to support people from all walks of life.

Figure 1.1: Collage of eVTOL

The successful manned flight of Solution F, the first manned electric helicopter, served as a catalyst for innovation in the industry [1]. Then the concept of distributed electric propulsion emerged with e-volo [2]. In the years that followed, eVTOL designs embraced the technology of distributed electric propulsion [3] which allowed electric power to be delivered cleanly to many rotors and get rid of the swashplate. Systematic study by NASA early on showed the limits of electric power [4]. It was clear that a new configuration built around electric power would be needed. What that configuration is remained unclear. Today, there are more than 500 eVTOL designs recorded by the VFS World eVTOL Aircraft Directory, some shown in Fig. 1.1. While these serve as a reminder that the best configuration is a strong function of the mission, more than the classical helicopter, many are serious contenders within the air-taxi marketplace. The market itself is highly valued. An outlook report by Morgan Stanley in 2021 projected a total market at $1 trillion [5]. At the same time, a joint report by Deloitte and Shell establishes the importance of de-carbonizing aviation, projecting that by 2050 aviation could contribute up to 22% of global greenhouse gas emissions [6]. Unfortunately, as it stands today aviation is omitted from the Paris Climate Agreement. Clean aviation is one of the enabling attributes of this market.

The other attribute is quietness. The insertion of aircraft into rural, suburban, and urban communities that fly at relatively low altitude has the potential to be wildly disruptive. Helicopters that hover at 80 dBA 300 ft above ground are a source of annoyance. An airspace saturated with noisy aircraft constantly flying overhead is not a pleasant prospect. It is crucial that this new class of aircraft be designed to be ultra-quiet from the start and blend into background noise to be accepted with open arms.

Urban insertion fundamentally changes the nature of passengers. They are no longer pre-planned travelers, but people with day to day needs. Trips may vary heavily from emergency services to regular commuters. The flexibility of the service will attract a diverse, vast base of constituents that the vehicles on market must be able to accommodate. Passengers with reduced mobility (PRMs) are but one example of this. To this day it is an arduous process for wheelchair bound individuals to travel via air. Standards and regulations do not represent their fundamental needs and this is a shortcoming that the eVTOL market can begin to rectify. There is an opportunity here for this new industry to be representative of all members of society whether disabled physically, cognitively, or visually. No one should be deemed too difficult to carry. It is necessary to apply a universal design mindset from the conceptual stage so that these vehicles are built around fundamentally inclusive features. If eVTOL are to emerge as mobility of the future, they must carry the entire community.

To adequately represent the end users, relevant stakeholders must be engaged early on in the design process to shed light on difficulties that the designers may otherwise overlook. To obtain insights on the challenges that persons with reduced mobility and other disabilities face, the team contacted and interviewed several personnel and campus organizations associated with disabilities. Their names are withheld but their needs are reflected in every aspect of the design. A common theme was that the best way to support a person with disability is to offer them independence and freedom in how they travel.

With their feedback *Starling* was conceived: A quad tiltrotor designed by the University of Maryland Graduate Design Team to provide clean, quiet, and efficient all-electric transport dedicated to carrying travelers of all abilities and afflictions with care and comfort.

The bird Starling, after which the aircraft is named, was first introduced by Shakespeare enthusiasts in Central Park, New York, in the late 19^{th} century. Today, it is one of the most common birds in the city. Their constant murmurations and mesmerizing patterns in the sky enthral New Yorkers and visitors alike. They are accomplished mimics capable of replicating car alarms, cell ringtones, and copying the sounds of other birds, even pets, to blend into the bustle of the city. Our *Starling* is inspired by these versatile vocalists.

2 Concept of Operations

The vision for Urban Air Mobility (UAM) is to revolutionize travel around greater metropolitan areas by enabling a safe, convenient, efficient, accessible and affordable method of air transportation. The Concept of Operations (ConOps) involved in a standard taxi mission is described below.

Pre-flight

At the departing flight location, the vehicle will be on standby while passengers are checking in to be approved for their flights. In the nominal 4 person configuration, the passengers will have their checked baggage loaded onto the vehicle, and will enter the cabin to find their desired seating. For the configuration with passengers with reduced mobility, the aircraft configuration will be readied beforehand based on special needs of the travellers, personal assistance will be provided by trained on-site personnel who will aid those who request support. Once the pilot has confirmed weather conditions are sufficient for flight departure will begin.

Takeoff and Vertical Ascent

Once the passengers are secured and the aircraft is cleared for takeoff, the rotors will started up and lift-off will commence. In ground effect hover will be entered for 10 seconds at 610 meters (2000 ft) above ground. The landing gear is then retracted. A vertical climb at 49 meters/minute will commence ending with out of ground effect hover at 640 meters (2100 ft) for 10 seconds.

Climb and Cruise Segment

Between the out of ground effect hover and the climb segment, the pylons will be tilted from 90°, helicopter mode, to 0°, airplane mode. This is the transition region. After transition, a steady climb at 9.46° will be established from 640 meters to 1219 meters (4000 ft). The flight paths will defer to local patterns dictated by air traffic or visuals. At 1219 meters, the aircraft will enter steady, level cruise at 200 km/hr (108 kts).

Descent and Landing

Descent will occur at an angle of 4° from the 1219.2 meter altitude down to 640 meters. After steady descent, the *Starling* transitions back to helicopter mode and an out of ground effect hover is held for 10 seconds. Vertical descent at 48.77 meters/minute is then initiated and the landing gear is deployed. Lastly, an in ground effect hover is held for 10 seconds followed by landing. Passengers will exit and claim their luggage. The operator will prepare the configuration for the next mission and the batteries will be recharged. Reconfiguration of the aircraft will not take more than 10 minutes and can be performed by on-ground personnel with standard equipment. Short turn around time and fast charging allow for a quick transition between flights.

3 Configuration Selection

3.1 Selection Structure

The RFP requests a vehicle that "accomplishes the mission in the most efficient manner." The vehicle must "be capable of continued safe flight following any single failure of the electrical power distribution system." This failure criteria has a strong impact on configuration selection as the vehicle must be capable of, essentially, completing the mission following a single point of failure. Additionally, minimum agility requirements are presented in steady flight and in the presence of gusts, requiring a high level of controllability.

Based on the mission requirements set forth in the RFP, configuration drivers were identified, and the Analytical Hierarchy Process (AHP) [7] was used to rank each driver relative to the other. Through this methodology, each team member individually constructed the AHP and obtained weight factors for the drivers. A discussion then took place until a consensus was reached amongst all members on the weight factors chosen, the result of which is shown in Table 3.1.

Following the AHP matrix, vehicle configurations were constructed. According to the VFS eVTOL Aircraft Directory, there are over 600 different vehicle configurations, each seeking to be the best configuration for eVTOL. The eVTOL market constitutes a diverse design space that seeks to take advantage of unique configurations that can be built around the electric drive. Therefore, a new methodology was developed to conjure vehicle configurations based on functional features. This is discussed in detail in the Configuration Downselect section.

Once a sufficient pool of vehicle configurations was identified, a Pugh Matrix [8] was constructed and used to score vehicle configurations based on the configuration drivers. Multiplying the scores with the weights of each configuration driver and summing each vehicle column provides the total value of each vehicle relative to the mission. The top three configurations are selected from this methodology for detailed design within the trade study.

3.2 Voice of the Customer/Selection Criteria

After studying the requirements set forth in the RFP, 12 distinct configuration drivers were identified and are presented below:

1. **Block Time:** This is the time from origin departure to destination arrival. Speed is vital because a more appealing ride service is one that carries passengers to their destination faster than cars and trains with a lower energy per distance per weight.
2. **Cruise Efficiency:** The Lift to Drag ratio of the aircraft that determines its cruise efficiency. Cruise is the longest mission segment, so the required energy is dictated by the cruise power. A key benefit of electric propulsion is the high motor efficiency at a wider range of RPM compared to a piston or turbine engine. The thrust requirement in forward flight is much lower than hover. By reducing the RPM of the rotor, higher blade loading is required to provide the same thrust, allowing operation at higher sectional C_l/C_d while reducing profile losses that scale with V_{tip}^3.
3. **Empty Weight:** The weight of the vehicle with no payload. A lower empty weight will reduce the total energy required throughout the mission and/or increase the payload capability of the vehicle.
4. **Hover Efficiency:** The power per unit thrust, or power loading. At any disk loading, power loading is maximized by maximizing Figure of Merit. The power required to hover is the highest power that dictates the design of the power plant.
5. **Safety and Crashworthiness:** The robustness of the onboard systems to failure and the exposure of the rotor to passengers and ground personnel are added levels of requirement beyond routine crashworthiness. Redundancy in electrical distribution systems are necessary to ensure continued operation following a potential failure. Additionally, passenger and ground operations safety is considered when entering and exiting the vehicle with rotors nearby. A high voltage system comes with the increased probability of battery fires, so available locations to place batteries away from passengers are prioritized.
6. **Lifecycle Cost:** The cost to design, manufacture, operate, and sustain the vehicle throughout its lifespan. Maintainability and reliability of the system ultimately drive its mechanical complexity.
7. **Gust Tolerance and Handling Qualities:** The ability of the aircraft to tolerate perturbations in airspeed and direction, particularly in urban microclimates with dynamic airflow patterns. A stable yet responsive aircraft is necessary to navigate the unpredictable wind patterns in cities. The presence of additional lifting surfaces increase the sensitivity to gusts. Sensors and software for autonomous collision avoidance are required. GNSS based landing and take-off cannot be relied on. Vision-based capabilities must be built in.
8. **Acoustics:** The success of an eVTOL in industry will be heavily impacted by its acceptance in the community [9]. Levels of community annoyance should consider more than just noise, including duration of exposure and frequency of disturbances. The aircraft's ability to blend into its operating environment is considered in terms of the magnitude and frequency of the noise it generates. Between 70-80 dB maximum in hover with a frequency >100 Hz is desirable to blend into the ambient noise of a city.
9. **Cabin Accessibility:** The flexibility to implement solutions to ease ingress and egress, particularly to support persons with disabilities. It is important to ensure adequate space up to and around the fuselage of the vehicle to allow for the implementation of supporting solutions.
10. **Ease of Certification:** The familiarity of the FAA and other regulatory agencies with the vehicle characteristics and weight class. eVTOL aircraft are still new, with current concepts varying greatly. Many operate both as an airplane and a helicopter. eVTOLs will not follow a traditional path for standard FAA Type aircraft certification. It is therefore desirable to design based on existing COTS technologies to ensure an easier path towards certification.
11. **Passenger Comfort:** The characteristics of the aircraft that affect the comfort of passengers are vibrations and internal acoustics of the cabin. Disabilities are not limited to physical restrictions. Passengers experiencing stress, anxiety, or hypersensitivity require a calm and reassuring interior

layout.

12. **CG Displacement:** The tolerance of the vehicle to longitudinal and lateral shift in the overall center of gravity. Different passenger and luggage configurations will shift the center of gravity away from the desired design point. The vehicle must be robust and capable of operation at the limits of this range.

3.3 Analytical Hierarchy Process (AHP)

The AHP was used to qualitatively rank the configuration criteria relative to each other in order to determine how heavily each ranking affects the configuration selection. Within the prioritization matrix, a value of > 1.0 indicates the criteria in the row is more important than the criteria in the column. Likewise, a value of < 1.0 indicates the criteria in the row is less important than the column. Rankings ranged from $\frac{1}{9}$, indicating the row is almost negligible relative to the column, to 9, indicating the row is exponentially more important than the column.

Table 3.1: Normalized weights from Analytical Hierarchy Process

	Block Time	Cruise Efficiency	Empty Weight	Hover Efficiency	System Safety & Crashworthiness	Lifecycle Cost	Gust Tolerance	Acoustics	Cabin Accessibility	Ease of Certification	Passenger Comfort	CG Displacement	Normalized Priority
Block Time	1.00	0.33	0.50	4.00	0.20	0.50	0.25	0.33	0.25	4.00	0.25	0.33	**0.0374**
Cruise Efficiency	3.00	1.00	2.00	5.00	1.00	2.00	1.00	1.50	1.00	5.00	1.00	1.50	**0.1128**
Empty Weight	2.00	0.50	1.00	4.00	0.33	1.00	0.25	0.33	0.33	4.00	0.33	0.50	**0.0496**
Hover Efficiency	0.25	0.20	0.25	1.00	0.14	0.20	0.17	0.20	0.20	1.00	0.20	0.25	**0.0179**
System Safety & Crashworthiness	5.00	1.00	3.00	7.00	1.00	3.00	2.00	2.00	2.00	6.00	2.00	2.50	**0.1667**
Lifecycle Cost	2.00	0.50	1.00	5.00	0.33	1.00	0.33	0.33	0.33	4.00	0.33	1.00	**0.0547**
Gust Tolerance	4.00	1.00	4.00	6.00	0.50	3.00	1.00	1.50	3.00	5.00	2.00	2.00	**0.1457**
Acoustics	3.00	0.67	3.00	5.00	0.50	3.00	0.67	1.00	1.50	5.00	2.50	2.00	**0.1183**
Cabin Accessibility	4.00	1.00	3.00	5.00	0.50	3.00	0.33	0.67	1.00	5.00	1.00	3.00	**0.1078**
Ease of Certification	0.25	0.20	0.25	1.00	0.17	0.25	0.20	0.20	0.20	1.00	0.17	0.25	**0.0186**
Passenger Comfort	4.00	1.00	3.00	5.00	0.50	3.00	0.50	0.40	1.00	6.00	1.00	2.00	**0.1038**
CG Displacement	3.00	0.67	2.00	4.00	0.40	1.00	0.50	0.50	0.33	4.00	0.50	1.00	**0.0668**

Table 3.1 shows the resulting normalized priority and Fig. 3.1 shows a graphical representation of the weights of each configuration criteria. All of these drivers were deemed important enough to impact the configuration selection. The highest weighted drivers are a combination of operating capability and passenger considerations, representative of the RFP. They define the key configuration characteristics that will mostly dominate the configuration selection.

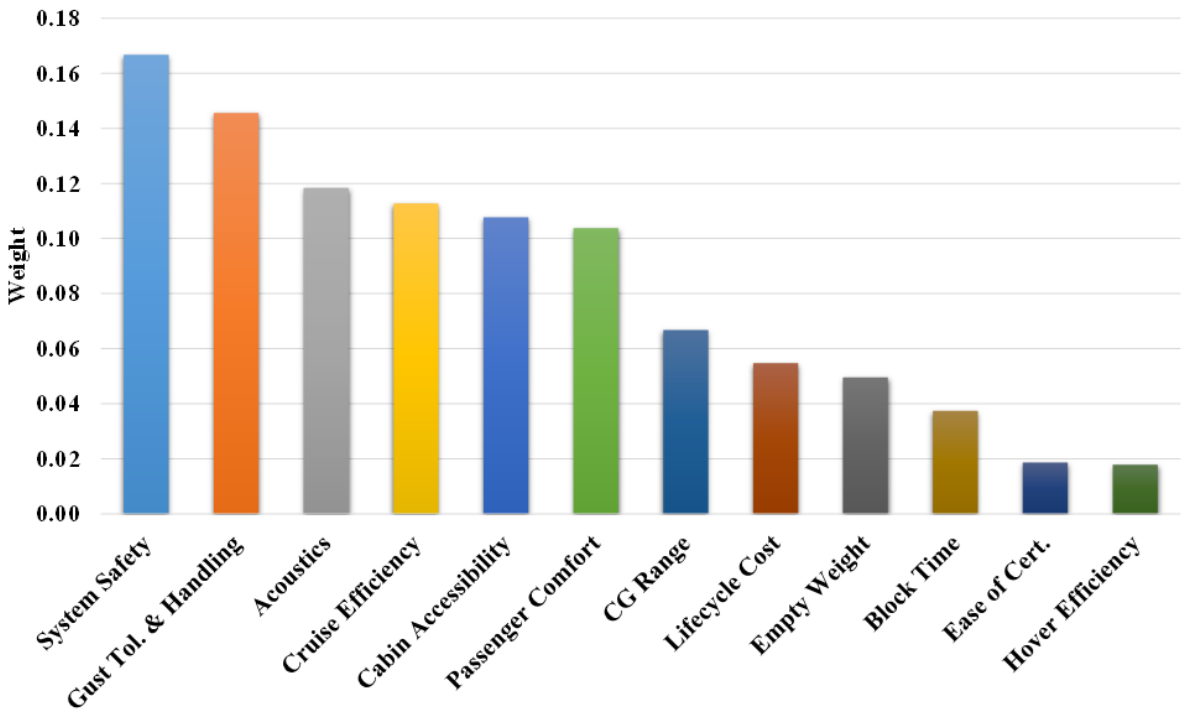

Figure 3.1: Relative ranking of configuration drivers

3.4 Configuration Composition

Distributed electric power opens the design space to configurations not previously conceivable. As a result, a new approach to generating a representative pool of configurations was deemed necessary to adequately capture every facet of the design space. Four primary categories of vehicle features were established, shown in Table 3.2. The resulting vehicle configurations are a combination of a single option from each category (column) e.g. no wing + single hub + single rotor + fixed shaft type results in a single main rotor. This process resulted in 54 potential vehicles.

Table 3.2: Possible configuration features

Wing	Number of Hubs	Rotor Type	Shaft Type
Fixed Wing	Single Hub	Stacked Rotor(s)	Fixed
Tilting Wing	Multiple Hubs	Single Rotor(s)	Transitioning
No Wing		Combination	Combination

Of the generated configurations, several were either physically impossible or duplicates. Fourteen final configurations were determined for consideration in the Pugh Matrix. In the qualitative comparisons, disk loading increases with an increasing number of side-by-side rotors due to the space constraint. The number of rotors is a design level decision and is left unspecified for the multi-rotor configurations. The vehicles considered in the Pugh Matrix and shown in Fig. 3.2 are the following:

1. **Single Main Rotor (SMR):** The single main rotor utilizes one main rotor for lift and propulsion as well as a conventional tail rotor to counter-balance the torque of the main rotor. This gold

Figure 3.2: Configurations considered

standard of efficient vertical lift is used as the baseline for all comparisons. The SMR is an excellent configuration for a long duration hover. However, a single point of failure may render the vehicle incapable of continued flight.

2. **Coaxial (two vertically offset counter-rotating rotors):** Relative to the SMR, the coaxial is more compact but has greater mechanical complexity and lower yaw control authority. The configuration also has lower forward flight efficiency at low speeds. The mast and hub structure is more complex and heavy, increasing empty weight and manufacturing cost. Due to natural anti-torque, a tail rotor is not needed.
3. **Tandem (two longitudinally offset counter-rotating rotors):** The tandem configuration is considered as it too provides natural anti-torque. It has a high tolerance for longitudinal CG displacement making it a good option to support a modular cabin. However, due to space constraints, an overlap would be necessary, reducing cruise efficiency from the increase in parasitic drag from raising the aft rotor. Vibrations will increase from additional rotor-wake interactions. Tandem provides an increase in available space surrounding the fuselage to implement supportive ingress and egress solutions.
4. **Multicopter (several distributed smaller rotors):** This vehicle consists of a fuselage body and

several smaller, distributed rotors with shafts that do not tilt. Distributing thrust to several rotors removes autorotation capability but increases the failure tolerance. The multicopter opens up more space for accessible solutions and provides easy anti-torque. Multicopters with four or more rotors also do not require swashplates as they can achieve lateral and longitudinal displacement through RPM variation alone. Distributed thrust has a favorable impact on vibrations, acoustics, and flight controllability, but its cruise efficiency is expected to suffer from the additional hub drag. Like cruise, hover efficiency is expected to suffer from space constraints, decreasing available lifting area and increasing disk loading. Thrust distribution gives a high tolerance to CG displacement.

5. **Single Main Rotor Lift Compound (SMR with full or half fixed wing):** The lift compounded SMR has increased cruise efficiency relative to the conventional SMR but is more susceptible to gusts from the additional surface area. The addition of a wing adds weight and takes away from the available fuselage area to support ingress and egress. A high wing configuration is not possible. It reduces vibrations in forward flight by unloading the main rotor, and there is no stall speed due to the main rotor. Maryland hover and wind tunnel tests have revealed download on the wing would add up to 3% to the thrust [10]. The lift compound benefit is realized at high speeds.
6. **Coaxial Thrust Compound (Coaxial with pusher propeller):** Adding a propeller to the coaxial configuration unloads the rotor from providing propulsive force, allowing for higher speed forward flight until Mach effects on the advancing sides of the main rotors become significant. No benefit is expected at lower speeds. The propeller adds to the noise generated in cruise and increases maintenance.
7. **Single Main Rotor Lift & Thrust Compound (SMR with full wing and pusher propeller):** A lift and thrust compounded SMR greatly increases the forward flight efficiency if the rotor speed is reduced by at least 20%. However, a tail rotor is still required in hover for anti-torque, which can be swiveled into a propeller for cruise. This is a very complex system. With the wing producing lift and a propeller producing thrust, the main rotor has no other function in forward flight than generating drag.
8. **Coaxial Lift & Thrust Compounded (Coaxial with full wing and pusher propeller):** Similar to the lift and thrust compounded SMR, the speed and forward flight efficiency of the vehicle is increased. Adding a wing adversely impacts gust tolerance and cabin accessibility but reduces vibrations from oscillatory loading in forward flight.
9. **Tilt-Rotor (Fixed wing with rotors that tilt forward from hover to forward flight):** Wing mounted rotors can be away from passengers and ground personnel. Like a multicopter, several rotors share lift and thrust which is expected to have a favorable impact on vibrations and acoustic profile from the reduction in loading per rotor. Tilting mechanisms add weight and complexity, but conversion to airplane mode increases L/D greatly. The wing has a negative impact on gust tolerance, but can be compensated by controllability and resilience to perturbations that distributed thrust provides [11]. A compromise between Figure of Merit and propulsive efficiency can be eliminated if rotor speeds can be reduced significantly. Tilt-rotors have the potential for very high speeds, until air resonance or whirl flutter boundaries are encountered. Civilian-grade tiltrotors, both conventional and electric, have either received certification (Joby S4) or are close to achieving it (AW609).
10. **Tilt-Wing (Tilting wing with distributed rotors that tilt with the wing:** Gaining all the benefit from distributed thrust, the wings tilting with rotors reduces the download in hover. With higher expected disk loading, hover Figure of Merit is still significantly less than a single main rotor helicopter. A major disadvantage of the tilt-wing vehicle is the large wing surface area in hover makes the vehicle quite susceptible to perturbations in yaw where there is already limited control. Tilting mechanisms are heavy and complex, and wing structural weight is increased. Wing stall in transition adds additional complexity. The tilt-wing comes with additional wing aeroelastic complexities as

well.

11. **Tilt-Wing with Fans-in-Wing (Tilting wing with ducted fans embedded into the wing):** The rotors are small fans embedded into the wing structure. The ducts provide a significant acoustic benefit by preventing noise from traveling in the in-plane rotor direction. A noticeable benefit to cruise efficiency is expected as well. The disk loading of this vehicle is expected to be quite high with the extremely limited space to place the rotors, adversely impacting hover performance.
12. **Fixed Wing + Fixed Lift Rotors + Fixed Cruise Rotors (Fixed wing with fixed rotors for lift and fixed propellers for cruise):** The first of the "combination" fixed wing configurations makes use of rotors and propellers that do not transition between hover and forward flight. The vehicle takes off vertically using the lifting rotors with the cruise propellers off. To transition, the cruise propellers spin up and the wing begins to generate lift as the aircraft gains speed. Once the vehicle passes stall speed, the lifting rotors are stopped in flight in an orientation to reduce drag. The advantage here is that each rotor and propeller can be optimized for their respective flight conditions without compromising Figure of Merit or propulsive efficiency. The drawback is the additional drag generated from the stopped lifting rotors in forward flight. The final three configurations are all quite similar and are expected to provide high cruise efficiency, a favorable acoustic profile, high system redundancy, and favorable passenger focused rankings. They all have mediocre gust tolerance.
13. **Fixed Wing + Fixed Lift Rotors + Tilting Cruise Rotors (Fixed wing with some fixed rotors for lift and additional rotors that tilt forward from hover to forward flight):** Similar to the previous configuration, a fixed wing and fixed lifting rotors are maintained. However, there are no fixed cruise propellers. Some rotors having tilting capability and transition from lifting rotors in hover to axial propellers in cruise. The advantage of this vehicle is that fewer rotors can be utilized and the number of unused motors and rotors in each flight segment is reduced. However, the tradeoff is the rotor efficiency compromise between hover and forward flight as forward flight efficiency demands high twist and Figure of Merit does not.
14. **Fixed Wing + Fixed Cruise Rotors + Tilting Cruise Rotors (Fixed wing with some fixed rotors for cruise and additional rotors that tilt forward from hover to forward flight):** The final configuration is considered for completeness. The only distinction between this and the previous configuration is fixed cruising propellers in place of fixed lifting rotors. The main advantage is that in forward flight, there are no unused rotors generating drag. The disadvantage is there are unused rotors in hover, increasing disk loading and subsequently power required to hover.

3.5 Pugh Matrix

The Pugh matrix was constructed to rank the configurations with respect to the configuration drivers. Table 3.3 shows these results. Rankings were given in integer values from -4 (very bad) to 4 (very good) with respect to the SMR.

The lift and thrust compounded SMR was determined to be the least effective solution to the mission relative to the configuration drivers. Despite the improvement to cruising efficiency and block time, almost every other metric was reduced due to the addition of the wing and propellers. The highest ranked configurations from the Pugh matrix are: (1) Multicopter, (2) Tiltrotor, and the (3) Fixed wing + fixed lift rotors + fixed cruise rotors configuration which will be studied further. From here on, the fixed wing + fixed lift rotors + fixed cruise rotors will be referred to as the **Stopped Rotor**.

Table 3.3: Pugh Matrix

	Weight	SMR	Coaxial	Tandem	Multicopter	SMR Lift Compounded	Coaxial Thrust Compounded	SMR Lift + Thrust Compounded	Coaxial Lift + Thrust Compounded	Tilt-Rotors	Tilt-Wings	Fixed Wing + Fixed Lift Rotors + Fixed Cruise Rotors	Fixed Wing + Fixed Cruise Rotors + Tilting Cruise Rotors	Fixed Wing + Fixed Lift Rotors + Tilting Cruise Rotors	Tilt-Wing with Fans-in-Wing
System Safety & Crashworthiness	0.1667	0.00	1.00	2.00	1.00	0.00	0.00	0.00	0.00	2.00	-1.00	2.00	2.00	2.00	0.00
Gust Tolerance & Handling Qualities	0.1457	0.00	1.00	1.00	2.00	-1.00	1.00	-1.00	0.00	1.00	-1.00	1.00	1.00	1.00	0.00
Acoustics	0.1183	0.00	1.00	0.00	2.00	1.00	0.00	-1.00	1.00	2.00	3.00	3.00	2.00	2.00	2.00
Cruise Efficiency	0.1128	0.00	-1.00	-1.00	-1.00	1.00	0.00	2.00	1.00	3.00	3.00	3.00	4.00	3.00	3.00
Cabin Accessibility	0.1078	0.00	1.00	2.00	2.00	-1.00	0.00	-2.00	-2.00	2.00	-1.00	-2.00	-1.00	0.00	0.00
Passenger Comfort	0.1038	0.00	-1.00	-1.00	2.00	1.00	0.00	1.00	1.00	2.00	1.00	2.00	2.00	2.00	3.00
CG Range	0.0668	0.00	0.00	2.00	3.00	0.00	0.00	0.00	0.00	2.00	2.00	1.00	1.00	1.00	1.00
Lifecycle Cost	0.0547	0.00	-2.00	-2.00	3.00	0.00	-2.00	-1.00	-2.00	-2.00	-3.00	2.00	-1.00	-1.00	-3.00
Empty Weight	0.0496	0.00	0.00	-1.00	0.00	-1.00	-1.00	-2.00	-2.00	-2.00	-2.00	-1.00	-1.00	-1.00	-2.00
Block Time	0.0374	0.00	0.00	1.00	0.00	1.00	2.00	2.00	3.00	4.00	4.00	3.00	4.00	3.00	3.00
Ease of Certification	0.0186	0.00	-1.00	-1.00	-2.00	0.00	-1.00	-1.00	-1.00	-2.00	-3.00	-1.00	-2.00	-2.00	-3.00
Hover Efficiency	0.0179	0.00	2.00	1.00	-1.00	-1.00	2.00	-1.00	1.00	-3.00	-2.00	-2.00	-3.00	-2.00	-4.00
	Total Score	0.00	0.23	0.49	1.31	0.05	0.08	-0.27	0.02	1.46	0.31	1.35	1.29	1.26	0.67

4 Configuration Trade Studies

Out of the configuration selection, *Starling* emerged as a design with a high level of safety, quietness, and cruise efficiency. The top three configurations, the multicopter, tiltrotor, and stopped rotor, are now considered for further in-depth analysis. At this stage, the number of rotors for each configuration has yet to be determined. For the sake of visualization Fig. 4.1 shows a simple sketch of each configuration as they are sized in the end. Further trade studies were conducted to fully define each configuration and make a final selection for detailed design.

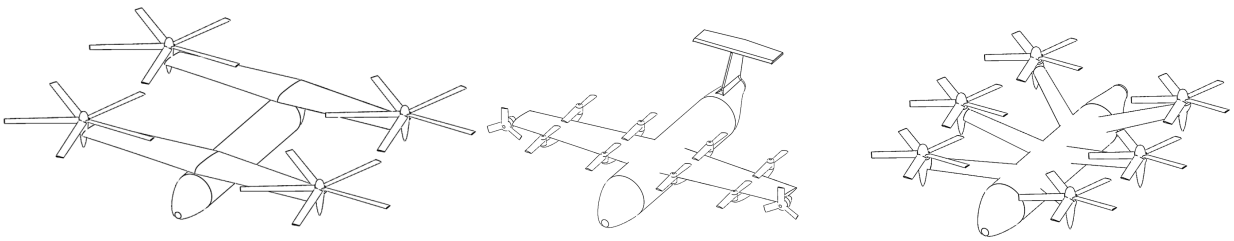

(a) Tiltrotor (b) Stopped Rotor (c) Multicopter

Figure 4.1: Three configurations selected for further trade study

4.1 Preliminary Vehicle Sizing

Initial vehicle sizing for all three configurations was performed using in-house sizing codes developed by the team. The codes all use a modified version of momentum theory to calculate the aerodynamic performance of the rotors. The U.S. Army Aeroflightdynamics Directorate (AFDD) weight model [12] was

used for traditional components whereas new in-house models were used for eVTOL-specific electric power components such as motors and avionics. Trade studies were performed to better understand how rotor design parameters affected aircraft weight and performance. In addition, the tiltrotor and stopped rotor configurations explored additional wing- and propeller-related parameters.

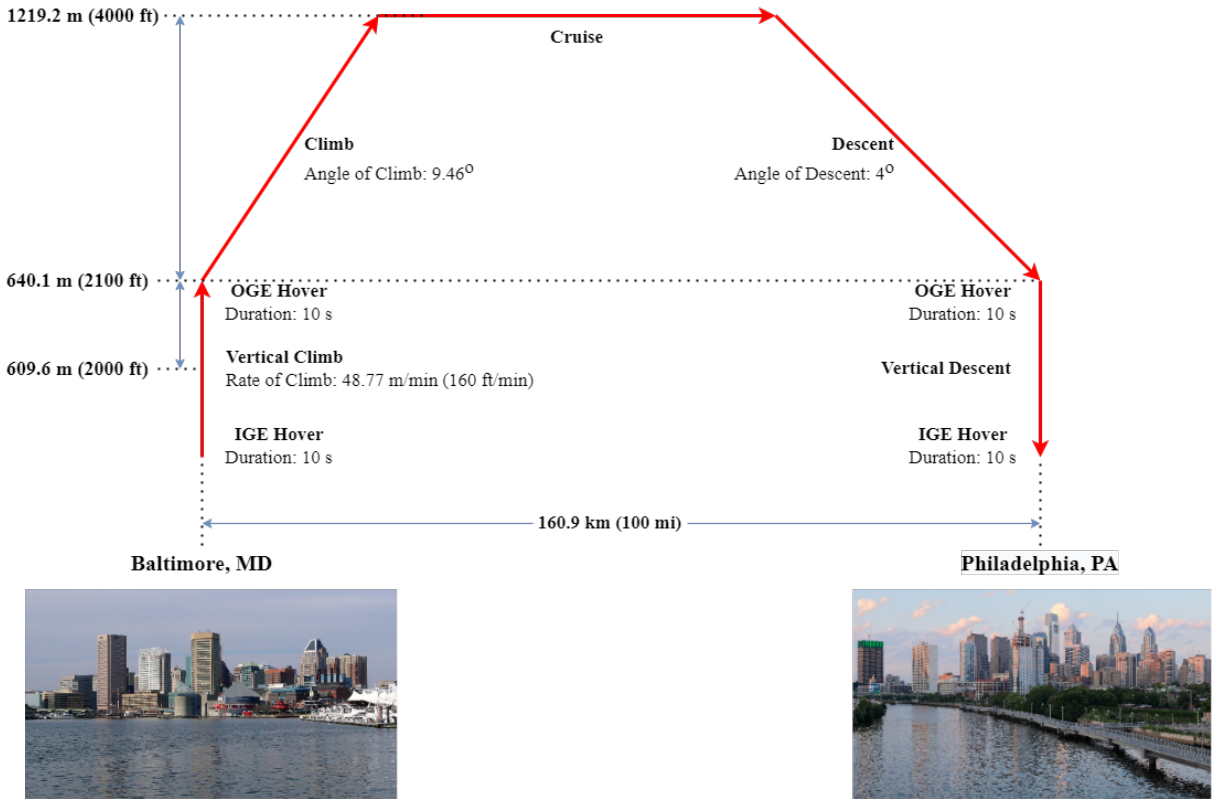

Figure 4.2: Mission profile between two cities.

4.1.1 Mission Profile

The sizing mission, shown in Figure 4.2, is based on a one-way trip between two cities set 160.9 km (100 mi) apart. Baltimore (Maryland) and Philadelphia (Pennsylvania) were used as examples. From the specified angles of climb and descent, the horizontal distance traveled in climb and descent ideally is 3.48 km (2.16 mi) and 8.29 km (5.15 mi), respectively. As a result, the distance needed to travel in cruise is 149.2 km (92.7 mi). However, this range credit is discarded. Cities and airports have unique takeoff and landing patterns due to building layouts or airspace restrictions (such as Washington, D.C. restricted airspace). As a result, the cruise distance could be as long as the full 160.9 km (100 mi) specified by the mission profile. The mission also accounts for reserve energy equivalent to twenty minutes of cruise.

Each configuration operates at a different target cruise speed based on configuration drag area, resulting in different flight times. The climb and descent speeds were the best endurance speeds, which is with the minimum power speed [13]. Flying at minimum power also provides the maximum power margin for additional climb-descent maneuvers. The cruise speed is the best range speed. Table 4.1 shows the estimated trip time for the three configurations. The estimated times for vertical climb and hover were neglected from this calculation because they are small enough to not significantly contribute to the overall trip time.

Each vehicle was designed to carry a payload of four able-bodied passengers, the pilot, and the baggage

Table 4.1: Climb speed, cruise speed, and total trip time for three configurations

Configuration	Climb (km/hr)	Cruise (km/hr)	Time (hr:min)
Tiltrotor	159.8	205	0:50
Stopped rotor	150.9	199.3	0:51
Multicopter	94.9	140.8	1:14

(checked, carry-on, and personal). Although a weight representative of the 95^{th} percentile would have provided the maximum passenger load-case scenario, it was reasoned that the urban air taxi service would attract a wide range of weight types such that a random selection of four passengers, including children, from a random city would have weights that would average close to 80.7 kg (177.9 lb), the average weight of a North American human [14]. The combined payload weight came out to be 554.1 kg (1221.5 lb); however, a payload weight of 589.7 kg (1300 lb) was specified to account for:

1. expected increase in human average weight [15]
2. differences due to regional obesity as documented by the CDC [16]

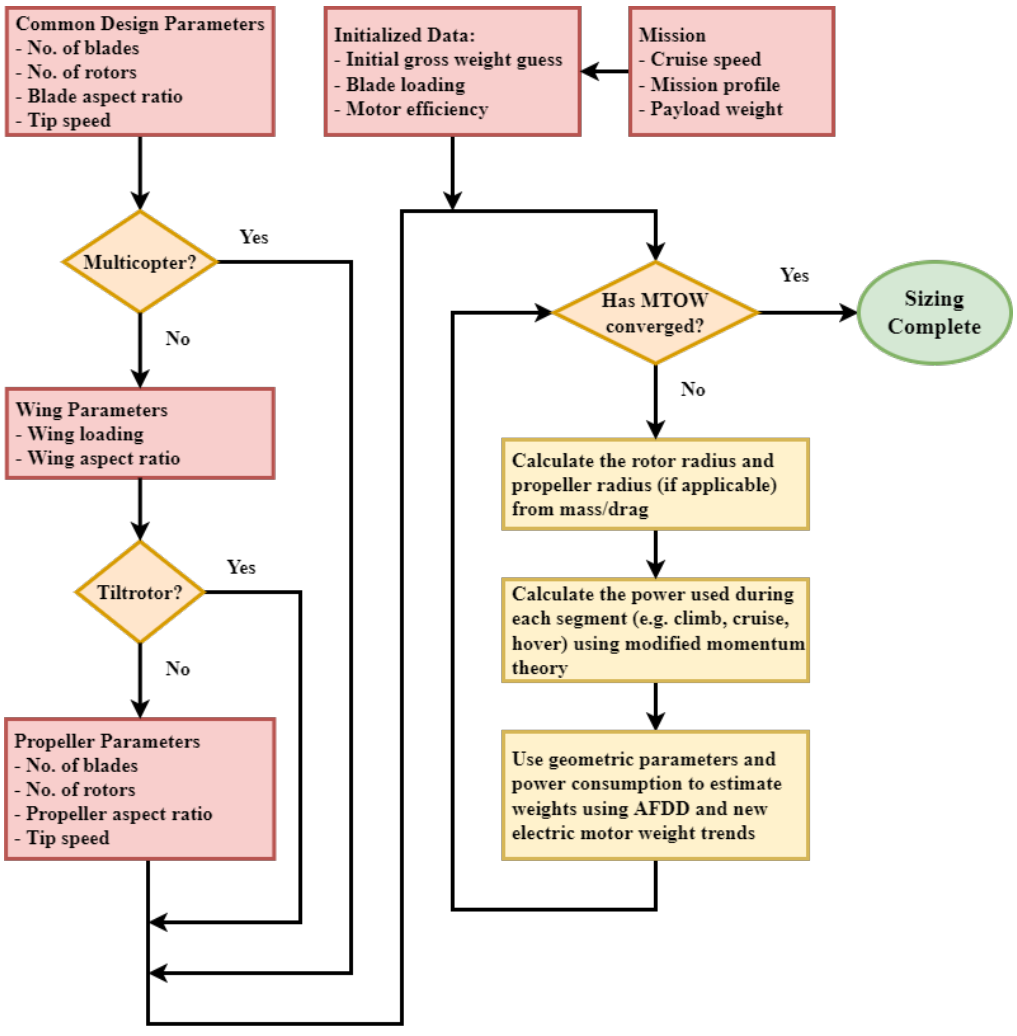

Figure 4.3: Flowchart for the configuration sizing procedure

4.1.2 Sizing Algorithm

The configuration sizing algorithm is depicted in Figure 4.3. The algorithm takes mission parameters, design parameters, and initialized variables. Additional parameters were added based on the individual configurations. The mission profile included ISA + 20°C for each segment. The initial gross weight estimate was inputted as a variable used for sizing iteration convergence. The blade loading for each configuration is set to a constant value that avoids the onset of stall during normal vehicle operation, which includes various maneuvers and potential gust interactions. The motor efficiency was set to 0.9. Thus, it was assumed that all three configurations use the exact same motors.

Once the inputs are specified, the gross weight was iterated. Within the loop, required power was calculated for each leg of the mission using momentum theory. Section 14 estimated that the avionics and HUMS suites would consume approximately 1.4 kW (1.88 HP), so this power consumption was factored into the power required for each mission segment. For configurations that enter forward flight using fixed lifting surfaces, the power requirement is dominated by the fuselage and wing drag. The fuselage drag in the forward flight legs of the mission uses the Harris trend with the exponent increased from 2/3 to 0.7263 based on previous Maryland VFS design experience.

$$F = f\left(\frac{W_{lb}}{1000}\right)^{0.7263} ft^2 \tag{1}$$

The variable f is the Harris drag factor. Typically $f = 2$ is for helicopters with retractable landing gear and $f = 1.5$ for tiltrotors. Much like the tiltrotor, the stopped rotor lift in cruise is generated entirely from its wings; however, the stopped rotors increase the overall fuselage drag. As a result, a drag factor of 1.75 is used.

The results of the performance analysis were then passed into a subroutine that estimated the weights of various components. The motor weights were sized based on the expected motor torque as shown in Equation 5 in Section 4.6.1. The sizing looped until the gross weight converged.

4.2 Design Drivers

Four design drivers influenced the qualitative evaluation of different configurations for each vehicle type. These drivers were a mixture of dimension restrictions and performance metrics. Other design considerations such as noise were considered in the down-selection process later. The final sizing decision for each vehicle configuration involved an extensive sweep of number of blades, number of rotors, blade aspect ratio, rotor tip speed, and other configuration-specific parameters. Specific trade studies on electric motors is covered in greater depth in Section 9.

4.2.1 Blade Loading

Blade loading C_T/σ is non-dimensional lift per blade area. The McHugh stall boundary ([17], Figure 1) predicts that rotor blades begin to stall in hover when $C_T/\sigma = 0.16$. A blade loading of $C_T/\sigma = 0.12$ is set as the target value to allow for ample margin during forward-flight transition as well as sufficient control authority under gusts. In edgewise flight, the blade loading stall limit decreases significantly at higher advance ratios. For example, at advance ratio $\mu = 0.3$ the stall $C_T/\sigma \approx 0.12$. Thus, the multicopter assumed a lower target value of $C_T/\sigma = 0.1$ to avoid retreating blade stall in forward flight. The blade loading limit was directly enforced by changing chord as gross weight varied.

4.2.2 Disk Loading

Disk loading is the ratio of a rotor thrust to area. High disk loading results in high downwash. Higher downwash could cause unsafe environment for both ground staff and passengers by dislodging dust and debris. In addition, a higher disk loading contributes to an increase in noise generated by the aircraft, which is antithetical to the benefits of eVTOL. Thus, the configurations aim to minimize rotor disk loading.

4.2.3 Rotor Diameter and Wingspan

The requirement that the entire vehicle must fit within a 15.24×15.24 m (50×50 ft) box places a physical constraint on number and size of the rotors and, if applicable, wing design. The use of distributed electric propulsion enables the use of multiple rotors. Depending on how these rotors are arranged, the vehicle may exceed the box dimensions; however, maximizing rotor radius as much as possible was still desired. For vehicle configurations with wings, the wingspan is constrained to be at most 50 feet. The maximum wing span of the tiltrotor considered the rotor placement at the tip, so the maximum span was 50 feet minus one rotor diameter. The stopped rotor assumed a similar rationale except with propellers at the wing tips. As a result, the maximum stopped rotor wingspan was $15.24 - 2R$ m ($50 - 2R$ ft) where R is the propeller radius.

4.3 Configuration 1: Tiltrotor

The sizing for the tiltrotor depends on two sets of design parameters: one for the rotor and another for the wing. The vehicle size constraint forces a delicate trade between the size of rotors and wings. When transitioning into a forward-flight configuration, the tiltrotor reduces the rotor tip speed and RPM to increase the blade lift coefficient as the primary force changes from weight to drag. As a result, performance studies were also conducted to find a suitable tip speed reduction for high propeller efficiency in cruise.

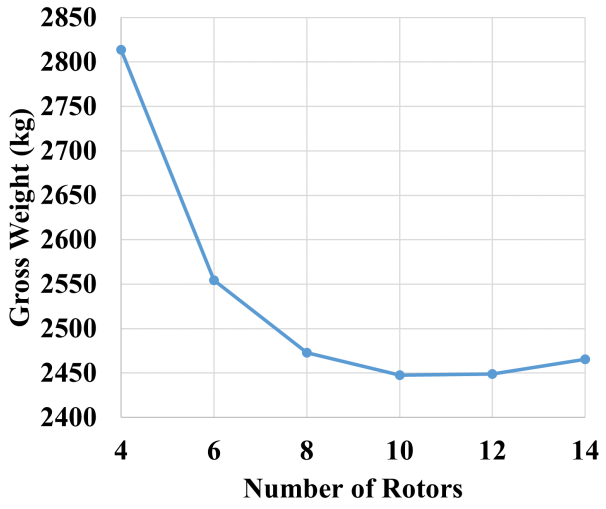

(a) Gross weight versus number of rotors

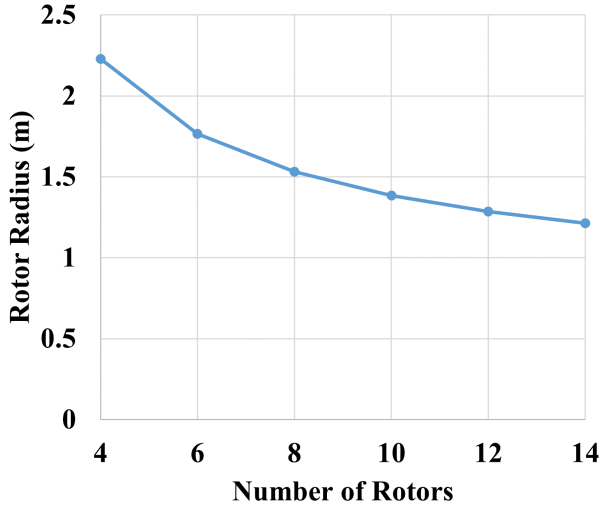

(b) Rotor radius versus number of rotors

Figure 4.4: Parametric study on number of rotors. All rotors assumed to have no cyclic

4.3.1 Number of Rotors

Distributed electric propulsion that most eVTOL use requires that the vehicle have multiple main rotors to generate rotary-wing lift. The first parametric study performed was the number of rotors since their placement, especially the tilting ones, would add mechanical complexity and weight downstream. The trade studies were performed assuming a flap frequency of $\nu_\beta = 1.15$/rev.

Holding all other design parameters fixed, Figure 4.4 show the results from the sizing code with increasing number of rotors. Only even-numbered rotors were swept to ensure yaw moment balance. Odd-numbered of rotors have been used on micro air vehicles (MAVs); however, their yaw control are not robust enough to implement on passenger rotorcraft [18]. Increasing the number of main rotors decreased both the gross weight and rotor radius. In practice, this trend is reversed due to additional support structures including inter-connecting shafts. Not all of these support structures may be required for an electric drive, so the weight benefit can perhaps be realized. Eventually, the gross weight begins to increase at higher rotor numbers. However, long before the number 10 is reached, the weight of the support structure is expected to turn the trend adversely. Results from the sizing code showed 6 and 8 rotors caused the design to fall outside the geometric space limits. Thus, four main rotors was the solution.

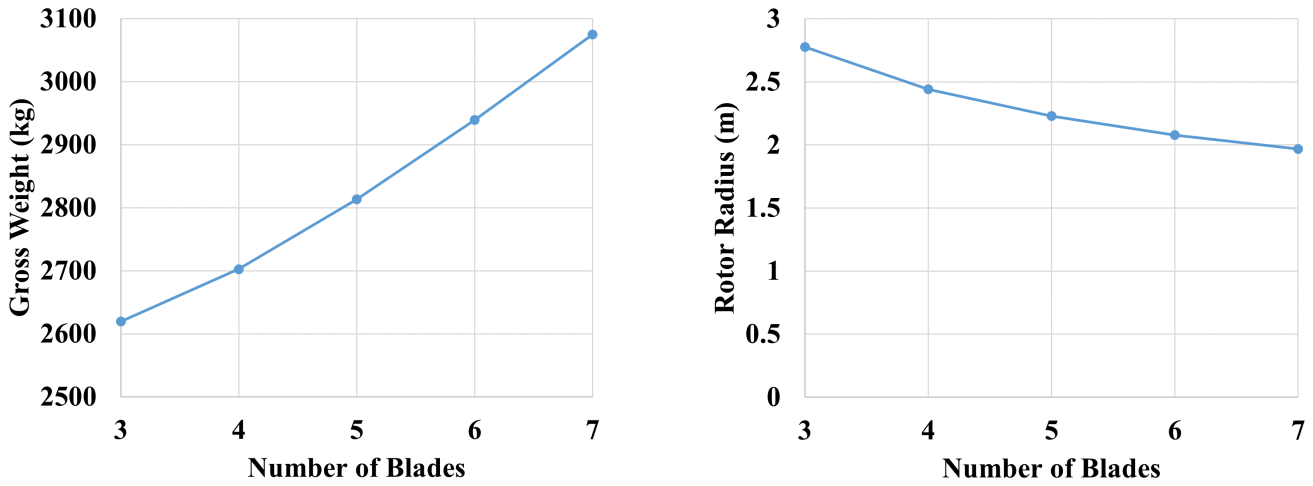

(a) Gross weight versus number of blades N_b

(b) Rotor radius versus number of blades N_b

Figure 4.5: Parametric trade study on number of blades

4.3.2 Number of Blades (N_b)

After the optimal number of main rotors was examined, a trade study on number of blades (N_b) was performed. As shown in Figure 4.5, increasing N_b increases gross weight but decreases the rotor radius. Assuming that the rotors were to be placed at the wing tip, the decrease in rotor radius would yield more flexibility in wing sizing downstream. It is well-known that increasing the number of blades reduces the propeller's loading noise [19]. It also pushes the blade passage frequency higher. Since noise was a key driver, $N_b = 5$ was selected to allow blending into the urban soundscape.

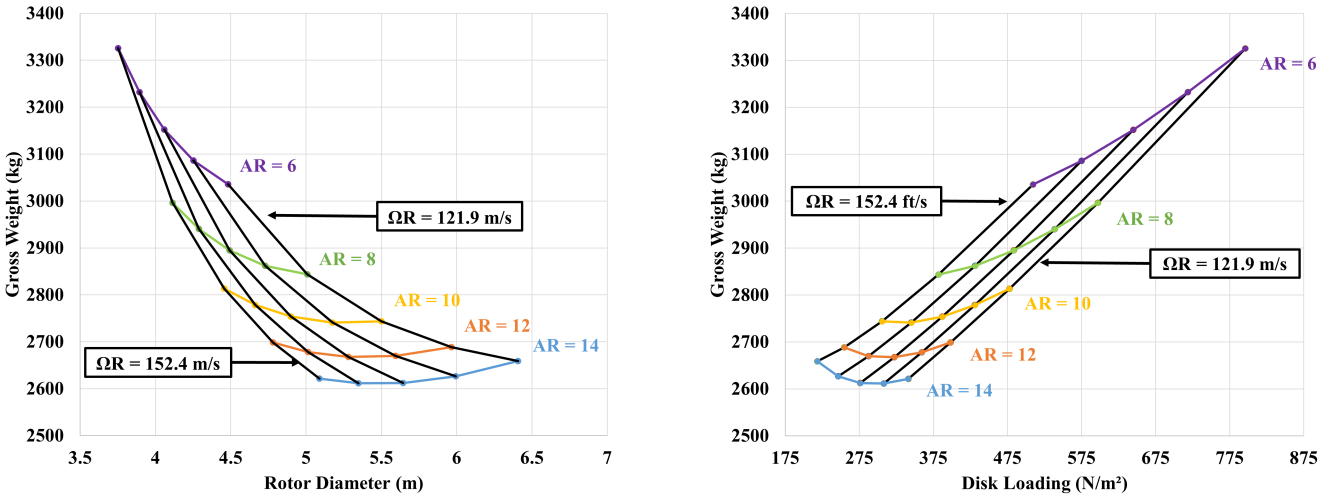

(a) Gross weight versus rotor diameter for varying AR and tip speed

(b) Gross weight versus disk loading for varying AR and tip speed

Figure 4.6: Parametric trade study on number of blades

4.3.3 Blade Aspect Ratio and Tip Speed

With the number of rotors and N_b settled, the rotor tip speed and aspect ratio were varied simultaneously to understand their effects on the vehicle disk loading, radius, and gross weight. The selected tip speed range was motivated by the desire for lower noise production in urban environments. Johnson [20] shows significant noise reduction around a tip speed of 137.2 m/s (450 ft/s), so tip speeds between 121.9 to 152.4 m/s (400 to 500 ft/s) were examined closely. Lowering the tip speed also increases the coefficient of thrust C_T which also increases the Figure of Merit.

The blade loading C_T/σ was enforced to be 0.12, so an increase in C_T requires a corresponding increase in rotor solidity. With the value of N_b set, the rotor solidity, defined as $\sigma = N_b/\pi AR$ can be increased by decreasing aspect ratio. The use of below-average tip speeds necessitates examination of solidity values that are above-average, so an aspect ratio range from 6 to 14 was swept. The trend mentioned by Johnson is visible at higher aspect ratios, so a nominal tip speed target of 137.2 m/s (450 ft/s) was selected. Lower aspect ratios significantly increase the vehicle weight, which is expected as increasing solidity increases the profile. An aspect ratio of 12 corresponding solidity $\sigma = 0.13$ was selected.

4.3.4 Wing Loading and Aspect Ratio

With the rotor fixed, Figure 4.7 shows a trade study involving wing loading and wing aspect ratio by plotting gross weight against cruise efficiency index. The cruise efficiency index is defined as the lift-to-drag per unit of power, so a higher index would warrant less power expenditure from the electric motors, thus extending battery life. At a given weight, a higher wing loading would reduce the overall wing area, which is useful in increasing the gust tolerance. The XV-15 wing loading was between 2969 and 4022 N/m^2 (62 lb/ft^2 and 84 lb/ft^2) at cruise speeds of 370 km/hr (200 kts, 230 mph). However, flying at a much lower cruise speed of 206.9 km/hr (111.7 kts, 128 mph) would call for a much lower wing loading. A wing loading range of 958 to 1532 N/m^2 (20 to 32 lb/ft^2) was examined. A higher aspect ratio improves cruise efficiency, but the placement of rotors outboard means that the wing must be structurally stiff to support the tilting nacelle, which favored lower aspect ratio. With these considerations, an aspect ratio of 6 and wing loading of 957 N/m^2 (20 lb/ft^2) was selected.

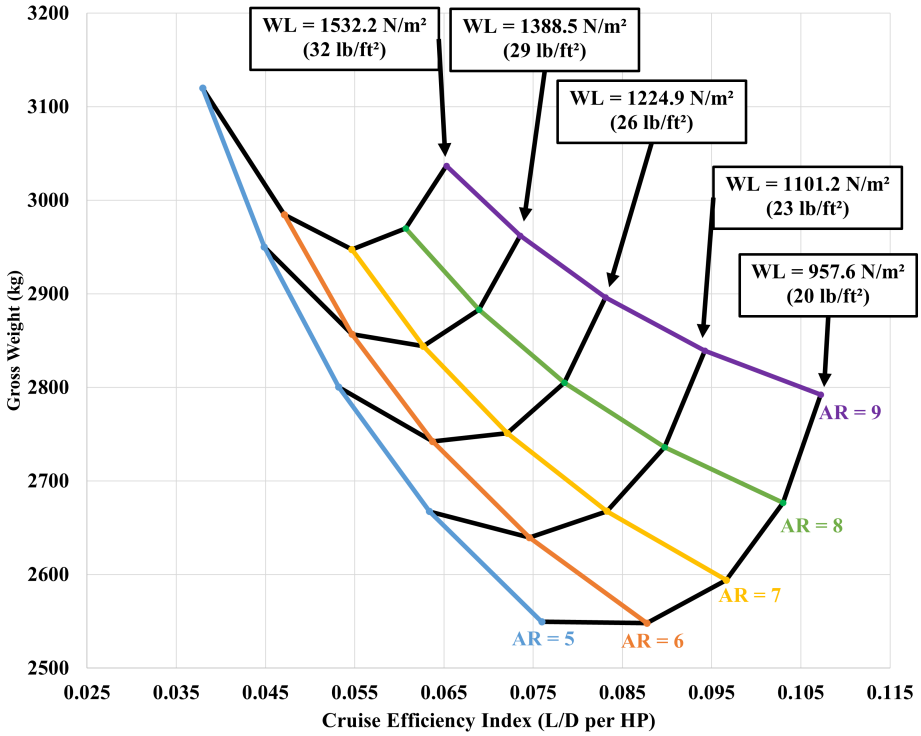

Figure 4.7: Gross weight and cruise efficiency versus wing loading and wing aspect ratio

The chosen combination of aspect ratio and wing loading resulted in a wingspan of 12.5 m (41 ft). Adding the rotor system to the wing tip would cause the vehicle width to exceed the dimension specifications. Thus, the wing was split into two wings – front and back. The reduced wing span for each wing is 8.84 m (29.0 ft). With the rotors added, the new vehicle width is about 46 ft. The two wings eliminate the need for a horizontal tail for longitudinal moment balance. Yaw control can be achieved by varying the thrust on each rotor via collective control. The omission of stabilizers also eliminates power that would have been otherwise consumed by the rudder and elevators.

4.3.5 Thrust and Power Coefficients

Trade studies on twist and inflow ratio were performed using an in-house blade element momentum theory (BEMT) code that is detailed later in Section 6. Figure 4.8 shows the effects of twist and inflow variation on thrust and power coefficients. Since cruise velocity is specified, cruise inflow was varied by dropping tip speed. Figure 4.8(a) shows C_T versus C_P. Figure 4.8(b) shows C_T/C_P versus inflow ratio. However, the proper metric is propeller efficiency $\eta_p = C_T\lambda/C_P$. Figure 4.8(c) shows the propeller efficiency. It shows decreasing tip speed increases propeller efficiency at all values of twist rate. This trend helps establish that a λ of 0.98 would allow the tiltrotor to operate at a propeller efficiency near 0.8 for high values of twist rate. This corresponds to a cruise tip speed of 60.96 m/s (200 ft/s), a 55% reduction from hover. At the same time adequate collective was ensured. Figure 4.8(d) shows how the hover Figure of Merit varied with twist rate. The values are somewhat higher than typical, but this is a result of the low tip speed.

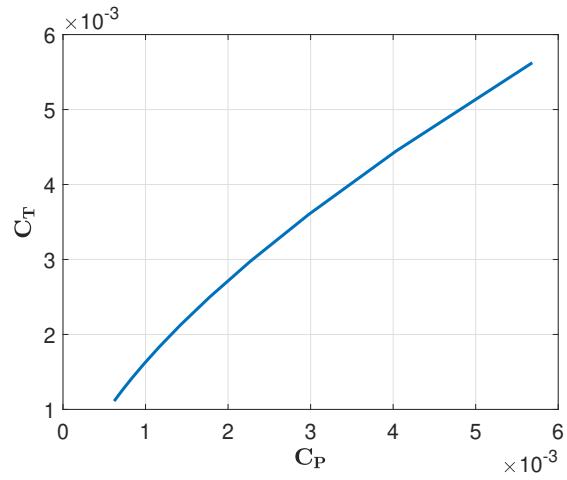

(a) C_T versus C_P

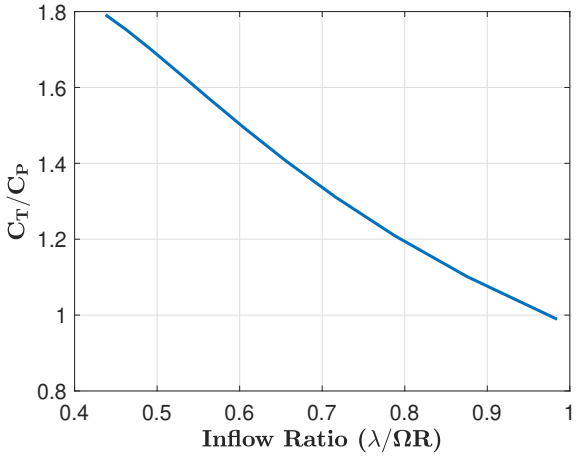

(b) C_T/C_P versus λ

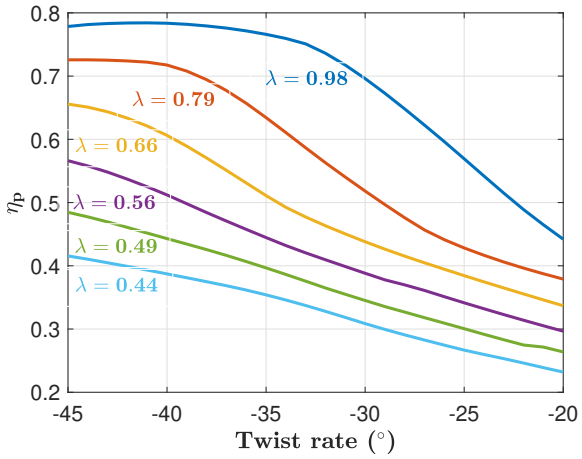

(c) Propeller efficiency versus θ_{tw}, λ using Clark-Y airfoil

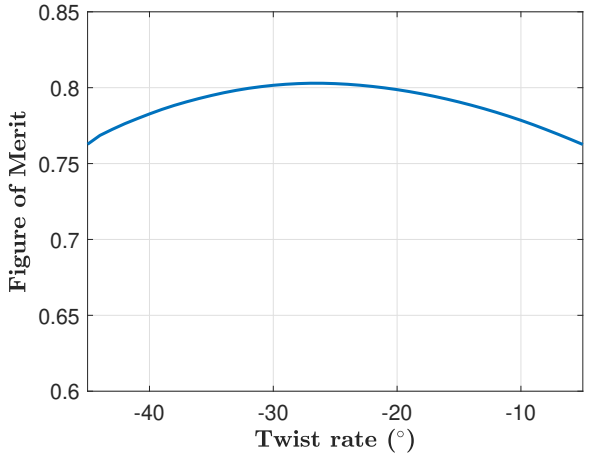

(d) Figure of Merit versus θ_{tw} using Clark-Y airfoil

Figure 4.8: Thrust and power coefficients traded against twist and inflow ratio

4.4 Configuration 2: Stopped Rotor

The lifting rotors are stopped in cruise. The addition of separate propellers requires their own individual sizing based on the vehicle drag. The use of a single wing and and non-collective propellers necessitates vertical and horizontal stabilizers. Since the rotors stop parallel to the vehicle longitudinal axis in forward flight, the rotors are restricted to having two blades each. Adding additional blades would significantly increase the drag when stopped, adversely affecting cruise performance.

4.4.1 Number of Propellers and Rotors

The optimal number of propellers and rotors were traded simultaneously on a gross weight versus rotor radius plot shown in Figure 4.9. The irregular trend from increasing the number of propellers results from different power-out scenarios affecting the estimated motor weight, which is covered in greater depth in Section 4.6.1. Much like the tiltrotor, adding more rotors brings the gross weight down, discounting penalty from support structures, but become increasingly difficult to place, especially with the need for additional

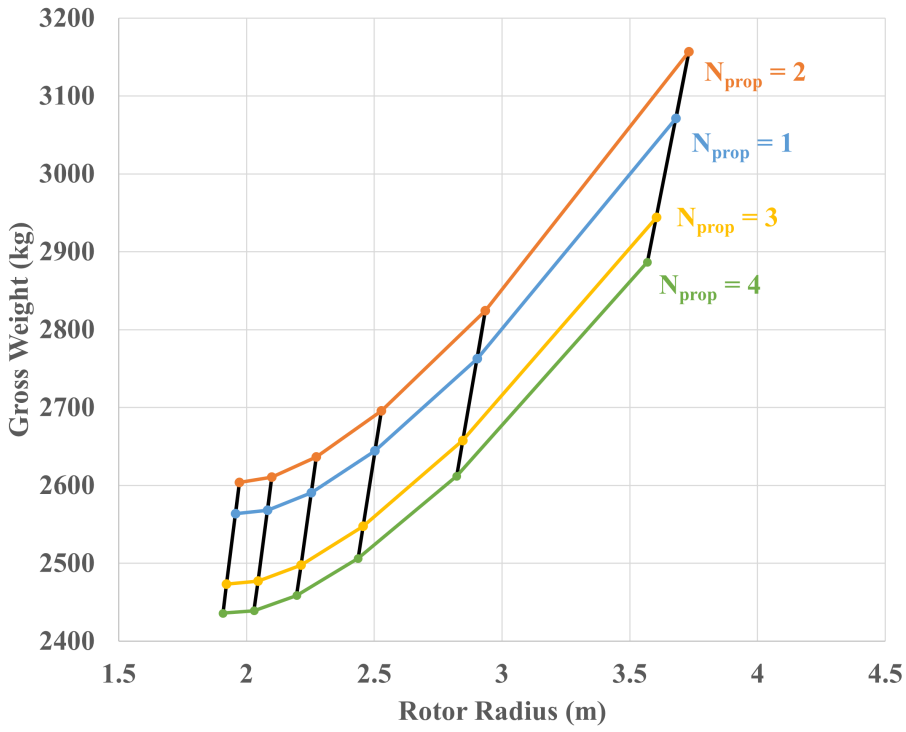

Figure 4.9: Gross weight and rotor radius vs. number of rotors and propellers

structure to support more rotors. Four combinations of number of rotors and number of propellers were considered for further investigation:

1. 6 rotors, 2 propellers
2. 6 rotors, 3 propellers
3. 8 rotors, 2 propellers
4. 8 rotors, 3 propellers

Trade studies similar to those done in Section 4.3.3 were performed for the aforementioned combinations of rotors and propellers. Using circle packing theory, a theoretical maximum rotor radius was determined for both 6 rotors and 8 rotors. The best combination of number of rotors and propellers was determined by the combination that yielded the most number of possible design points below the maximum radius, which were $R_{6\text{ rotors}} = 2.86$ m (9.38 ft) and $R_{8\text{ rotors}} = 2.60$ m (8.53 ft). From this analysis, a configuration with 8 rotors and 2 propellers was selected.

4.4.2 Rotor Parameters

Rotors that are stopped in flight require higher aspect ratios to reduce adverse aerodynamic effects and be stiff enough to not flap around. Thus, a range from 4 to 7 was swept. Increasing the rotor aspect ratio decreased the weight of the vehicle but reduced the number of available design points. These available design points at high aspect ratio also required high tip speeds and in turn affected noise. A rotor aspect ratio of 6 and tip speed of 167.64 m/s (550 ft/s) was chosen as a compromise on noise, radius, and weight minimization.

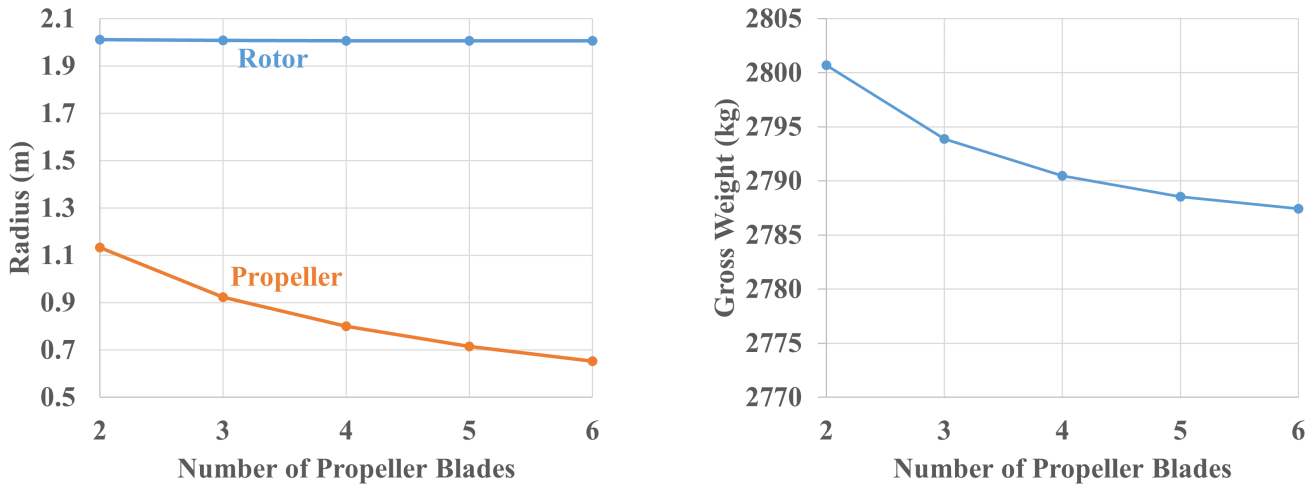

(a) Propeller radius vs. number of propeller blades

(b) Rotor radius vs. number of propeller blades

Figure 4.10: Parametric trade study on number of propeller blades for stopped rotor

4.4.3 Number of Propeller Blades

A sweep of number of propeller blades was performed to better understand its effect on rotor and propeller radius. Figure 4.10 shows that increasing the number of propeller blades only affects propeller radius. While the rotor radius appears to be constant, it is actually decreasing in increments of 0.0254 mm (0.001 in) with increasing number of propeller blades. On the one hand, fewer blades maximize efficiency; on the other, more blades decreases noise generation. As a result, 2 and 3 propeller blades were selected for further investigation.

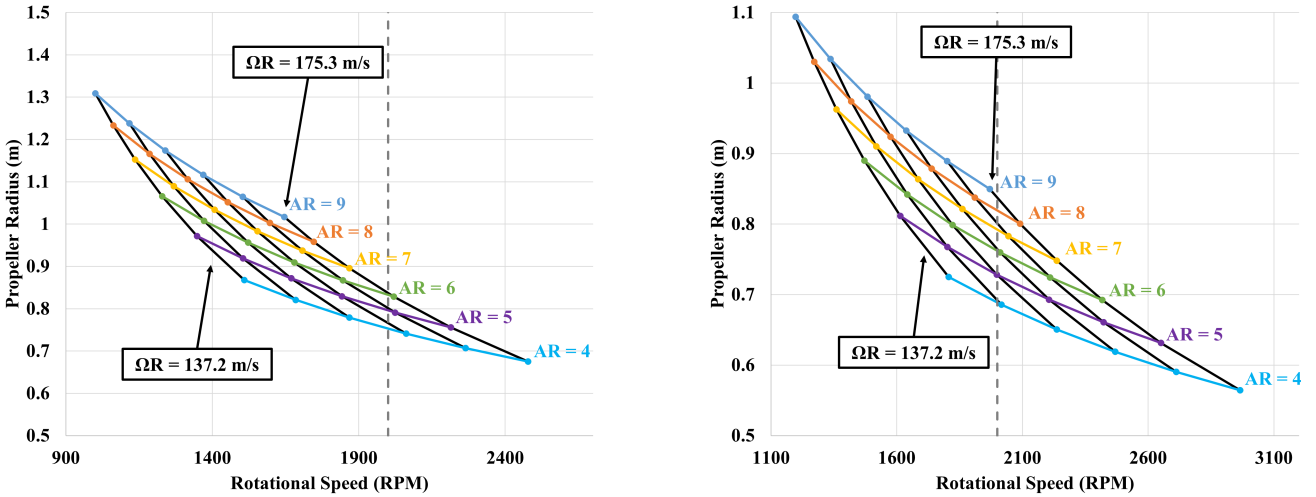

(a) Propeller radius vs. rotor RPM for 2 blades

(b) Propeller radius vs. rotor RPM for 3 blades

Figure 4.11: Propeller radius vs. RPM

4.4.4 Propeller Aspect Ratio and Tip Speed

For a fixed number of blades, propeller radius, propeller rotational speed, and gross weight were traded against propeller aspect ratio and tip speed. Propellers typically have aspect ratios between 5 and 12, but a more conservative range of 4 through 9 were selected for this study. The selection of tip speed was motivated by reducing the need for gearboxes. Rotors and propellers operating at above $\Omega = 2000$ RPM can be connected directly to the motor without needing gearboxes to reduce the RPM [21]. From Section 4.4.3, a propeller radius of $R_{\text{prop}} \approx 0.92$ m (3.03 ft) was used to determine a suitable range of propeller tip speeds to examine by finding the corresponding RPM. A range of 137.2 to 175.3 m/s (450 to 575 ft/s) was considered as it results in Ω =1418 to 1812 RPM, which can be increased by varying the aspect ratio as show in Figure 4.7. A conclusion similar to that of Section 4.4.3 was made that varying either propeller property did not significantly affect the overall weight of the vehicle, so rotor rotational speed primarily influenced the propeller selection. The optimal design points lie above 2000 RPM as Figure 4.11. Operating at the highest tip speed would reduce both propeller radius and rotor RPM but result in a louder propeller. Furthermore, using lower aspect ratio propellers would significantly increase cruise power via an increase in the propeller solidity. In the comparison between $N_{b,\text{prop}} = 2, 3$, it can be observed that more valid design points were available above 2000 RPM with higher aspect ratios. Thus, the following geometric parameters were selected for the stopped rotor propellers: $N_{b,\text{prop}} = 3$, $AR = 7$, $V_{\text{tip}} = 167.6$ m/s (550 ft/s).

4.4.5 Wing Sizing

The procedure for sizing the stopped rotor wings followed that for the tiltrotor. The propellers would be placed on the tip of the wings, but the smaller diameter would allow for a larger wingspan. The wing aspect ratio still has to be relatively low since the rotors would be placed along both wings. An aspect ratio of 7 and wing loading of 957.6 N/m^2 (21 lb/ft^2) resulted from the analysis.

As mentioned earlier, the stopped rotor configuration would require horizontal and vertical stabilizers for pitch and yaw stabilization. Many aircraft use symmetric airfoils for their stabilizers, so a NACA 0012 was used. Using a sizing methodology from Gudmundsson [13], the vertical and horizontal tail dimensions were found below:

Table 4.2: Dimension of stopped rotor stabilizers

Stabilizer	Span (m)	Average Chord (m)
Horizontal	4.85	1.21
Vertical	2.16	1.1

4.4.6 Thrust and Power Coefficients

Much like Figures 4.8(a) and 4.8(b) in Section 4.3.5, it is difficult to quantify vehicle performance using the coefficients alone, as shown in Figures 4.12(a) and 4.12(b). Dividing the quantity C_T/C_P by the hover tip speed would yield the stopped rotor power loading (PL) in hover. However, the metric in cruise is propulsive efficiency $C_T\lambda/C_P$ shown in Figure 4.12(c). Figure 4.12(c) shows that decreasing the propeller tip speed increased its efficiency. As a dedicated propeller, it can be observed that it can achieve a higher propulsive efficiency than that of the tiltrotor. The stopped rotor Figure of Merit in Figure 4.12(d) follows the same trend as Figure 4.8(d) earlier. The maximum Figure of Merit is reduced due to a lower aspect ratio.

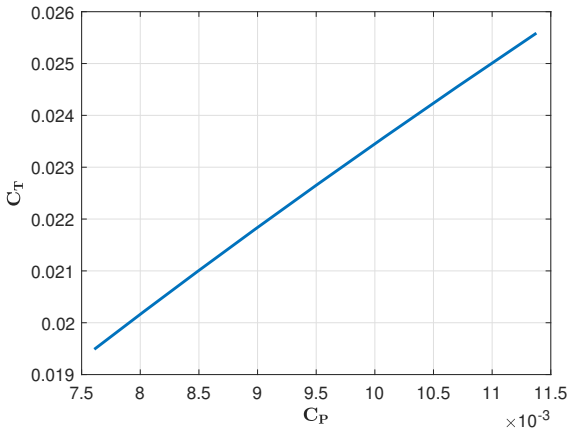

(a) C_T vs. C_P for stopped rotor

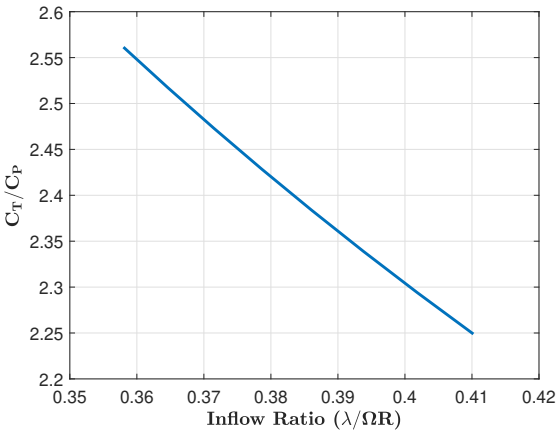

(b) C_T/C_P vs. λ for stopped rotor

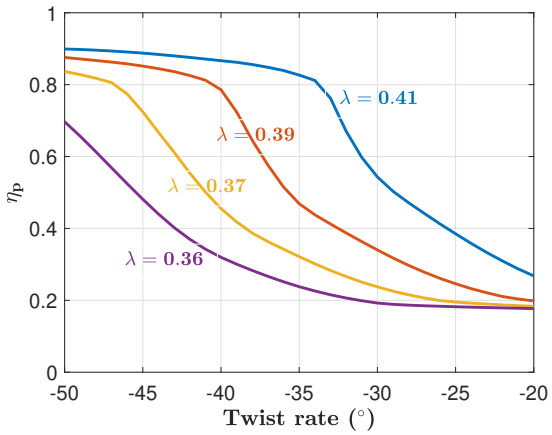

(c) Propeller efficiency vs. θ_{tw}, λ for stopped rotor propeller

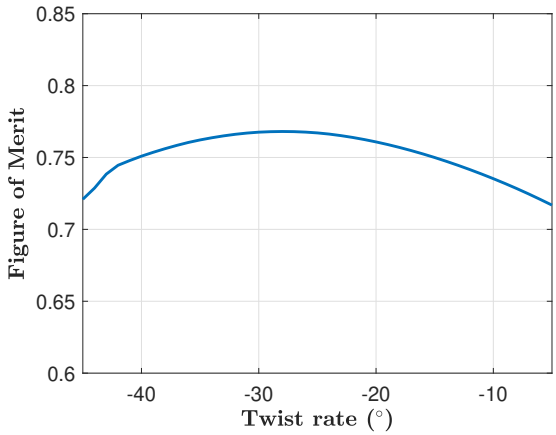

(d) Figure of Merit versus θ_{tw} for stopped rotor rotor

Figure 4.12: Thrust and power coefficients traded against twist and inflow ratio for stopped rotor

4.5 Configuration 3: Multicopter

Sizing for the multicopter follows the same steps highlighted in Sections 4.3.1 and 4.3.3. Within the sizing code, the climb, cruise, and descent legs had power calculated using momentum theory in forward flight. Like the stopped rotor, the multicopter faces a similar challenge of rotor placement, so mathematical circle-packing was used again to approximate the maximum allowable rotor radius.

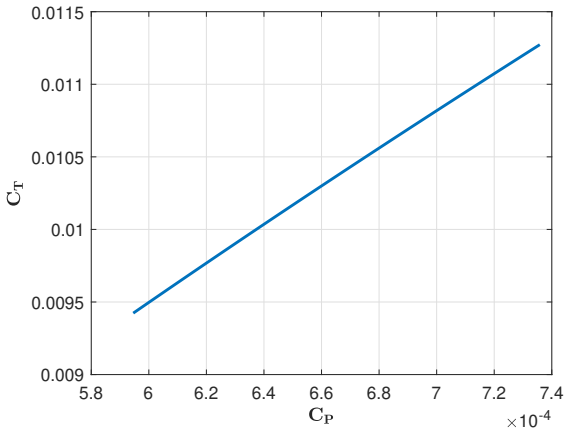

(a) C_T vs. C_P for multicopter

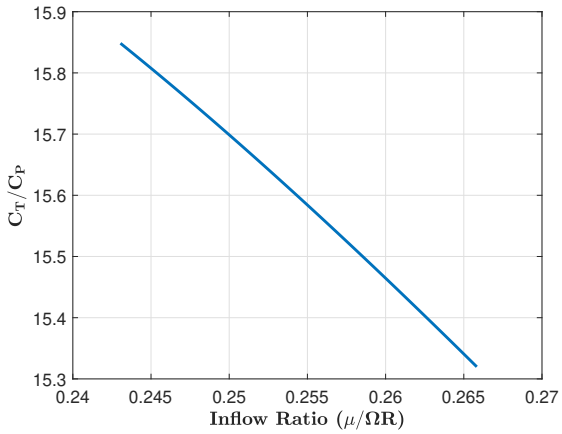

(b) C_T/C_P vs. λ for multicopter

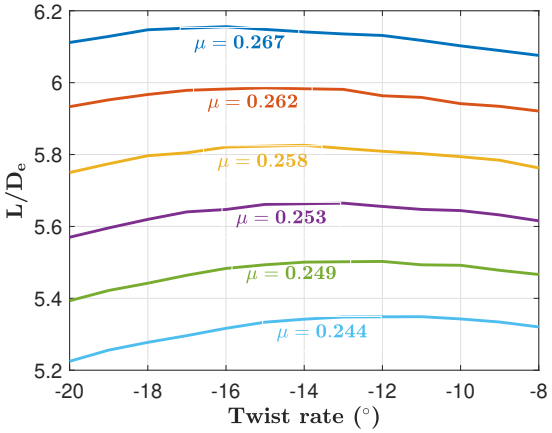

(c) L/D_e vs. θ_{tw}, λ for multicopter

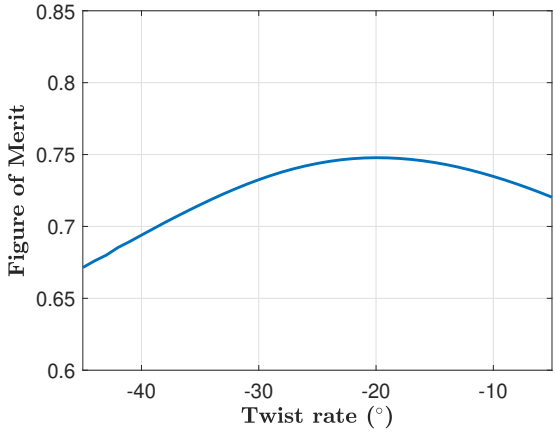

(d) Figure of Merit vs. θ_{tw} for multicopter

Figure 4.13: Thrust and power coefficients traded against twist and inflow ratio for stopped rotor

4.5.1 Overall sizing

The desired configuration for the multicopter resulted from a systematic trading of design parameters. Many of the decisions made for the multicopter used similar justification for that of the tiltrotor and stopped rotor. The post-sizing specifications of the multicopter are shown in Table 4.5.

4.5.2 Thrust and Power Coefficients

Figures 4.13(a) and 4.13(b) show the C_T versus C_P and C_T/C_P versus λ plots, respectively. The cruise performance of an edgewise rotorcraft is better quantified with L/D_e. Figure 4.13(c) shows that slightly decreasing the tip speed increases the multicopter's cruise efficiency. Figure 4.13(d) shows the same trend as the previous two configurations.

4.6 Generalized Trade Studies

The following studies apply to all three configurations.

4.6.1 Motor Selection

There are a limited variety of electric motors that can be used, each with their own set of advantages and disadvantages. These motor varieties are compared in Table 4.3. The evaluation criteria were:

1. Maturity and Certification: Proven and readily available technologies were preferred to ensure safety and rapid certification.
2. Reliability: Designs that were less prone to errors during regular operation was preferred. Fewer wear components will tend to be more reliable.
3. Volume Overhead and Integration: Smaller volume overhead and more suitable shape were preferred.
4. Acoustic Noise: Lower external acoustic noise generated across RPM range were preferred.
5. Efficiency: Maximizing ratio of mechanical output to electrical input was preferred.
6. Transient Response: Lower rotational inertia was preferred to increase bandwidth for RPM control.
7. Electrical Noise: Less unwanted electrical signal transmitted unintentionally into circuit was preferred.
8. Lifecycle Cost: A lower total cost to source raw materials, fabricate, manufacture, operate and maintain the motor was preferred.

Table 4.3: Motor type Pugh matrix

Criteria	Weights	Normalized Weights	Permanent magnet (PM) brushless DC (BLDC)	Brushed DC	Switched Reluctance	AC Induction
Maturity and Certification	5.00	0.18	0	0	-3	0
Reliability	5.00	0.18	0	-3	1	0
Volume and Integration	4.00	0.14	0	-1	-1	-3
Acoustic Noise	4.00	0.14	0	-3	-3	1
Efficiency	3.00	0.11	0	-2	1	-2
Transient Response	3.00	0.11	0	-2	2	1
Electrical Noise	2.00	0.07	0	-2	2	0
Lifecycle Cost	2.00	0.07	0	0	1	-1
Score			**0.00**	**-1.68**	**-0.39**	**-0.46**

The brushless DC (BLDC) electric motor was selected, and a number of commercially available BLDC motors were reviewed to develop weight models to size the aircraft. From multiple suppliers and sources, motors were surveyed and key characteristics were modeled with regression lines as shown in Figure 4.14. In addition to motor weight, electrical efficiency of the motor η_{peak}, diameter of the motor D_{motor} for drag, and motor input voltage V were considered as functions of peak torque output. With the motors installed directly below or behind the propeller and the motor diameter dictating the size of the nacelle, a smaller diameter is preferred to reduce drag. In addition, greater operating voltage is preferred to minimize current losses, thereby saving weight. Ideally, the motor would be designed specifically for the aircraft.

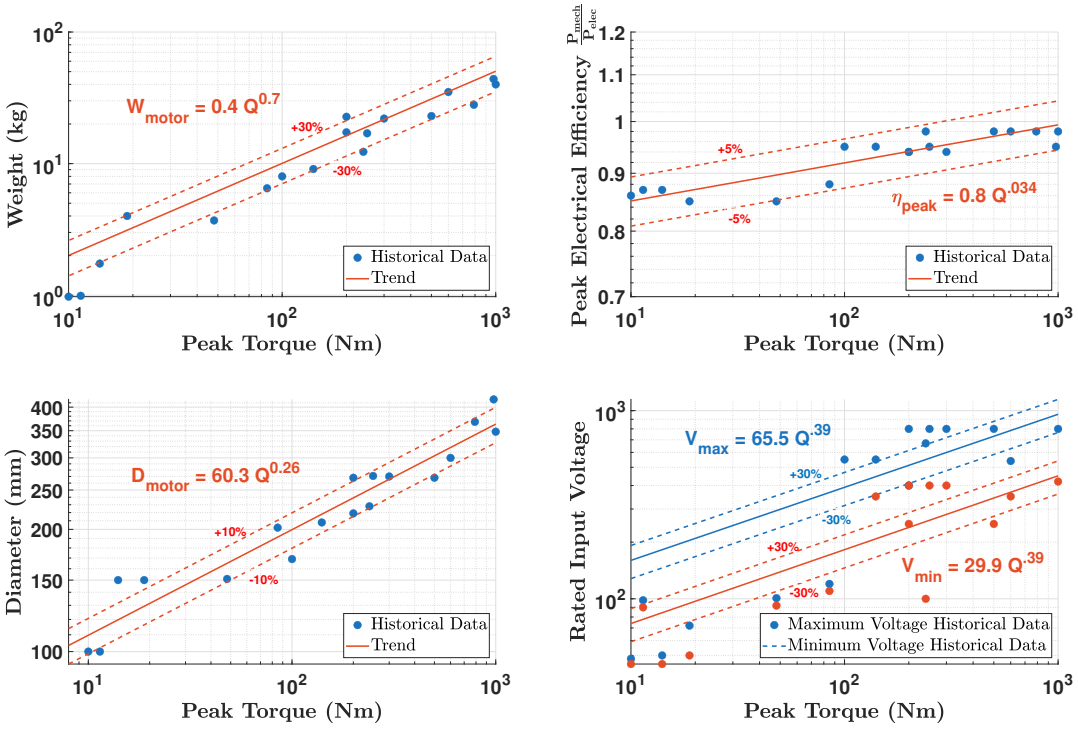

Figure 4.14: Reviewed trends for BLDC electric motors.

As required by the RFP, "the aircraft shall be capable of continued safe flight following any single failure of the electrical power distribution system". Thus, to ensure the aircraft is capable of hover following a single motor failure, two solutions can be used:

1. For each rotor, a single motor can be used to drive the rotor. However, with the loss of one motor, one out of the total number of rotors will become inoperable, thereby requiring greater power from the remaining motors to drive the remaining rotors. In addition, an opposing motor(s) would need to throttle down to balance aircraft moments. If multiple motors fail, the corresponding set of motors would also need to be throttled down, further increasing the power required for the remaining rotors. This is similar in methodology to the six rotor Joby S4 vehicle as described by Stoll and Bevirt [22]. For a single rotor, a total torque Q_{rotor} is required. An approximation for torque required per motor for a vehicle with a total number of rotors N_{rotors} is then:

$$Q_{\text{motor w/ tol.}} = \frac{N_{\text{rotors}}}{N_{\text{rotors}} - 2} \cdot Q_{\text{rotor}} \qquad \text{for } N_{\text{rotors}} \geq 2 \tag{2}$$

2. For each rotor, multiple stacked motors can be used to drive the rotor. The torque per motor $Q_{\text{motor w/out tol.}}$ without compensation for loss in torque required due to a motor failure with a total number of motors N_{motors} per rotor is:

$$Q_{\text{motor w/out tol.}} = \frac{Q_{\text{rotor}}}{N_{\text{motors}}} \qquad \text{for } N_{\text{motors}} \geq 1 \tag{3}$$

However, in the event of a single motor failure, Equation 3 does not produce the total torque required Q_{rotor}. To compensate for a single motor failure, the torque required per motor $Q_{\text{motor w/ tol.}}$ becomes:

$$Q_{\text{motor w/ tol.}} = \frac{N_{\text{motors}}}{N_{\text{motors}} - 1}\left(\frac{Q_{\text{rotor}}}{N_{\text{motors}}}\right) = \frac{Q_{\text{rotor}}}{N_{\text{motors}} - 1} \qquad \text{for } N_{\text{motors}} \geq 2 \tag{4}$$

Comparing both methods, the total motor weight per rotor with single motor failure tolerance is defined based on the historical trend:

$$W_{\text{motors}} = N_{\text{motors}} \cdot 0.4 \cdot (Q_{\text{motor w/ tol.}})^{0.7} \tag{5}$$

To reduce complexity, the motors will be placed directly behind and along the same axis as the rotor. Thus, an estimate for the front plate area of the motors in forward flight, and therefore the nacelle front plate area, can be defined based on the historical trend of the motor diameter:

$$f_{\text{motors}} = \pi \cdot 9.09 \cdot 10^{-4} \cdot (Q_{\text{motor w/ tol.}})^{0.52} \tag{6}$$

Figure 4.15 shows total motor weight for a single rotor for both solutions. For the first solution described which uses a single motor per rotor, Equation 2 was used with four, six, and eight rotors to calculate motor weight and front plate area. These results are labeled as '1 motor per rotor' for four, six, and eight rotors. The stacked motor cases were calculated using Equation 4.

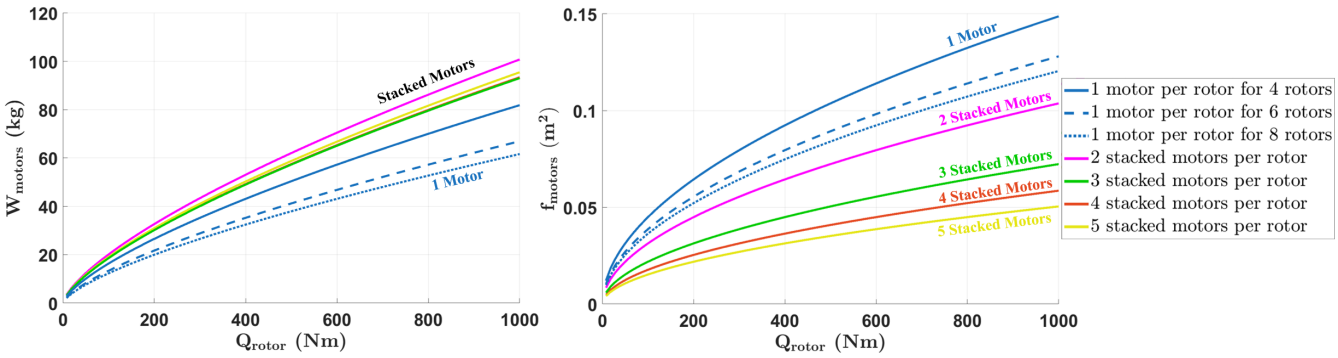

Figure 4.15: Total weight of motors (left) and flat plate area of motors in forward flight mode (right) vs. rotor torque.

For the tiltrotor which has four rotors, '1 motor per rotor for 4 rotors' is compared to the stacked motor cases. Compared to a single motor, the stacked motor trades 14% increased weight for 52% reduced front plate area. In addition, cyclic control is avoided with stacked motors for a four rotor vehicle. This is because with only three rotors operating, additional moments are required to hover the vehicle. Notably, three stacked motors is 7.6% lighter than two stacked motors and the lightest of all the stacked motor multitudes. Ultimately, a stack of three motors was selected as it provides safety and the best trade between reduced weight, forward flight drag, and complexity. In addition, out of the total number of motors, 1 motor per rotor can fail simultaneously and the vehicle will continue to fly without issue. Thus, for the tiltrotor configuration, the stacked motor configuration allows for a total of 4 motor failures.

For the stopped rotor and multicopter hover motors, three stacked motors were selected to ensure all rotors continue operating at their design figure of merit even in the event of a failure. In contrast, with a single motor per rotor, the figure of merit will decrease for the remaining rotors as they will operate at greater collectives/RPMs to compensate.

4.6.2 Wing Aerodynamic Design

The main wing airfoil for both the stopped rotor and the tiltrotor configurations was selected based on the following requirements:

1. High $C_{l_{max}}$ and gradual stall onset
2. Relatively high thickness-to-chord (t/c) for adequate beam stiffness to prevent whirl flutter
3. Adequate torsion stiffness to prevent air resonance
4. High L/D for cruise efficiency
5. Low pitching moment
6. Adequate dimensions for internal battery placement

Twenty airfoils were investigated and the NACA2418 airfoil was ultimately selected. This airfoil has a 18% thickness, low pitching moment and high L/D. Its properties are plotted in Figure 4.16. Later, it was confirmed to allow for sufficient internal structure to prevent whirl flutter and air resonance.

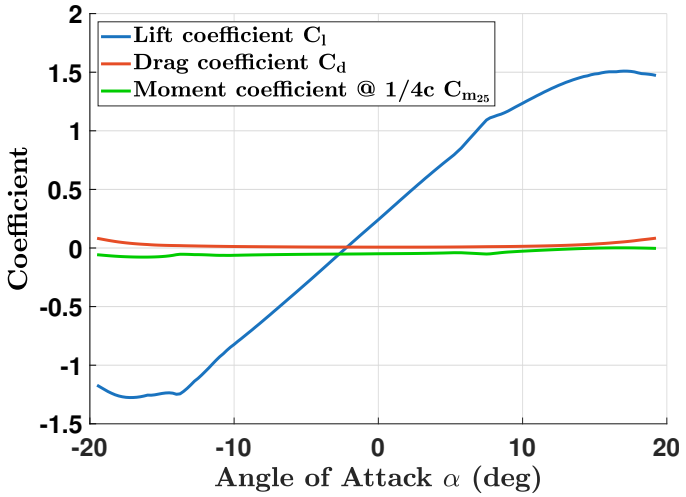

Figure 4.16: Wing 2D NACA2418 airfoil characteristics

4.6.3 Landing Gear

A common landing gear was selected for all three configurations because they must complete the same mission. An initial comparison between skids and wheels was made. Skids are lightweight and cost-efficient to manufacture; however, skids have relatively high drag coefficients compared to their wheeled counterparts [23]. In addition, wheeled landing gears are better suited to land on prepared surfaces commonly found in heliports and urban environments, so a wheeled landing gear system was selected for all three configurations.

The cruise portion of the mission incentivizes the minimization of drag as much as possible. The use of retractable landing gear would minimize landing gear drag. Empirical estimates indicate that landing gear retraction mechanism increases the landing gear weight by approximately 10%.

Table 4.4: Weight comparison of different landing gear types, tricycle configuration

Landing Gear	Tiltrotor	Stopped Rotor	Multicopter
Fixed wheel system weight (kg)	104.4	103.1	109.8
Fixed wheel drag/area at V_{cruise} (N/m^2)	951.4	872.9	404.3
Retractable wheel system weight (kg)	114.8	113.4	120.7

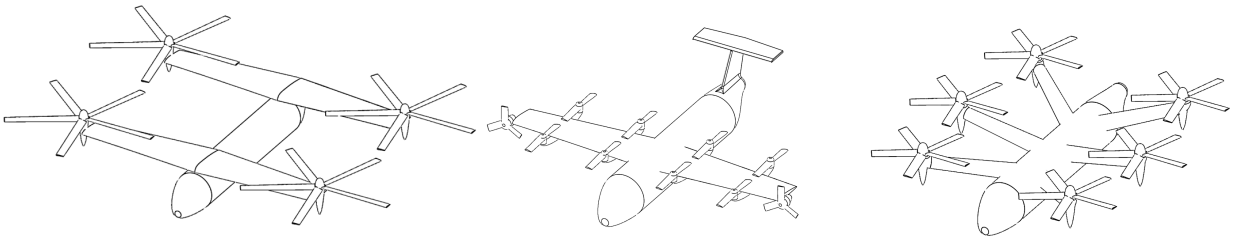

(a) Tiltrotor (b) Stopped Rotor (c) Multicopter

Figure 4.17: Three configurations selected for further trade study

4.7 Trade Summary

Table 4.5: Comparison of eVTOL configurations

Parameter	Tiltrotor	Stopped Rotor	Multicopter
Number of Rotors	4	8 (hover) 2 (propeller)	6
Number of Wings	2	1	0
Gross weight (kg)	2548.0	2589.9	2747.1
Cruising speed (km/hr)	205	199.3	140.8
Drag area in cruise (m^2)	0.49	0.58	0.69
Trip time (hr:min)	0:50	0:52	1:14
Rotor diameter (m)	5.16	3.49 (hover) 1.17 (propeller)	4.83
Solidity	0.13	0.11 (hover) 0.14 (propeller)	0.10
Linear twist (deg)	-45	-25 (hover) -45 (propeller)	-16
Tip speed in hover (m/s)	137.2	167.6 (rotor)	160
Tip speed in cruise (m/s)	60.96	155.4 (propeller)	156.4
Figure of Merit, all systems operating	0.8	0.77	0.75
Motor per rotor configuration	Three-stacked	Three-stacked (hover) Three-stacked (cruise)	Three-stacked
Figure of Merit, single-system failure	0.8	0.77	0.75
Power required, IGE hover (kW)	425.79	518.6	409.96
Power required, vertical climb (kW)	421.44	444.76	407.73
Power required, OGE hover (kW)	426.29	519.17	410.33
Power required, climb (kW)	345.2	311.12	335.99
Power required, cruise (kW)	123.39	131.02	205.37
Power required, desecnt (kW)	9.14	7.14	165.44
Power required, vertical descent (kW)	426.29	519.17	382.12
Total energy consumed per mission (kWh)	152.1	389.86	326.4
Reserve energy (kWh)	41.1	43.67	68.46
Total battery weight	432	396.5	861.3
Motor continuous torque (Nm)	127 (hover) 92 (cruise)	128 (rotor) 116 (propeller)	203
Motor continuous power (kW	53.37 (hover) 17.18 (cruise)	62.53 (rotor) 30.22 (propeller)	67.29

4.8 Advantages and Disadvantages of Each Configuration

The results from the trade studies on vehicle geometries, motors, and lifting surfaces allowed the design team to compare the three configurations against the configuration drivers specified in Section 3.

The multicopter was the first configuration removed from consideration based on the performance. Compared to those of the stopped rotor and the tiltrotor, the multicopter has as significantly lower L/D. The relatively low cruise performance and longer time to complete the mission make it a less attractive option as an air taxi for passengers and operators alike. The multicopter requires a significantly larger battery than the other two configurations. More energy per mission results in higher operating costs and thinner

profit margins or higher price per mile, neither of which is appealing.

The comparison between the stopped rotor and the tiltrotor was not as straightforward. Both vehicles have comparable vehicle cruise efficiency and gross weights. In the end, it was the manufacturing complexity of the stopped rotor and higher expected lifecycle maintenance cost that ultimately led to the selection of the tiltrotor. The stopped rotor tip speed is 22% higher than the tiltrotor which is known to directly correlate with sound pressure level. Alongside tip speed, the tiltrotor makes use of an odd number of blades which helps mitigate constructive addition of sound pressure waves and vibratory loads from the rotor. In each leg of its mission, the stopped rotor is carrying weights of rotors that are not used in cruise and add to the drag profile. The lack of reliable weights and loads data on these types of rotors also makes them unreliable. With many more rotating elements, especially the rotors that come to a rapid halt, the maintainance of the drive system is expected to be higher than the tiltrotor.

The tiltrotor was also the preferred configuration for a number of other reasons. On the certification front, several advancements have been made to define a clearer path to FAA type certification for tiltrotor civil transport. The Joby S4 recently received its first certification that would allow it to be flown commercially. Leonardo is also working very closely with the FAA to not only acquire certification but also define new sets of regulations for civilian tiltrotors in general. Test data from the electric Maryland Tiltrotor Rig and validated in-house codes have indicated flutter-free safe flight for hingeless hubs up to 463 kmph (250 kts, 287.9 mph) [24]. The subsequent sections will go into greater depth on structural, aerodynamic, and dynamic properties that validates *Starling* as a tiltrotor airworthy for primetime operation.

4.9 Final Selected Vehicle, Quad Tiltrotor *Starling*

Table 4.6: Key Features of *Starling*

Feature	Requirement	*Starling*'s Value
Block time	-	48 min
GTOW	-	2518.79 kg (5552.97 lb)
Footprint	15.24 m × 15.24 m	10.37 m × 14.6 m
Vehicle Height	-	3.14 m (10.3 ft)
Maximum speed	-	277.8 km/hr (150 kts)
Hover noise level	-	52.2 dBA
Empty weight	-	1929.12 kg (4252.97 lb)
Maximum payload	-	589.67 kg (1300 lb)
Battery Energy	-	191 kWh
Battery Nominal Voltage	-	600 V
Battery C-rate	-	3 C
Battery Weight	-	479 kg (1056 lb)
Maximum altitude	-	4500 m (15000 ft)
Installed power	-	623 kW (835.5 hp)
Rotor radius	-	5.16 m (16.93 ft)
Disk loading	-	6.73 lb/ft^2 (32.86 kg/m^2)
Charge rate	-	250 kW

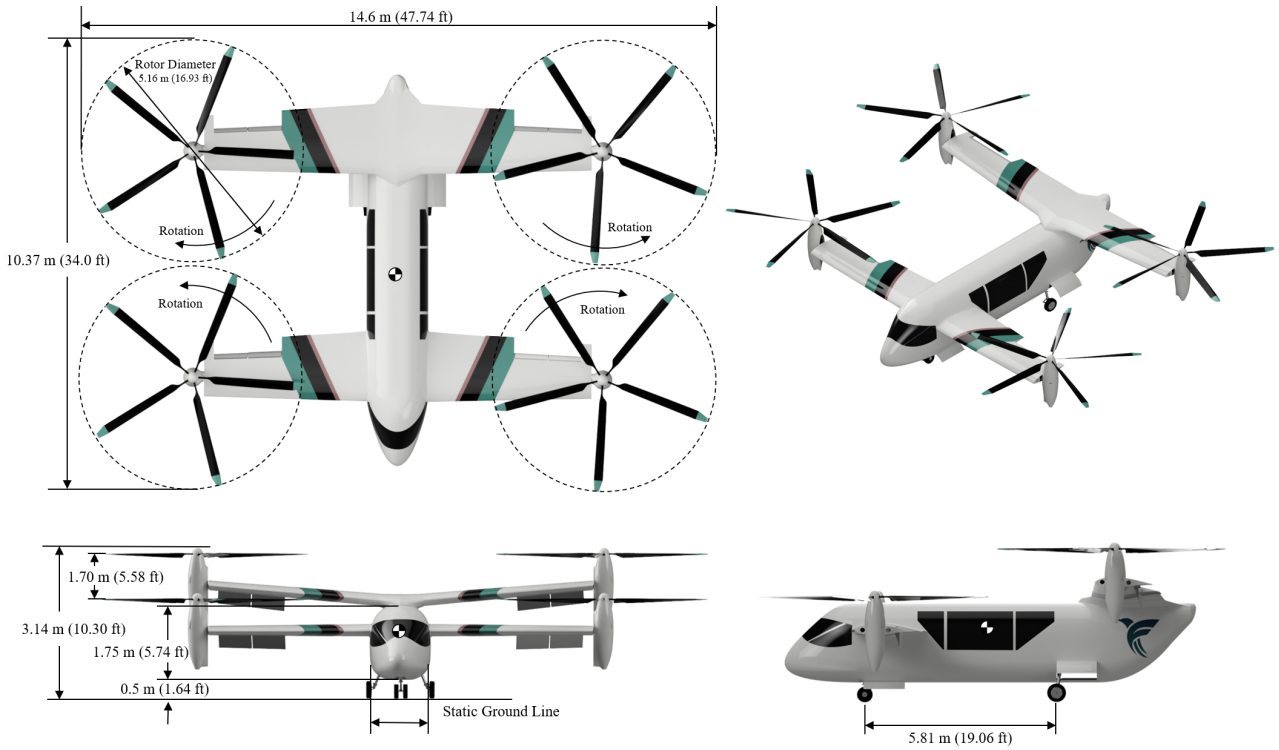

Figure 4.18: Three view of *Starling* hover configuration

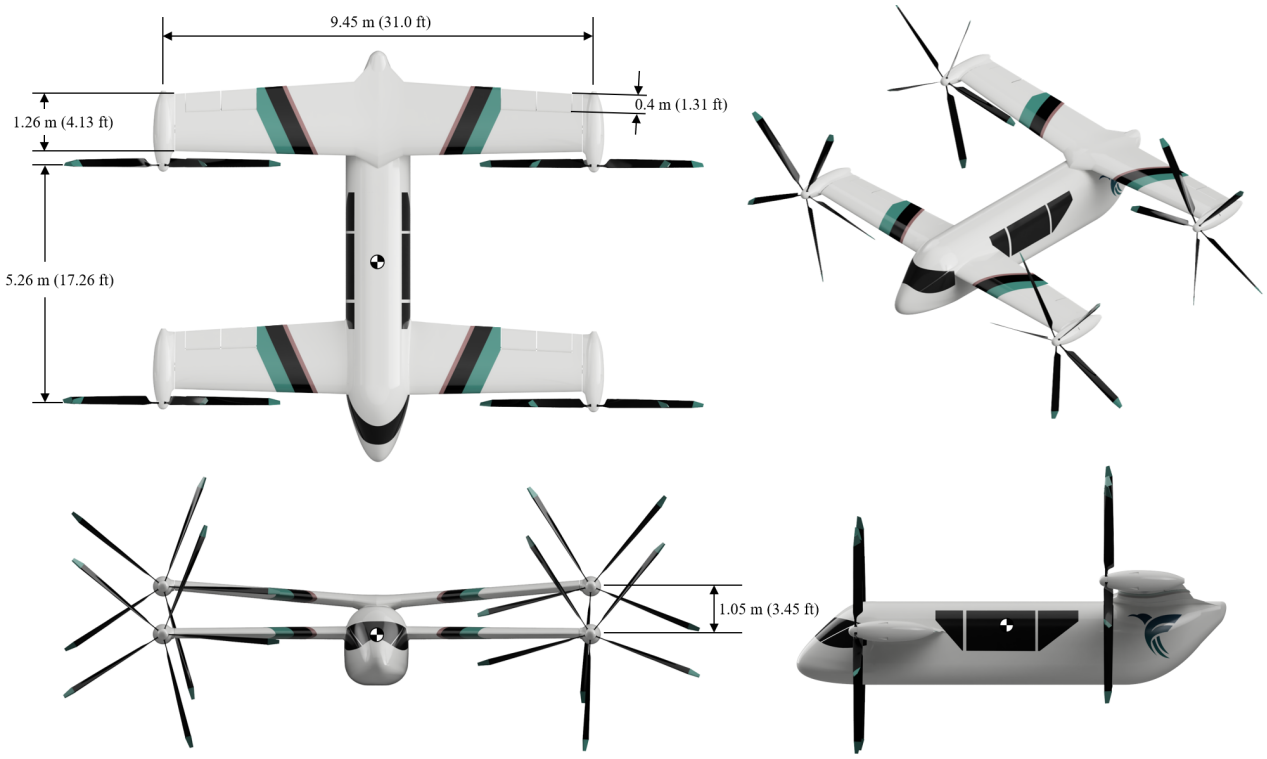

Figure 4.19: Three view of *Starling* cruise configuration

5 Accessible Cabin Design

Starling is designed to carry a single pilot and four passengers without reduced mobility or two passengers with reduced mobility, including their baggage and necessary medical equipment. From boarding to seating, the vehicle is designed to restore passenger independence and accommodate a wide range of passenger types, including those with reduced mobility and hidden disabilities.

5.1 Motivation

The desire for people with reduced mobility to independently travel on aircraft is often at odds with existing FAA regulations. The size of the aisles on most commercial aircraft are often too small for many wheelchairs to navigate, so passengers with reduced mobility must be physically assisted onto an aisle chair and then into their flight seat. This strategy of boarding is exhausting to the passenger and generates an undesired feeling of helplessness by removing the passenger's independence. In a joint personal interview with Bell, Mike Miller-Smith, CEO of Aerobility, stated that the ideal solution would be to have passengers with reduced mobility be able to fly in their personal wheelchairs. Buses and other common forms of public transportation already allow this capability by employing ingress-egress strategies and technology, but these solutions are still too heavy for aircraft.

While allowing passengers to travel in their own wheelchairs would be the most egalitarian, the solution faces a number of logistical and bureaucratic hurdles. Existing FAA and CFR regulations mandate that passengers must fly in airplane-crashworthy seats as a safety measure. These standards become even more stringent for helicopter-crashworthy seats as the vehicle must be able to withstand at least 16 g of downward force. Crashworthiness tests involving wheelchairs restrained by a Q'Straint system have claimed that such a system would fulfill FAA crashworthy regulations; however, these tests do not provide sufficient evidence that such a system would meet FAA rotorcraft crashworthiness standards. The lack of standardization in wheelchair designs and regulations also contribute to the difficulty of using wheelchairs as aircraft seats. The federal government currently does not regulate the size of wheelchairs and other mobility assistance devices. Even though voluntary guidelines on wheelchair designs exist, the designs vary widely in size and weight to accommodate different type of ambulatory disabilities. With these conflicting requirements in mind, a suitable cabin design and ingress-egress strategy was developed that nonetheless provided autonomy for passengers with reduced mobility while complying with existing FAA requirements. Additional accommodations were added to assist passengers who have hidden disabilities.

5.2 Ingress and Egress

The existing guidelines for transportation set forth by the Americans with Disabilities Act (ADA), Subpart B - Buses, Vans and Systems, were adapted to create an ingress-egress strategy for *Starling*. Primary ingress and egress is accomplished with the ramp, as it gives disabled and non-disabled passengers independence and equality while boarding without the need for assistance from active ground personnel. As shown in Figure 5.2, passengers board on the right side of the aircraft via an external ramp. Since the vehicle's floor is higher than 22.86 cm (9 in) off the ground, the ramp has a slope of 1:12 in accordance with §1192.23(c)(5). The material selection and structural geometry was designed to be able to support 272.2 kg (600 lb) as dictated by §1192.23(c)(1). The handrails have a diameter of 3.81 cm (1.5 in) as required by §1192.23(b)(13). The surface of the handrail will have an additional texturing that enhances passengers' gripping ability when boarding or disembarking. Brightly-colored yellow dimple pads are placed on the top and bottom of the ramp to indicate ramp endpoints for visually-impaired passengers as required by §1192.25(a) and (b). Depending on the specific needs of a passenger, an external and movable elevator can also be used if it is preferred. This elevator also follows the guidelines set forth by §1192.23, which

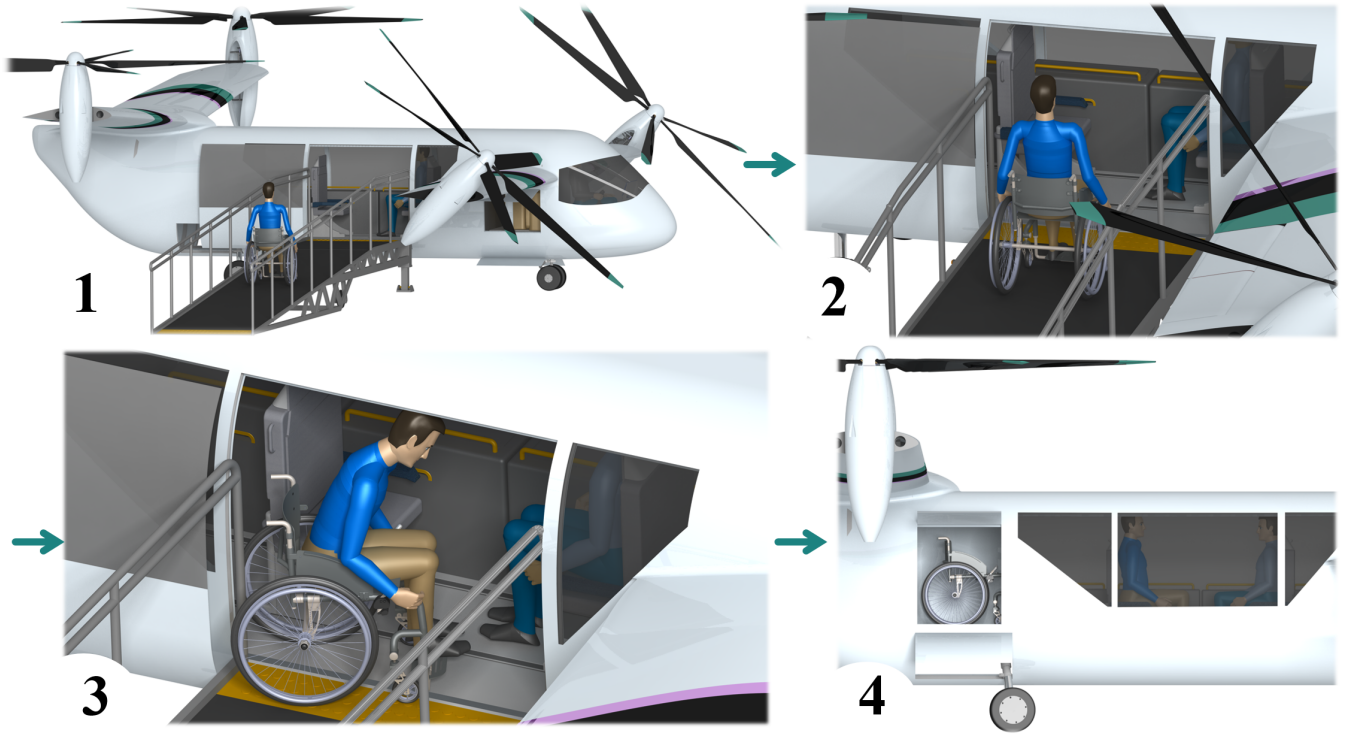

Figure 5.1: Passengers board independently via a ramp into *Starling*

includes handrail diameter, load requirement, and platform deflection rate. Both the ramp and elevator are movable by ground support crews and are designed to be perfectly flush with the vehicle's floor to ease entrance and exit, especially by passengers that require mobility devices. By using an external method of ingress and egress, accommodation for all types of passengers can be maximized while minimizing vehicle weight. In contrast, an ADA-compliant elevator integrated into the airframe would add significant weight to the vehicle. When taking into consideration the relatively few deployment cases, a built-in elevator would add considerable weight for a daily use rotary-wing aircraft.

The cabin door is located at the right and center of the fuselage, which is at the furthest point from the rotors to avoid height clearance issues. The front rotor pylons are tilted at an angle of 45° to prevent height clearance issues while boarding up the ramp. The sliding door is designed to be large to accommodate different ingress-egress strategies while being intuitive to operate by all. The locking mechanism can be seen by direct visual inspection by crewmembers on the outside and inside of the vehicle. While boarding, the front right rotor pylon can be tilted forward such that it provides greater height clearance for passengers boarding. The electric-powered rotors will not be spinning and do not need a warm-up procedure, thereby ensuring the safety of those near the outside of the vehicle.

The aisle is wider than required by 14 CFR §29.815 at 33.02 cm (13 in) wide and is located on the right side of the seats. To assist those with reduced mobility and visual impairment, railings and handles are brightly colored to be visible in daylight and nighttime. These structures are sized to be 3.81 cm (1.5 in) in accordance with ADA Subpart-B §1192.29 (b). Emergency floor lighting is also implemented to aid with navigation and emergency egress inside the cabin in low-light scenarios as required by 14 CFR §29.812.

5.3 General Cabin Accessibility Features

Given a wide variety of disabilities, the cabin must be reconfigurable to meet the needs of everyone. Seating configurations for four passengers and two passengers are shown in Figures 5.4 and 5.5. Seats are aligned in a 1×4 column and can be removed, repositioned, and reoriented to face forward or rearward via a single set of tracks on the floor. Therefore, depending on the needs of the passengers, the same vehicle can be used to seat between one and four passengers. With a column-wise seating configuration, each passenger can have sufficient space for themselves as well as a personal storage compartment directly beside them for their carry-on baggage and personal item. This guaranteed personal space reduces passenger anxiety, provides ample space for accommodations such as a service dog, and removes the need to trust an unknown passenger who would otherwise be seated directly by their side. These features are especially advantageous for those with hidden disabilities, such as post-traumatic stress disorder, who may feel discomfort with strangers and require a quiet and secluded space.

In addition, each passenger has both an aisle and a window view on either side to minimize claustrophobia. The windows are made from electrochromic glass, allowing passengers to change the tint from 0% to 100% depending on their preference. A personal storage compartment is also located directly beside them and at waist level, allowing for medical equipment to be easily and independently accessed without strain or support staff, as would be required with a traditional overhead compartment.

From a vehicle performance standpoint, seating passengers in a single column is advantageous for reducing longitudinal inertia, keeping the center of gravity located at the center of the vehicle regardless of seating configuration, and allowing the fuselage to be narrower, thereby reducing drag.

5.4 Cockpit

The cockpit is separated from the passenger cabin. The pilot door is on the left of the aircraft for ingress and egress. From a passenger comfort perspective, separating the cockpit away from the cabin and blocking the view of the cockpit with a wall can help reduce passenger anxiety by hiding pilot functions. From a physical security perspective, separating the cockpit from the passenger cabin can prevent sabotage and prevent in-flight attackers from entering the cockpit during flight.

As required by 14 CFR 29, paragraph §29.771, the vibration and noise characteristics in the cockpit are low and therefore do not interfere with safe piloting operations. The windows in the cockpit are large enough to provide a 180° view, providing a clear and unobstructed view in all weather conditions. The windshields are also designed to reduce glare which aids in ensuring adequate pilot visibility in different conditions. The windows are made from two layers of Lexan polycarbonate to minimize fragmentation in the case of bird strike at cruising speed.

5.5 Baggage Compartment

Checked baggage and durable medical equipment such as wheelchairs are stored separately in the front and rear of the passenger cabin and are accessible via doors on the outside of the vehicle. As required by 14 CFR 29, paragraph §29.785, each baggage compartment is designed to hold the maximum baggage weight of up to 271 kg (600 lb) under load factors specified by 14 CFR 29, paragraph §29.561. Items are secured by a cargo net to prevent contents from becoming a hazard in the baggage compartment. In an emergency landing, if contents break lose, they will not injure occupants as the compartments are located away from passengers at the front and rear of the aircraft and separated by a wall.

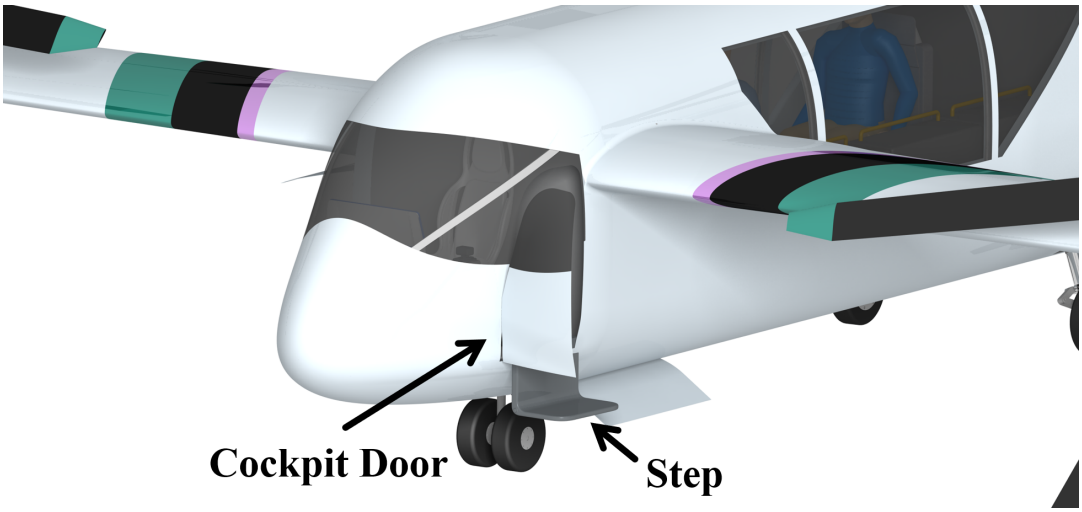

Figure 5.2: Pilot boards using a separate cockpit door and a retractable aircraft step

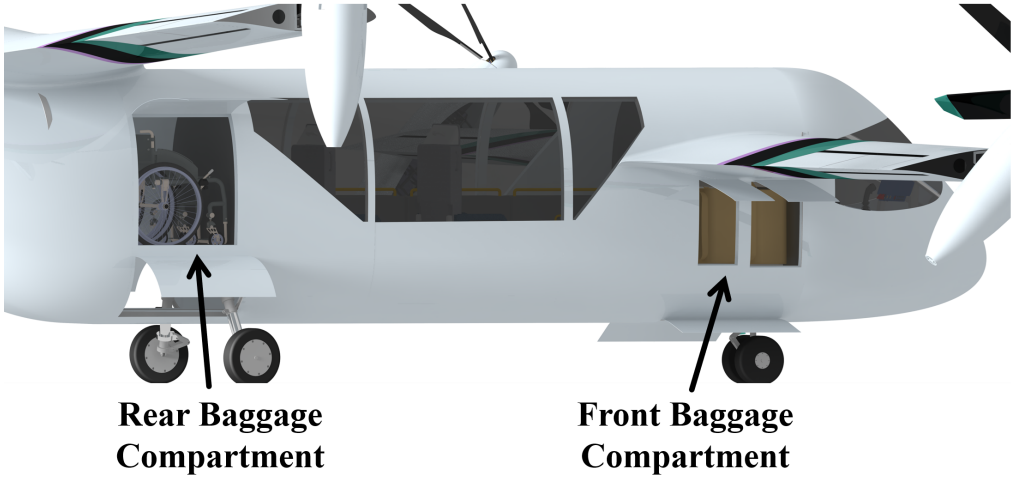

Figure 5.3: Front and rear baggage compartments

5.6 Four Passenger Configuration

In the case of four passengers without reduced mobility, the cabin can be configured with all four seats facing forward or with some facing the rear. For passengers traveling together that are co-dependent, such as a parent and child, seats can be repositioned 180 degrees to create combined seats that face one another so that those traveling together can share the same space. Seats can be reconfigured on a trip to trip basis, and therefore, do not require the aircraft to spend down time making interior reconfiguration changes. Between trips while charging the aircraft, seats can be re-positioned 180° by flight crew via latches on the floor using tamper resistant tools. The position of the seats would be available to flight crew prior to departure via flight specific passenger boarding information and reoriented within three minutes. Table 5.1 shows an itemized list and associated weights for the four passenger configuration.

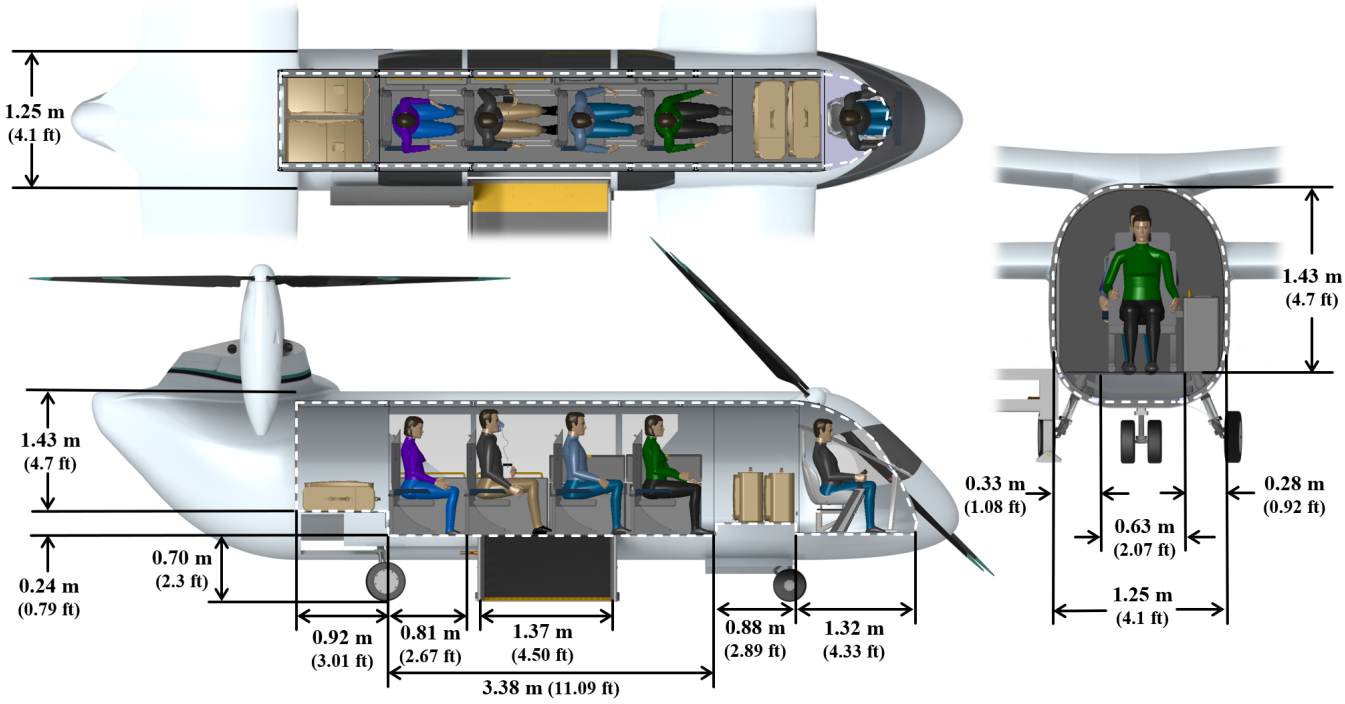

Figure 5.4: Three-view of four passenger baseline seating configuration

Table 5.1: List of cabin equipment, passengers and their baggage for four passenger configuration

Item	Quantity	Weight (kg)	Percent of Total (%)
Seat	4	68	12.0
Seat tracks	1	8	1.3
Storage bin	4	13.5	2.3
Support railings	1	6.8	1.1
Passenger	4	322.8	57.0
Checked baggage	4	92	16.0
Carry-on baggage	4	40	7.0
Personal item	4	20	3.3
Total		571.1	100

5.7 Two Passenger Configuration

For the case of two passengers with reduced mobility, the cabin can be configured with both seats facing forward or with some facing aft as shown in Figure 5.5. For passengers in wheelchairs, a flat surface, wide door, and seats located directly next to the door make it easy to independently position themselves while in the wheelchair and slide into the aircraft seat. The separate baggage compartment can then be used to store larger medical equipment such as wheel chairs, crutches, and walkers. While it is often preferred by those with reduced mobility to stay in their wheelchair throughout the flight, the current regulations do not allow for it as commercially available wheelchairs do not satisfy crash-worthiness standards. If these regulations change in the future, seats could easily be removed to provide room for personal wheelchairs that could be fastened to the floor using Q'Straints. Table 5.2 shows an itemized list and associated weights for the two passenger configuration based on estimates from known materials and historical data.

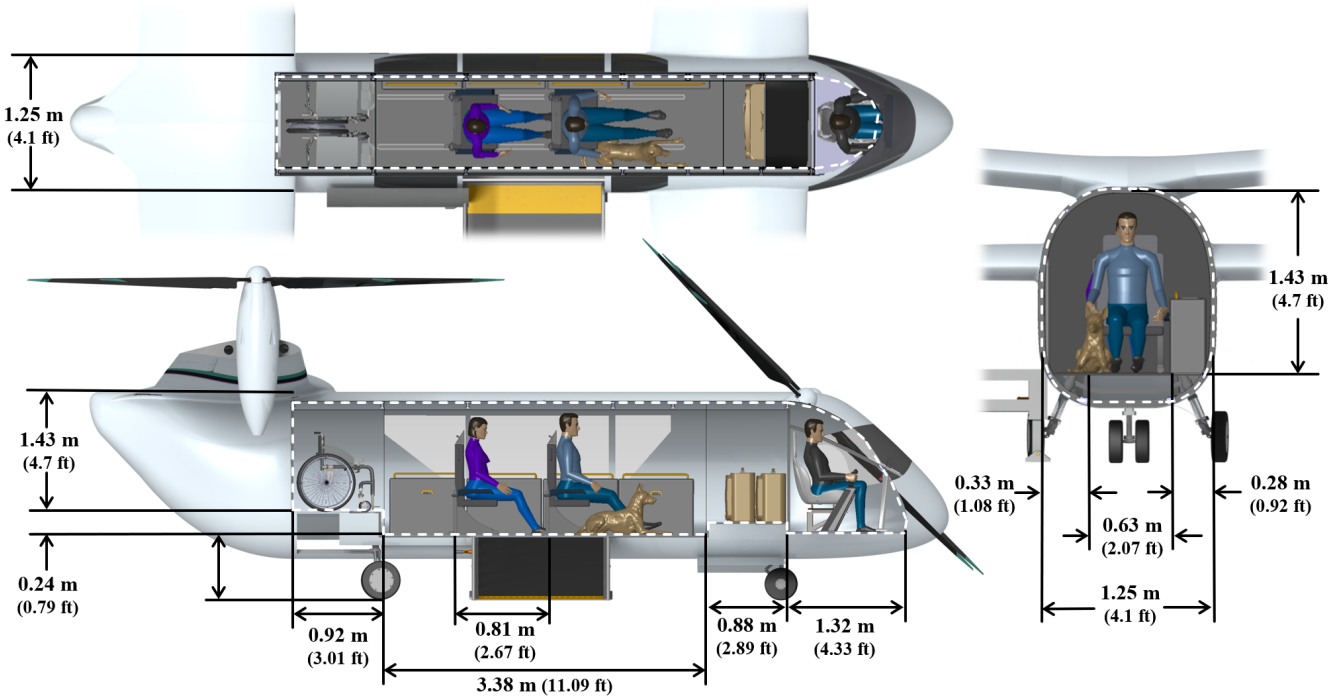

Figure 5.5: Three-view of two passenger seating configuration

Similar to the four passenger configuration, the seats can be configured to face towards the front or rear of the aircraft as shown in Figure 5.6. This is useful for disabled travelers who require a care giver or for a parent and child.

(a) Forward facing configuration

(b) Caretaker configuration

Figure 5.6: Seating configuration can be adapted to fit the needs of the passengers

Table 5.2: List of cabin equipment, passengers, and their baggage for two passenger configuration

Item	Quantity	Weight (kg)	Percent of Total (%)
Seat	2	34	6.0
Seat tracks	1	8	1.4
Storage bin	4	13.5	2.3
Support railing	1	6.8	1.2
Passenger	2	161.4	28.3
Electric Wheel Chair	2	271.4	47.5
Checked baggage	2	46	8.0
Carry-on baggage	2	20	3.5
Personal item	2	10	1.8
Total		571.1	100

5.8 Seating

Seats are designed to accommodate a maximum passenger weight of 246 lb, the 95th percentile human male weight, with considerations towards maximum load factors, inertial forces, and reactions between the occupant, seat, and lap belt for all flight conditions. Seats are equipped with a combined safety belt and shoulder harness with a single-point release. For young children, child seats to be added on the regular seating will be available at the hub. All projecting objects such as seat backs and railings are padded to further protect passengers.

In case of hard/crash landings, energy attenuation mechanisms within the vehicle absorb the kinetic energy of the aircraft. While a part of this energy is dissipated by allowing large plastic deformations in the landing gear and structure, the remaining energy is dissipated by stroking of the seats. The seats use variable load energy absorbers (VLEAs) that are designed to operate at different levels of g-force seat deceleration and can be adjusted depending on the weight of the passenger, to result in a maximum deceleration of 14g during a crash.

5.9 Emergency Egress

Both the side cabin door and pilot door serve as emergency exits and can be opened from inside or outside the vehicle according to 14 CFR 29, paragraph §29.809. They can also be jettisoned if needed and have backup latching if the primary latching mechanism fails. They are designed not to jam under inertial loads as specified by 14 CFR, paragraph §29.783 (d). With ample room inside the cabin, all passengers may exit in under 60 seconds through the side door or designated window exits. With the disabled passenger seating located directly next to the door without interference, a safe exit is possible without the requirement for assistance by others. In addition, the door is 180% wider and 90% taller than required as specified by 14 CFR 29, paragraph §29.807, to further simplify egress. The aircraft is highly unlikely to rollover due to its unique high double wing and fuselage design, however, in the event that it does, windows can be jettisoned to ensure an opening is available regardless of orientation with the ground. To help guide passengers in an emergency egress scenario, illuminated emergency exit signs marked with the word “Exit” are located throughout the cabin and aisle. In an emergency water landing, the fuselage and doors are designed to maximize time afloat and prevent passenger injury as required by 14 CFR 29, paragraph §25.801. In the event of structural failure, the high voltage busses are kept far away from the cabin inside the wings and are shielded by the cabin walls to prevent electrical safety hazards.

In summary, *Starling* was designed to accommodate a wide range of passengers and their specific needs. By providing ample space throughout the cabin, a private area for each seat, and reconfigurable seating,

all passengers will be able to safely fly aboard *Starling* with limited to no personnel assistance, thereby restoring passenger independence.

6 Blade Aerodynamic Design

6.1 Design Goals

Starling is a quad-tiltrotor designed to transport both able-bodied passengers and those with reduced mobility seamlessly between two urban centers at ranges that are currently not attainable by existing eVTOL vehicles. Achieving the goal of long range and requiring only a very short hover calls for a proprotor aircraft that is efficient in cruise. Figure 4.2 in Section 4 shows that the vehicle will be in hover for ultra-short periods of time. As a result, it was determined that the rotor design would prioritize cruise efficiency.

The challenging part of designing a proprotor, especially one that is expected to achieve high cruise efficiency while still being able to hover regardless of duration, is addressing the different rotor aerodynamic conditions in each flight mode. A rotor in hover experiences relatively low but entirely induced inflow. In contrast, a proprotor in cruise experiences high inflow, most of which is cruise inflow. Small-angle assumptions typical of helicopter analysis are no longer valid in cruise. These two flight modes require vastly different rotor pre-twists.

6.2 Design Procedure

The *Starling* proprotor was developed using a comprehensive procedure that involved evaluation of airfoil characteristics and use of in-house codes developed by the design team. Initial analyses of Reynolds and Mach numbers on the rotor disk were performed to aid in blade airfoil selection. Once the airfoils were selected, the lift, drag, and moment coefficients were generated for a range of angles of attack and Reynolds number using an in-house two-dimensional Reynolds-Averaged Navier-Stokes solver (2D RANS). Further analysis on airfoil C_l/C_d and $C_{l\max}$ led to the designation of inboard and outboard airfoils. In-house blade element momentum theory (BEMT) codes for hover and cruise were developed with blade-geometry-sweeping capabilities. The geometric parameters varied includes twist, taper, airfoil transitions, and inboard-outboard airfoil combinations. These codes output propeller efficiency and Figure of Merit whose values were plotted to generate a Pareto front. Once the Pareto front was generated, a design point with a high propeller efficiency and a good Figure of Merit was selected as the final blade design.

6.3 Blade Airfoil Considerations

Airfoil selection begins with analysis of Mach and Reynolds number distribution on the rotor disk. The drop in tip speed while the vehicle is in cruise significantly drops both Mach and Reynolds numbers across the disk as shown in Figure 6.1. In hover, a good portion of the rotor disk have Reynolds numbers (Re) above 1 million and Mach numbers (M) below 0.3. The values for both of these numbers decrease significantly in the cruise scenario. For $M < 0.3$, Mach numbers do not affect the airfoil lift and drag characteristics significantly; however, Reynolds number effects on airfoil aerodynamics must be considered when $Re < 10^6$. Thus, airfoil tables from 2D RANS CFD simulations generated lift, drag, and moment coefficients at a wide range of angles of attack and Reynolds numbers.

The airfoils considered, shown in Table 6.1, are a mixture of common rotorcraft airfoils, tiltrotor airfoils, and medium Reynolds number airfoils. The Boeing-Vertol airfoils, denoted VR, are well-researched airfoils that have been used on the Bell XV-15, an experimental tiltrotor aircraft. SC1095, OA209, and RC410

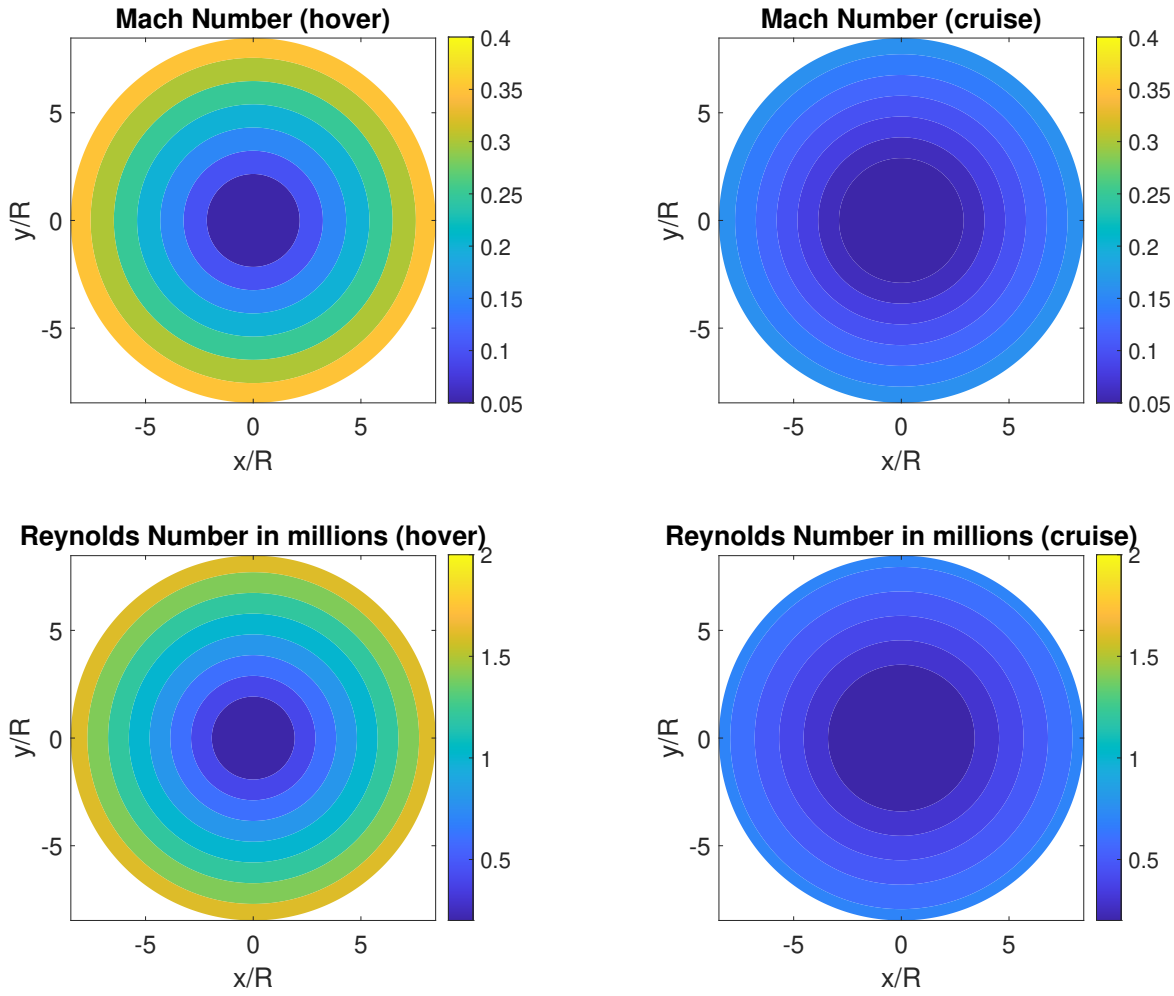

Figure 6.1: Mach and Reynolds number distributions in hover and cruise

are second-generation rotorcraft airfoils with low thickness, a property that would make them suitable outboard airfoil candidates. The MH-60 and Clark-Y are airfoils meant for high lift-to-drag ratios at lower Reynolds numbers and steady flow.

Placement of airfoils in different sections of the rotor depend on both the aerodynamic and thickness of the candidate airfoils. Optimal inboard airfoils should have a high lift-to-drag ratio at lower Mach numbers. This characteristic also tends to make these airfoils thicker, which has an added benefit of being able to absorb higher structural loads at the root. Optimal outboard airfoils aim to have great aerodynamic performance at higher Mach numbers, a characteristic associated with thinner airfoils. As a result, the candidate airfoils were placed into either an "inboard" or "outboard" group based on their thickness, and the transition point was varied as a parameter.

6.4 Blade Configuration Trade Study

Two BEMT codes were used to determine the optimal blade design for *Starling*. Two codes were needed to accurately model the rotor performance in cruise where inflow is high and swirl cannot be neglected. The same code could also be used in hover but was unnecessarily time-consuming to converge the negligible swirl.

Table 6.1: Airfoils considered for rotor design

Inboard	Clark-Y	VR-7	RC-410		
Outboard	VR-8	SC1095	OA209	MH-60	Boeing 23010

A parametric sweep of twist rate, taper, inboard/outboard airfoil combinations, and their corresponding transition locations was implemented within both codes to obtain important proprotor metrics: Figure of Merit in hover and propeller efficiency (η_{prop}) in cruise.

Certain considerations were built-in to ease manufacturing. The transition for both airfoil and and twist were set to be at the same location. Compared to existing rotorcraft, the *Starling* rotor radius has a small enough radius such that a linear taper did not improve performance significantly. A linear taper was introducted past $r/R = 0.75$ to combat profile losses near the tip [25].

A combination of the following geometric parameters were swept:

1. Inboard twist: $\theta_{\text{tw}} = -38\,\text{deg} : -42\,\text{deg}$
2. Change in twist: $\Delta\theta_{\text{tw}} = 2\,\text{deg} : 6\,\text{deg}$
3. Inboard airfoils: Clark-Y, VR-7, RC-410
4. Outboard airfoils: VR-8, SC1095, OA209, MH-60, Boeing 23010
5. Twist and airfoil transition region: $x = 0.5, 0.575, 0.65$
6. Linear taper: 1.2, 1.6, 2.0
7. Taper transition location: $x = 0.8, 0.9$

The "Change of twist" indicates how the twist rate changes at the transition location. For example, if the inboard twist is $\theta_{\text{tw}} = -38°/\text{span}$ and the $\Delta\theta_{\text{tw}} = 5°/\text{span}$, then the outboard twist is $\theta_{\text{tw}} = -33°/\text{span}$. The sweep yielded 4,050 unique blade geometries. The corresponding Figure of Merit and η_{prop} were plotted to generate a Pareto plot. The Pareto front is indicated in orange.

The green star on the Pareto front indicates the final selection. Other rotor combinations to the right of the design point sacrifice hover performance to attain a substantially minimal gain in propulsive efficiency. It should be noted that the MH-60 and Boeing 23010 airfoils performed equally well; however, there was one major uncertainty with the MH-60. Based on data from McCroskey [26], Bousman [17], and Leishman, who gathered extensive unsteady data on the NACA 23012 [27], it is well understood that the unsteady aerodynamic characteristics of an airfoil have a vital impact on the helicopter mode flight. The impact is greatest at high advance ratios which *Starling* encounters at much lower speeds due to its low tip speed. The MH-60 airfoil unsteady characteristics are unknown. Unsteady and dynamic stall test data exists on the NACA 23012 [27], a close cousin of the Boeing 23010, a Boeing airfoil modified from the NACA 23010 specifically for tiltrotor applications. The existence of unsteady data lent confidence on the Boeing 23010. Thus, Boeing 23010 is selected as the outboard blade airfoil. The variation of pitching moment with mean angle of attack is deemed satisfactory for *Starling*.

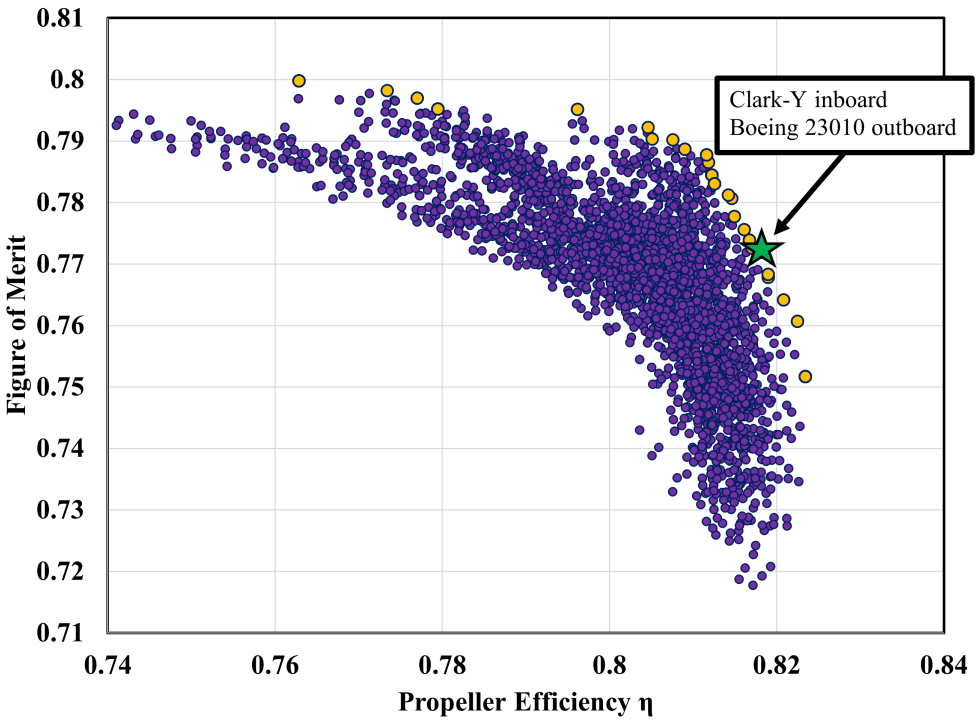

Figure 6.2: Pareto plot for blade geometries

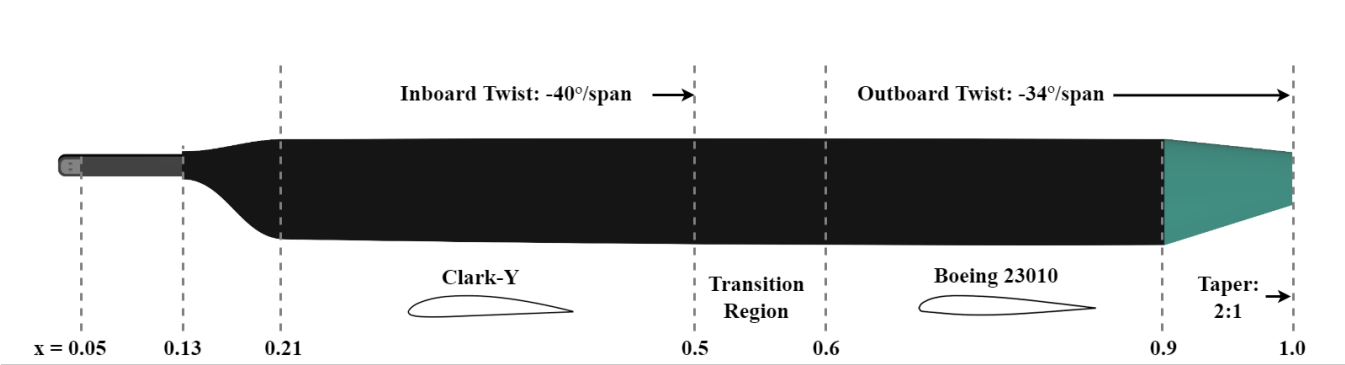

Figure 6.3: Final blade design

Table 6.2: Performance metrics and collective settings for final blade design

Property	Value
Figure of Merit	0.77
η_{prop}	0.82
$\theta_{75,\text{hover}}$	13.5°
$\theta_{75,\text{cruise}}$	54.1°

7 Blade Structural Design

The *Starling* has soft in-plane hingeless rotors with 5 blades. Glass and carbon fiber composite materials are chosen to fashion the blade spar and skin because of their high specific strength and superior fatigue properties. The internal blade structure is designed to absorb the loads and allow the motions needed in absence of cyclics generated during edgewise flight. There must be adequate stiffness in the blades in airplane mode to ensure unsteady perturbation does not lead to impact with the leading edge of the wing. Adding a forward sweep to the wings to avoid impact would be sub-optimal. Targets for first flap and first lag frequencies were set to 1.15/rev and 0.65/rev, respectively, to provide the required stiffness in flap and alleviate chordwise loading of the hub. The blades are designed for high fatigue strength, low weight, and ease of manufacturing.

An in-house developed cross sectional analysis tool was used to calculate the blade cross section inertial and stiffness properties at required spanwise locations based on ply orientation and thickness in the spar and skin. Spar placement and the addition of leading edge weights were determined to ensure the blade elastic axis and center of gravity are coincident at quarter chord. The resulting spanwise material properties were input into an in-house comprehensive code where the frequencies (flap, lag, and torsion) along with modal couplings were identified. This process was iterated until the desired frequency characteristics were achieved at *Starling* operating RPM.

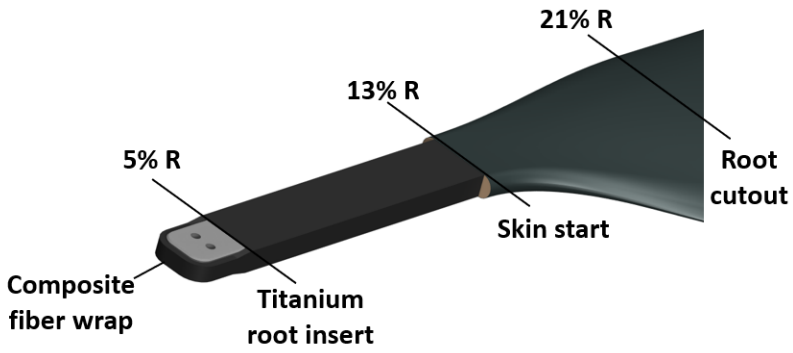

Figure 7.1: Blade root structure at $\theta_{75} = 0°$

7.1 Blade Root Structure

The blade root section spans from 5% to 21% radius, shown in Fig. 7.1. The blade spar starts as a rectangular cross section with a Rohacell 51 foam core. The spar is composed of unidirectional [0°] plies of E-glass/epoxy prepreg chosen specifically for its fatigue properties. At the blade grip, the composite fibers are split, wrapped, and cured around a titanium root insert that fits snug into the spar center, greatly improving the load transfer to the hub. From 5% to 13% span is the spar alone which maintains a constant cross section and pitch equal to the root pitch of the blade, 20.1°. The transition region from 13% to 21% span allows for smooth, direct load transfer from the blade skin to spar as well as allowing adequate space for the spar to transition slightly itself for its outer profile to match the root airfoil geometry. The spar is designed thicker at the root to reduce stress under centrifugal and oscillatory loading and plies are dropped through the transition to the blade root airfoil. The effective flap hinge of the structure is at 10% R and the root cutout is 21%. To reduce stresses under steady loading in hover, a slight pre-cone of 2.5° is added to the blades. Similarly, to reduce chordwise loading in steady axial flow (cruise), a 12 mm (0.5 in) torque offset is added.

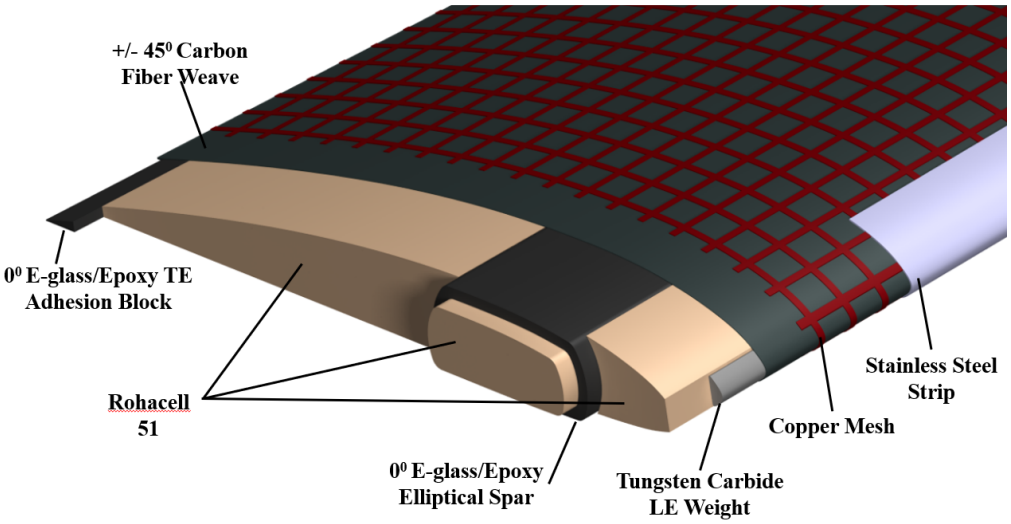

Figure 7.2: Blade internal anatomy with materials

7.2 Blade Internal Structure

The elliptical spar is the primary structural member that transfers the centrifugal force to the hub. The blade cross section is shown in Fig. 7.2. A "hollow" spar is desired to provide the necessary stiffness at a relatively lower cost-to-weight. The spar is positioned from 17% to 33% of the chord to maintain the appropriate elastic axis. The center of gravity is placed inline with the pitch axis at quarter chord via distributed tungsten carbide leading edge weight, providing generous pitch-flap stability margins. The leading edge weights are broken into 20 equivalent segments along the blade to ensure they do not contribute to the stiffness of the structure. For the foam core material, Kevlar honeycomb, Rohacell 51, and Rohacell 75 were evaluated. The Kevlar honeycomb is lower in density (34 kg/m^3) than either Rohacell (52 kg/m^3 and 75 kg/m^3 respectively), but is more difficult to machine precisely. A core for the spar is necessary to maintain the inner spar profile if the blade is to be manufactured as one continuous structure, therefore the honeycomb was dropped from consideration. Rohacell 51 is lighter and provides the necessary additional mass to achieve the desired frequency targets, thus it is selected as the core material for the spar as well as the blade to preserve aerodynamic profile of the cross section. A trailing edge E-glass/epoxy block of 2% chord is added to reinforce the trailing edge of the blade and provide adequate surface area to bond the upper and lower skin. The blade skin is composed of [$\pm$45°] plies of carbon fiber epoxy weave, greatly increasing the torsional and chordwise stiffness of the blade. To prevent wear and erosion, the blade is coated in polyurethane elastomer. Due to the electrically insulating properties of E-glass, the entire blade is wrapped with a copper mesh sleeve to provide an electric current path spanwise to the hub in the event of a lightning strike, avoiding electrostatic charge build-up and damage to the blade in accordance with 14 CFR 25.581. Lastly, a stainless steel strip is placed on the leading edge for abrasion resistance. De-icing mechanisms were avoided based on the mission characteristics and would add unnecessary complexity to the design.

7.3 Blade Manufacturing

The blade spar and titanium root insert would be fabricated together. The foam core would first be machined to maintain the inner profile of the blade spar from grip to tip. Next, the titanium insert is machined to have a toothed end that matches the root spar inner profile. The E-glass/epoxy laminate is

cut at one end such that the fibers flare and can be wrapped around the root insert. Composite laminate is wrapped around the foam and tooth of root insert to achieve the desired spar thickness throughout. The spar assembly is placed in a vacuum mold and cured in an autoclave.

As the spar cures, the leading-edge weights and foam can be machined. Upon completion, each component is stacked and glued accordingly. This entire assembly is wrapped with the two [±45°] plies of carbon fiber epoxy prepreg. Due to the high blade twist, transition in airfoil geometry, and the skin transition region, draping techniques are employed appropriately to ensure a wrinkle and deformity free product. A mold is produced with a shallow indent on the leading edge for the stainless steel strip. Final curing is achieved in an autoclave.

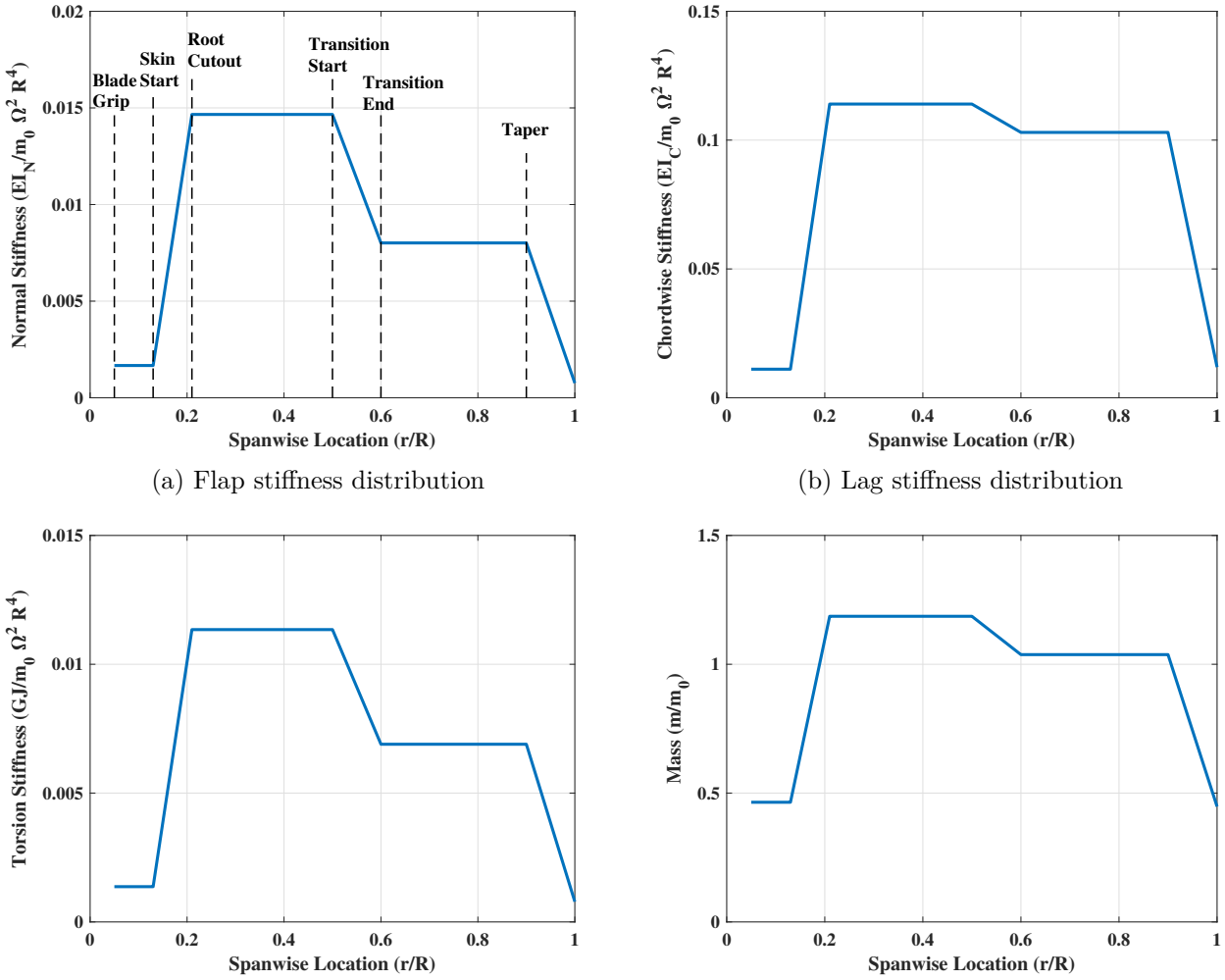

(a) Flap stiffness distribution

(b) Lag stiffness distribution

(c) Torsion stiffness distribution

(d) Mass distribution

Figure 7.3: Rotor Blade Sectional Properties

7.4 Rotor Blade Sectional Properties

Each individual blade weighs 3.14 kg (6.29 lb). So 20 blades would weigh 62.74 kg (138.3 lb). Figures 7.3(a) through 7.3(d) show the non-dimensional mass and stiffness distribution of the blades. The blade grip clamps at 5%R. The spar and skin transition are responsible for the increase in stiffness and mass from 13% R to 21% R. Outboard of the root cutout, the sectional properties are obtained from the skin,

spar, leading edge weights, and foam core. The discrete changes in properties outboard of the root cutout are due to ply drop-off as the airfoil transitions to a thinner profile and tapers at the tip.

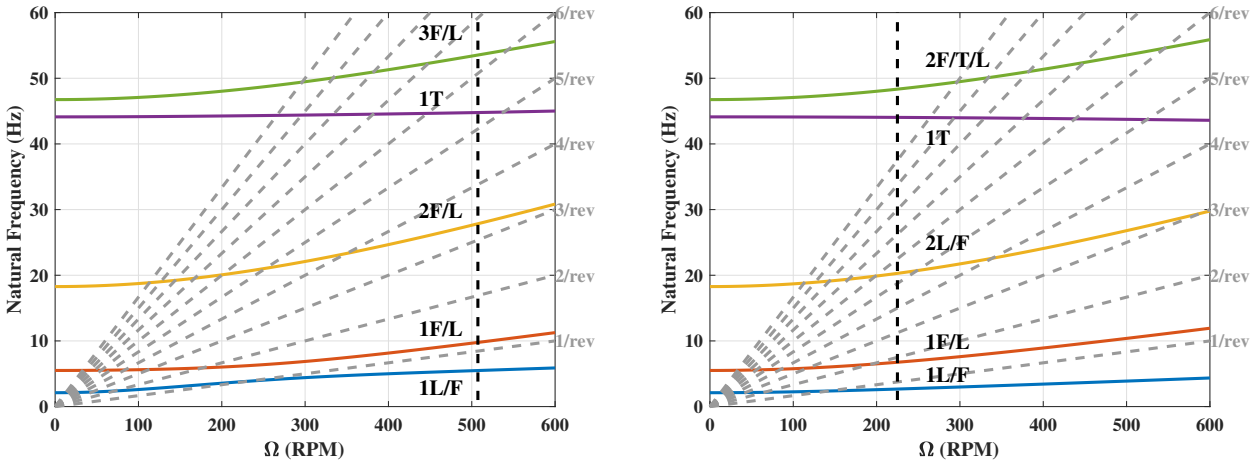

(a) Hover RPM fan plot

(b) Cruise RPM fan plot

Figure 7.4: Fan plots showing first five rotor frequencies at hover and cruise RPM

Table 7.1: Hover RPM natural frequencies

Frequency (/rev)	Hover 507 RPM
1st Lag/Flap	0.65
1st Flap/Lag	1.15
2nd Flap/Lag	3.29
1st Torsion	5.30
3rd Flap/Lag/Torsion	6.34

Table 7.2: Cruise RPM natural frequencies

Frequency (/rev)	Cruise 225 RPM
1st Lag/Flap	0.71
1st Flap/Lag	1.80
2nd Lag/Flap	5.40
1st Torsion	11.75
3rd Flap/Lag/Torsion	12.80

Fan plots, one each for hover and cruise, of the rotor blade are shown in Fig. 7.4. As the blades are pitched, lag becomes softer and flap stiffer. The variation in collective between hover and cruise is 13.5° to 54.1°. Due to the high blade twist, the modes are highly coupled so the dominant mode is listed first. The plots show that the blade natural frequencies are well separated from the 1 to 10/rev harmonics at the operating conditions. In the transition from helicopter to airplane mode, it is necessary to cross several resonant frequencies. The reduction in RPM is initiated after the pylons are fully tilted to airplane mode to reduce oscillatory loading. The drop in RPM is performed quickly to minimize the impact of these adverse operating conditions. Necessary torsional stiffness is achieved through tuning the pitch link stiffness, resulting in a fundamental torsion frequency of 5.3/rev.

7.5 Aeroelastic Stability Analysis

Aeroelastic stability analysis was performed to ensure high stability margins for *Starling*. Pitch-flap and flap-lag couplings were considered throughout the design of the rotor by eigen-analysis and the identification of stability boundaries using appropriate mass, damping, and stiffness properties of the rotor itself.

Flap-Lag flutter arises from aerodynamic perturbations in the flap and lag modes that forces the lag motion into an unstable condition. Generally, rotors that are stiff in both flap and lag are susceptible to this phenomenon. Detailed analysis of the blades showed stability in both hover and cruise operating conditions. Due to the high twist of *Starling* blades, further analysis was carried out to identify the

boundaries of this instability and ensure adequate margins. Figure 7.5 shows the flap-lag flutter boundary at hover conditions in the form of egg plots with increasingly negative twist rates. Blade loading is held constant at $C_T/\sigma = 0.16$. It was observed that this instability is subdued by the introduction of twist which is useful because lag dampers are difficult to incorporate in hingeless hubs. The *Starling* blades have an average twist rate of $-37°$, much greater than those in Fig. 7.5. With this high twist, no flutter boundary exists at any operating blade loading and the rotor would stall in edgewise flight before this mode reaches instability. In cruise mode, the aerodynamic lag damping increases significantly and no flutter boundary exists at all. Figure 7.6(a) shows the eigenvalues obtained at the design frequencies. *Starling* is free of flap-lag flutter in all operating conditions.

Pitch divergence and pitch-flap flutter were analyzed, the boundaries of which can be seen in Fig. 7.6(b). Pitch divergence is a static instability resulting from coupling between lift and centrifugal force. Offset between these two forces result in a twisting motion of the blade that may cause failure. The location of the elastic axis is unimportant. Pitch-flap flutter is the dynamic instability from lift and centrifugal coupling about the pitch axis. The most effective means to mitigate this is to ensure the pitch axis and blade center of gravity are in line with the aerodynamic center, usually around quarter chord. Therefore, the rotor blade pitch axis and C.G. are placed at quarter chord, quelling all pitch-flap instability concerns. A high fundamental torsional frequency was selected to further increase this stability margin.

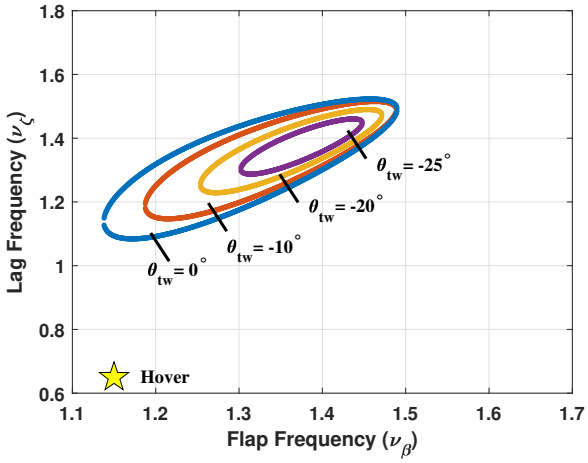

Figure 7.5: Flap-lag flutter boundaries at $C_T/\sigma = 0.16$ with increasing twist rate

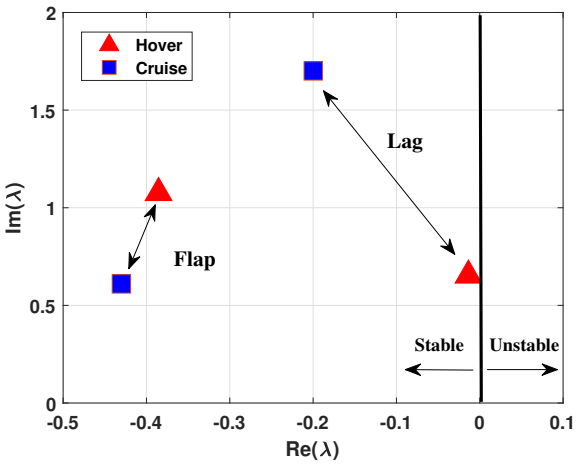

(a) Flap-Lag eigenvalues in hover and cruise

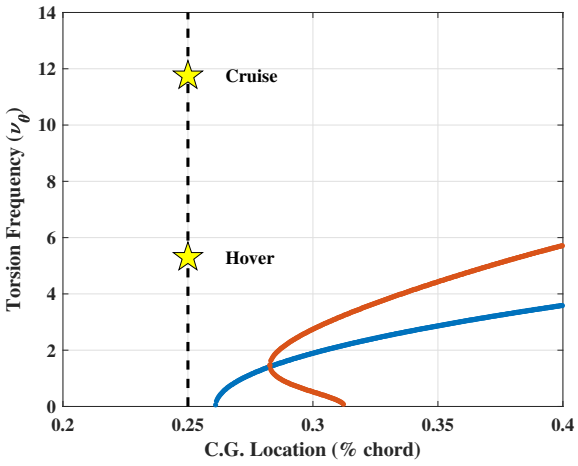

(b) Pitch divergence and flutter boundary

Figure 7.6: Flap-lag and pitch-flap stability margins

7.6 Ground Resonance

Ground resonance is a mechanical instability typically seen in soft in-plane rotors that arises from rotor lag modes coupling with the landing gear/body pitch and roll modes. A simplified, single rotor model was analyzed as it models the worst case scenario. Four rotors equally spaced about the body rotating in their

respective directions is expected to have a cancelling/stabilizing effect. Figure 7.7 shows the coupled ground resonance results for the *Starling* rotor, from which it can be seen that the body modes and lag modes are clearly separated in the operating range. No additional lag damping is required. The first coalescence is roughly 50 RPM (10%) above nominal hover, therefore motor speed limitations will be incorporated into the control system to ensure the rotor never exceeds 550 RPM.

7.7 Stress Analysis

A detailed analysis of the blade and flexure was performed using the high-fidelity US Army/University of Maryland code X3D [28]. This solver uses three-dimensional (3D) finite elements to model the structure from first principles and capture the dynamic stresses. The main objective of this analysis was to capture the stress concentrations throughout the structure and ensure that an acceptable factor of safety of 1.5 was maintained. The analysis was conducted at several flight conditions, but the results are only shown for the case that produced the highest loads: edgewise flight at $\mu = 0.3$.

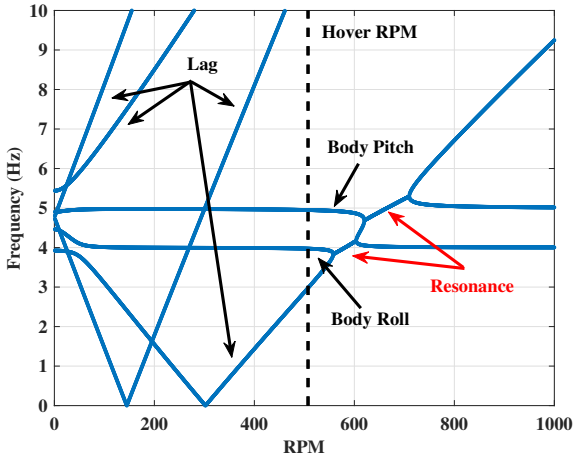

Figure 7.7: Stability from ground resonance

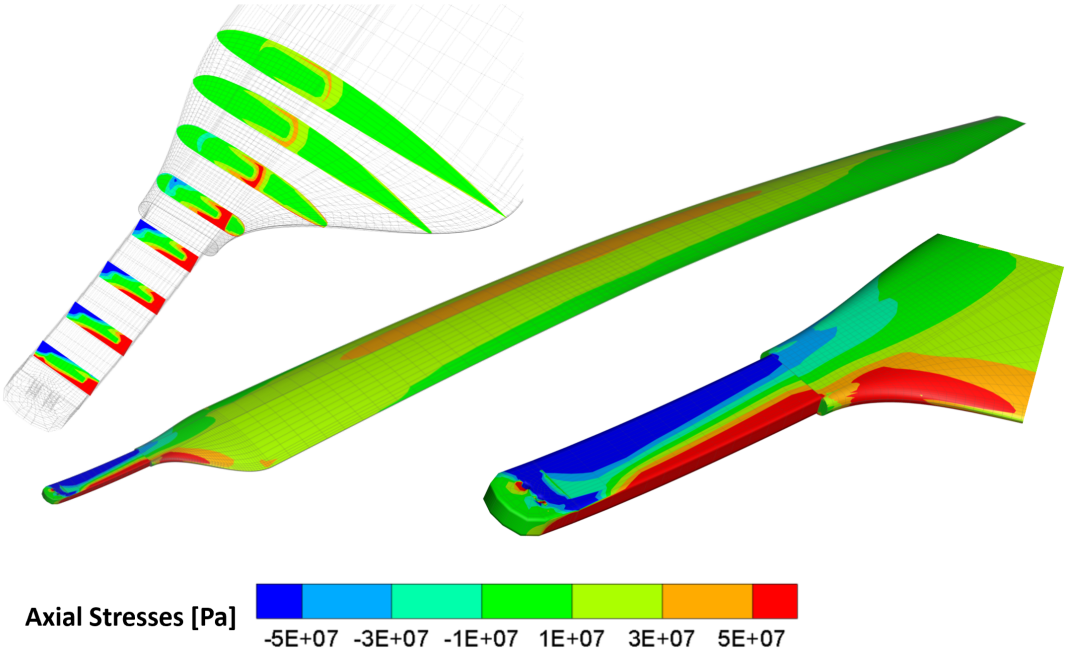

Figure 7.8: Axial stress distribution of *Starling* blade and flexure at edgewise flight, $\mu = 0.3$.

Figure 7.8 shows the stress distribution in the blade at azimuth $\psi = 104°$. The contour limits shown in the figure were lowered from the maximum stresses to better illustrate the variation. There is tensile stress concentration at the top surface of the blade near mid-span due to the blade pre-cone. However, the highest stresses understandably occur near the root. Zooming into this area, high compressive stresses are observed on the top surface due to the lift, with the bottom surface having high tensile stress. The maximum tensile stress in the spar is approximately 300 MPa, which gives a factor of safety over 1.5.

Similarly for compressive stress, a factor of safety of greater than 2 is achieved. The maximum von Mises stresses in the root insert were approximately 500 MPa, which is why titanium was used over aluminum to produce a factor of safety over 1.75. A chordwise stress variation is also seen in Figure 7.8. This is due to the lead deflection of the blade flexure. The load flows from the flexure to the bolt holes through the plies wrapped around the root insert, which is seen in the stress concentrations at the leading and trailing edges. To accommodate these high stresses, extra plies were added to wrap around the root insert. Lastly, looking at the blade cross-sections, it is observed that the majority of the stress is carried by the blade spar, and there are no unusual stress concentrations seen in the transition region.

To summarize, the rotor blade of *Starling* was designed to achieve the targeted frequencies and to be free from aeroelastic instabilities. A high-fidelity 3D analysis was also performed to verify and refine the design.

8 Hub Design

Conventional tilt-rotors employ a gimballed hub. The gimbal allows the blades to cyclic flap freely, greatly alleviating hub loads in edgewise and transition flight. Flapping introduces kinematic pitch-flap coupling through a pitch link offset angle $-\delta_3$ which separates the lag frequency from flap and allows for stable axial flight up to the whirl flutter boundary [29]. However, the gimballed hub can be bulky, complex, and unable to accommodate five blades with sufficient spacing of pitch links for $-\delta_3$. Five blades are crucial for noise, however the trade-off is high loads in helicopter mode justified by the small hover and transition time.

8.1 Hub Selection

Figure 8.1 displays the hub selection criteria. Each hub type is ranked relative to the gimballed hub with the scale as + (better than), 0 (comparable to), and - (worse than). A compact and simple hub is essential as four of them must be produced. Larger hubs increase nacelle size and hub drag, significantly hindering performance. A high collective range is necessary to achieve collective targets in cruise, allowing for increased propulsive efficiency and additional margins are needed for controllability. As *Starling* will operate in urban environments, gust tolerance is important. Lastly, a higher number of blades is desired relative to conventional tilt-rotors to blend into urban soundscapes. The available space around the hub becomes a limiting factor.

Hub Type	Complexity	Compactness	Collective Range	Gust Tolerance	Blade Number	Total
Gimbal (baseline)	0	0	0	0	0	0
Articulated	-	0	0	+	0	0
Hingeless	+	+	0	-	+	+2
Bearingless	+	+	-	-	+	+1

Figure 8.1: Hub selection

With four main rotors, the *Starling* does not require cyclic controls to achieve adequate control authority

in all flight conditions. Simplifying the swashplate design to collective-only removes gimballed hubs from consideration as there is no longer control over the tip path plane. Despite the increased gust sensitivity, the hingeless hub is the ideal choice for the given mission requirements. Hingeless hubs come with higher loads. Therefore, a soft in-plane design is preferred. The Boeing Vertol company developed a hingeless tilt rotor hub in the 1970s and conducted tests in the 40×80 ft wind tunnel at NASA Ames, proving their design was free of aeroelastic instability at high speeds [30]. Therefore, similar frequency targets were chosen for *Starling* at a 1st lag frequency of 0.65/rev and 1st flap of 1.15/rev.

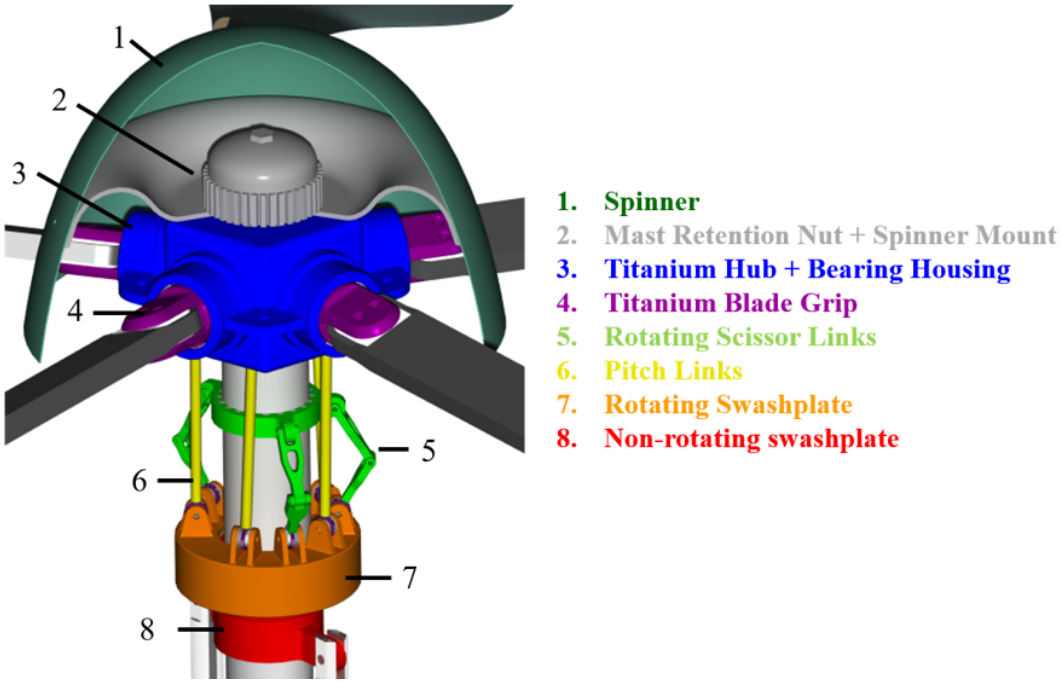

Figure 8.2: Hub assembly

8.2 Hub Assembly

The hub assembly is shown in Fig. 8.2. It is a two piece assembly that doubles as a bearing housing and is made of titanium alloy (Ti-6Al-4V). Titanium offers the highest strength to weight ratio, allowing for a more compact design. It is a hollow assembly that the main rotor mast passes through and is secured on top by a mast retention nut which is threaded according to the direction of rotation, e.g. counter clockwise rotation to right hand threaded nut. The mast is toothed where it passes through the housing such that it transmits torque equally through the upper and lower casing. The lower casing has precise cutouts for the pitch links as pitch actuation is achieved from inside the hub gap. The joint between the pitch link and pitch horn is a spherical ball joint to alleviate bending stresses and provide a wide range of motion. *Starling* has a collective range of 65°.

The blade grip adapter is a cylindrical piece of titanium machined to have a flared back end with a pitch arm that rests inside the hub, shown in Fig. 8.3(a). The bearing stackup consists of a thrust bearing and a needle roller bearing which transmit the centrifugal force and bending moments to the hub. The hub is designed with lips to fix the outer race of the needle bearing to the fixed race of the thrust bearing as well as to provide some surface area for the thrust bearing to transfer axial load to the hub directly. The thrust bearing is sized for maximum loading of 40 kN and the needle bearing for 1.5 kN for a high margin of safety. This assembly allows the blades to be freely rotated about their pitch axes while providing sufficient

load transfer. Appropriately sized shoulder bolts connect the blade and the blade grip adapter. Similarly, shoulder bolts are sized to secure the upper and lower hub casing together.

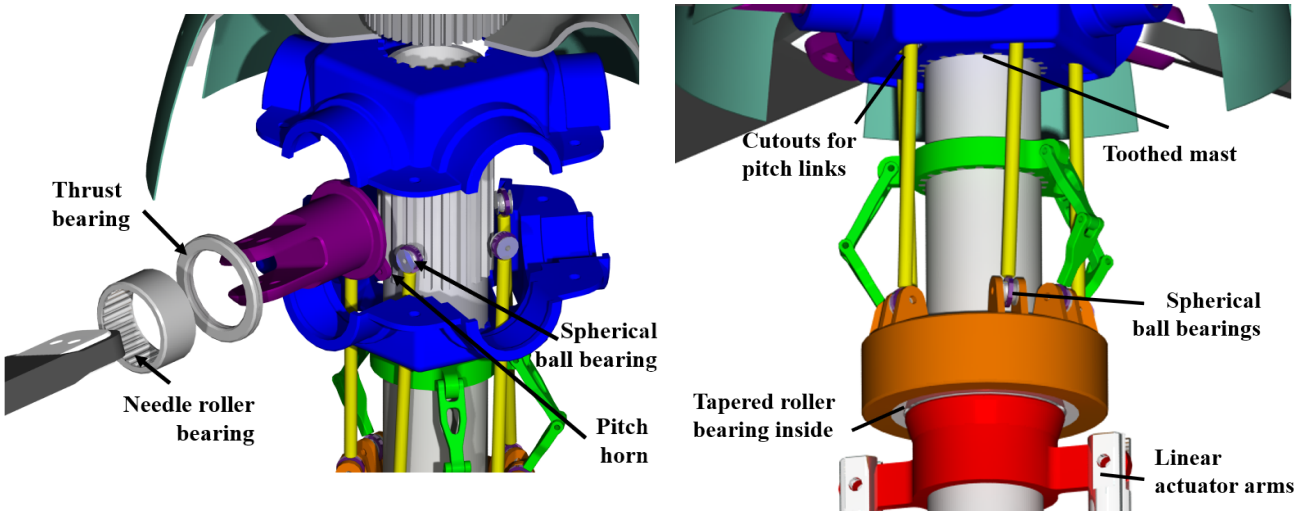

(a) Exploded view of bearing stackup and hub housing

(b) Swashplate features

Figure 8.3: In-depth component details of the hub and swashplate assemblies

8.3 Swashplate Design

The swashplate is designed for collective control only, greatly simplifying the control mechanism. The pitch links are 132 mm (5.2 in) long and are specifically designed for a high range of collective. Since the pitch links have an angular spacing of 72°, three scissor links are necessary for symmetric transfer of torque from the mast to the rotating swashplate and are secured to the mast via a splined collar, shown in Fig. 8.3(b). The non-rotating swashplate is itself a sleeve bearing with a teflon coating allowing it to slide freely along the rotating mast. The inner race of a tapered roller bearing is press fit on to the non-rotating swashplate while the rotating swashplate is press fit on to the outer race. The tapered roller bearing allows for axial force transfer in both directions while permitting rotation of the pitch link assembly. Actuation of the non-rotating swashplate is accomplished via linear actuators mounted to the pylon structure and the stroke length required to achieve the full collective range of 65° is 38 mm (1.5 in). The actuators are based off of Thomson linear electric linear actuator MD24A025 with a nominal stroke length of 50 mm (1.97 in) and a maximum stroke speed of 52 mm/s (2.05 in/s), providing sufficient control authority. The pitch links are sized to absorb the rotor loads with a margin of safety of 5.0.

8.4 Gearbox

To generate the greatest motor efficiency, electric motors should generally operate between 2000 and 5000 RPM. Because the rotor spins at 508 RPM in hover and 226 RPM in cruise, the motor efficiency would be too low for a direct drive system. Thus, a gearbox is needed to allow the BLDC motor to operate in a higher and more efficient RPM range. As found from Section 3, a gear ratio of 7.9:1 is required to keep the motor RPM in an operational range where the motor efficiency is between 94 and 95% for both hover and cruise. A planetary gearset was chosen as it provides a clean and linear design that can be connected directly to the motor shaft and can be kept within the tight area of the nacelle. In addition, a planetary gearset has low energy losses and increased safety and reliability due to the inherent redundant drive paths. Bearing forces are applied evenly with all radial forces reacted as hoop stress in the ring

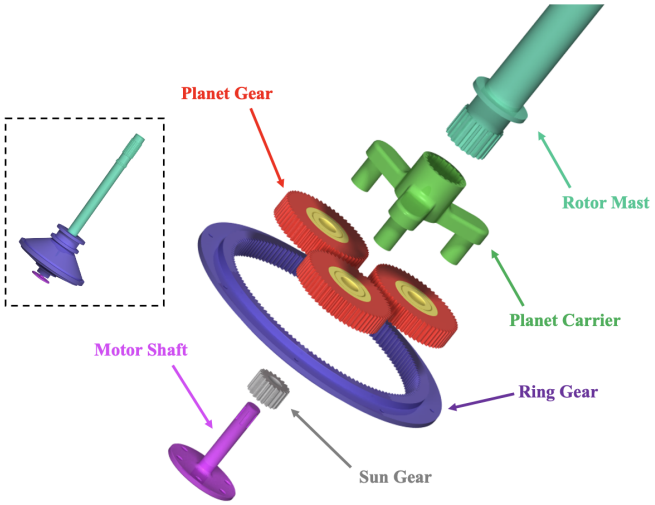

Figure 8.4: Gearbox Design Exploded View

gear. The relative size of the gears is reduced by increasing the number of planets in the gearset allowing the torque to be split among the planet gears. For additional compactness, the ring gear is non-rotating and serves as the outer casing. For material, the gearbox uses a magnesium-zirconium alloy because of its good heat-resistance and stiffness properties as well as its relatively low weight. The final gear selection quantities are presented in Table 8.1.

Table 8.1: Planetary gearbox parameters and quantities

Parameter	Sun	Planet	Internal Ring
Number of teeth	20	59	138
Module (mm)	2	2	2
Pressure angle (deg)	20	20	20

Since acoustics is a principal configuration driver, steps are taken to reduce the noise of the gearbox. First, high precision gears are used. That is, pitch error, tooth profile error, runout error, and lead error are all small. Second, the gears have good surface finishes to improve the smoothness of the tooth surface. Third, backlash in the gearing is correctly sized to prevent a pulsating transmission. Fourth, the transverse contact ratio is increased by a decreased pressure angle and increased tooth depth. Lastly, high viscosity lubrication is used to keep the lubricant film on the surface. To prevent noise from the gearbox escaping, noise dampening paint is used on the gearbox housing for noise insulation [31].

9 Propulsion System and Fault Tolerant Architecture

The propulsion system for *Starling* was designed to minimize weight while maximizing efficiency and safety. Although the idealized 400 Wh/kg battery is beyond current battery specific energy of 150-250 Wh/kg, it is still below 11,889 Wh/kg of Jet A fuel. However, distributed lightweight and reliable electric motors with high efficiency (85-95%), gear-reduction, and a wider RPM range can make up for these losses. In addition, using multiple electric motors provides other advantages such as mechanical simplicity, lower current levels, distributed thrust, and fault tolerance. Batteries can be designed such that there are no single points of failure, allowing for the entire mission to be completed even with multiple pack failures. To ensure the best overall propulsion architecture, the battery and motor were considered as a coupled

system, rather than two separate units. The final motor selection and battery architecture of *Starling* represents the best combination of simplicity, weight savings and safety.

9.1 Detailed Motor Selection

With a required total vehicle hover power of 423 kW (576 HP), operating torque, and RPM found from Section 4, 12 EMRAX 228 motors were chosen as they satisfied the operating requirements with a maximum continuous torque of 125 Nm (92 ft-lb) at 4000 RPM (62 kW continuous) and operating with an efficiency of 94% to 95% across the operating RPM range. Due to the additional torque required for fault tolerance, each motor operates below 75% of their peak continuous torque level. Therefore, liquid cooling is not needed as the motors operate within the power limits for air cooling. For each motor, a Cascadia PM100Z inverter capable of a continuous operating power of 90 kW was chosen as it has 45% greater power than required, thereby avoiding the need for liquid cooling. The inverter has built in diodes for reverse current protection. In a motor out scenario, the remaining two motors in the stack stay below the maximum continuous operating torque limit with similar efficiency. In nominal flight without a motor fault, the vehicle has a total of 623 kW (835.5 hp) or 47% more power than required for steady hover.

9.2 Battery Design

The battery was designed to meet the energy demands of the mission while maximizing safety. To size the battery, lithium-ion 18650 cells with a voltage range of 4.2 V at beginning of life (BOL) and 3.0 V at end of life (EOL) were assumed with a nominal voltage of 3.7 V. A capacity of 3,800 mAh was chosen as this is the standard cell type used in modern high-power applications [32]. To determine an estimate for the battery volume and shape, a Tesla Model S module was used for reference. A single Tesla module contains 444 18650 cells and consumes a true volume of 0.0158 m^3. In addition to the cells, this volume includes the structure, battery management system, insulation, and liquid cooling channels. Based on the dimensions of an 18650 cell, 444 cells packed tangentially consume 0.00935 m^3 or 70% greater volume than the true volume of a Tesla module. This empirical correction metric was later used to size the battery's volume.

With the EMRAX 228 motors capable of running up to a maximum voltage of 680 V, an operating voltage of 600 V was chosen over the more typical 400 V architecture. These voltage levels were compared in Table 9.1. The full criteria considered were: 1) Safety: Lower voltage systems are preferred to avoid electrical arcing and reduce insulation. 2) Weight: Higher voltage systems are preferred to reduce wire gauge due to resistance in wire. 3) Maturity and Certification: Proven and readily available technologies are preferred to ensure safety and rapid certification. 4) Lifecycle Cost: Total cost to source raw materials, fabricate, manufacture, operate and maintain the battery and electrical components. 5) Charge Time: Although voltage is not a factor in C-rate, ground support battery chargers are limited due to state of the art and by voltage level. Issues such as self-discharge and capacity fade are important phenomena that were also considered.

Table 9.1: Operating voltage level Pugh matrix

Criteria	Weights	Normalized Weights	600V System	400V System
Safety	5.00	0.31	0	1
Weight	4.00	0.25	0	-3
Maturity and Certification	3.00	0.19	0	1
Lifecycle Cost	2.00	0.13	0	1
Charge Time	2.00	0.13	0	-1
Score			**0.00**	**-0.25**

To achieve 600 V nominally, 162 cylindrical cells are connected in series using a busbar to form a lattice structure. To achieve the required energy, there are two different modules that are placed in the front and rear of the wing box. For the front wing box battery module, there are three series sets connected in parallel with a voltage controller. For the rear wing box battery module, there are four series sets connected in parallel. Thus, in either battery module, there is a total of 486 and 648 cells that together make 11.4 and 15.2 Ah at 600 V. Each battery module is housed within interstitial support and controlled for voltage, temperature, and balance in case of a cell-loss. In total, there are 12 front and 12 rear battery modules connected in parallel that together make 319.2 Ah at 600 V (192,000 Wh). These packs are fused and controlled by contactors. The number of parallel modules was determined from energy and power at the EOL and the maximum was selected. The two battery module types are respectively identical with the same battery layout to simplify manufacturing and maintenance. Critical elements of the battery pack design such as contactors, high voltage interlock, over-current protection, and fusing to prevent arc flash and over-current at the module/cell level are included in the battery overhead. The modules are placed within the wing and near the fuselage to reduce vehicle inertia and remove potential risk of battery fire injuring passengers within the cabin. In addition, the pack housing has rupture discs to vent rapid pressure increase by allowing gas build up to vent out. In the event of a collision, the leading edge battery pack has reinforced structure to prevent cell damage. The 18650 cell pack geometry was designed to fit within the constraints of the wing and the battery modules are flush with the lower surface. Panels under the wing can be removed to expose and remove a single battery module for regular maintenance and pre-flight monitoring.

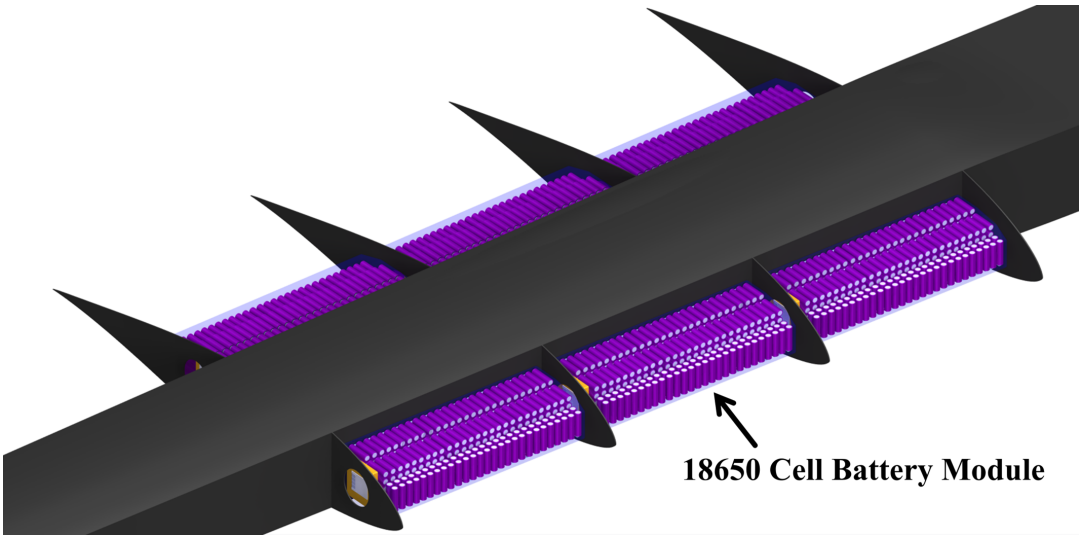

Figure 9.1: Internal view of 18650 lithium-ion battery cell module inside half span wing

The battery was found to be energy limited rather than power limited, and sized to match this specific energy. The C-rate of the battery cell is a specific power metric used to specify the ratio of a battery cell power to energy. To accomplish EOL hover, a C-rate of at least 2.5 C is required. Thus, a 3 C battery cell is used so that *Starling* is still capable of hover with a depleted battery.

Rather than using an additional battery to power auxiliary components such as the actuators and avionics, a 600 V to 24 V DC-DC converter connected to the main battery is used. A DC-DC converter will ensure that the percentage energy available for the actuators is consistent with the main battery, thereby ensuring that the actuators will not run out of energy before the main rotors and vice-a-versa. In addition, this simplifies the charging infrastructure as only one charger at the 600 V level will be needed, further saving weight. The 24 V auxiliary voltage was chosen as this is the standard for FAA use, and thus, a large variety of actuators and other electrical sub-systems are commercially available. The 24 V DC-DC auxiliary voltage is self-regulated and will continuously provide 24 V across the range of the battery voltage (486 V to 680 V). As a precautionary measure, the auxiliary components were selected to continue operating with a 20 V to 30 V off-nominal margin.

9.3 Fault Tolerance

Starling is capable of continued safe flight following any single failure of the electric power distribution system. For each rotor, there are three motors, such that if one motor fails, the remaining two motors will still output the same required torque and RPM to drive the rotor. Each of the three motors has a single motor inverter. To power the motors, there are 24 separate batteries linked in parallel. By connecting the batteries in parallel, if a single battery module fails, the voltage of the resultant total battery will remain unchanged. However, the total energy capacity will decrease due to these failures. As shown in Figure 9.3, six of these batteries can fail at the start of the mission and the vehicle can still complete the full 160.9 km (100 mi) mission based on the 20 minute cruise reserve.

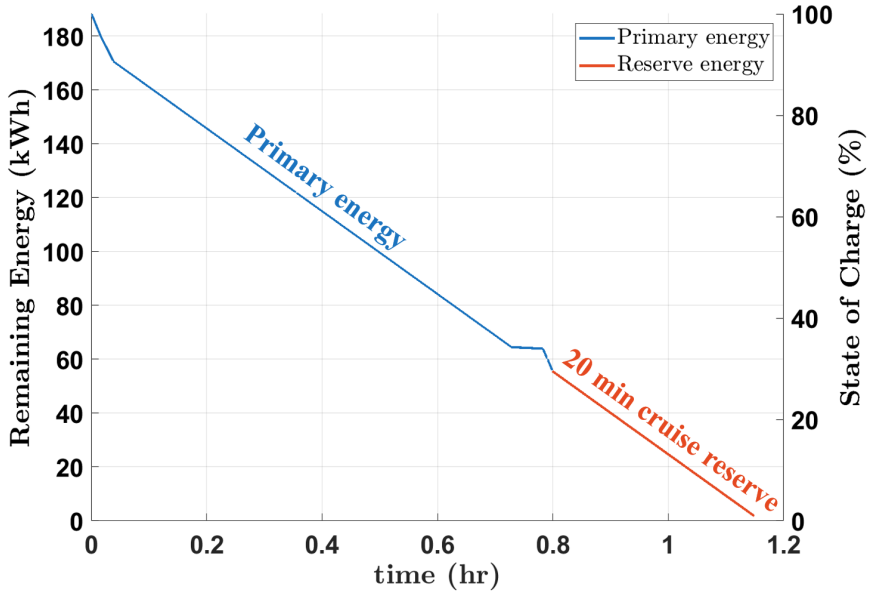

Figure 9.2: Remaining vehicle energy vs. time for 160.9 km (100 mi) mission

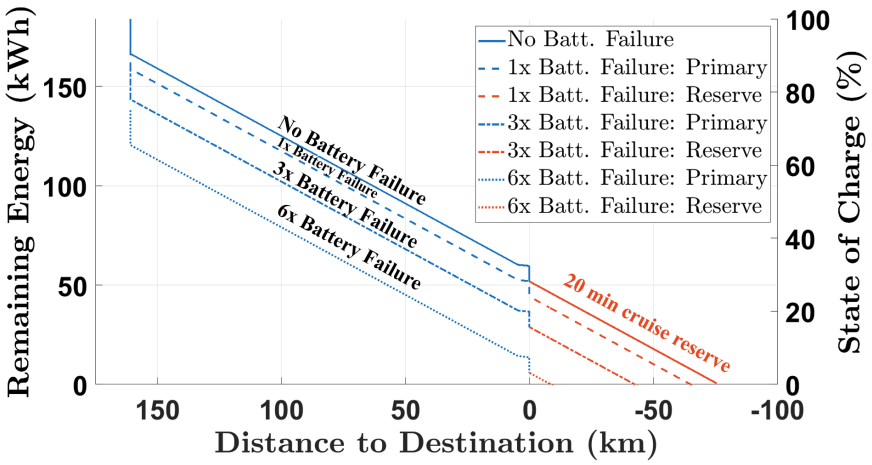

Figure 9.3: Remaining vehicle energy vs. distance to destination for 160.9 km (100 mi) mission with varying number of battery module failures

Figure 9.4 shows a simplified schematic of the 24 batteries, 12 motors, and 12 inverters with parallel wire connections to ensure single point of failure fault tolerance. Similarly, Figure 9.5 shows a simplified schematic of the 8 tiltrotor actuator motors, 8 control surface actuators, and 2 DC-DC converters.

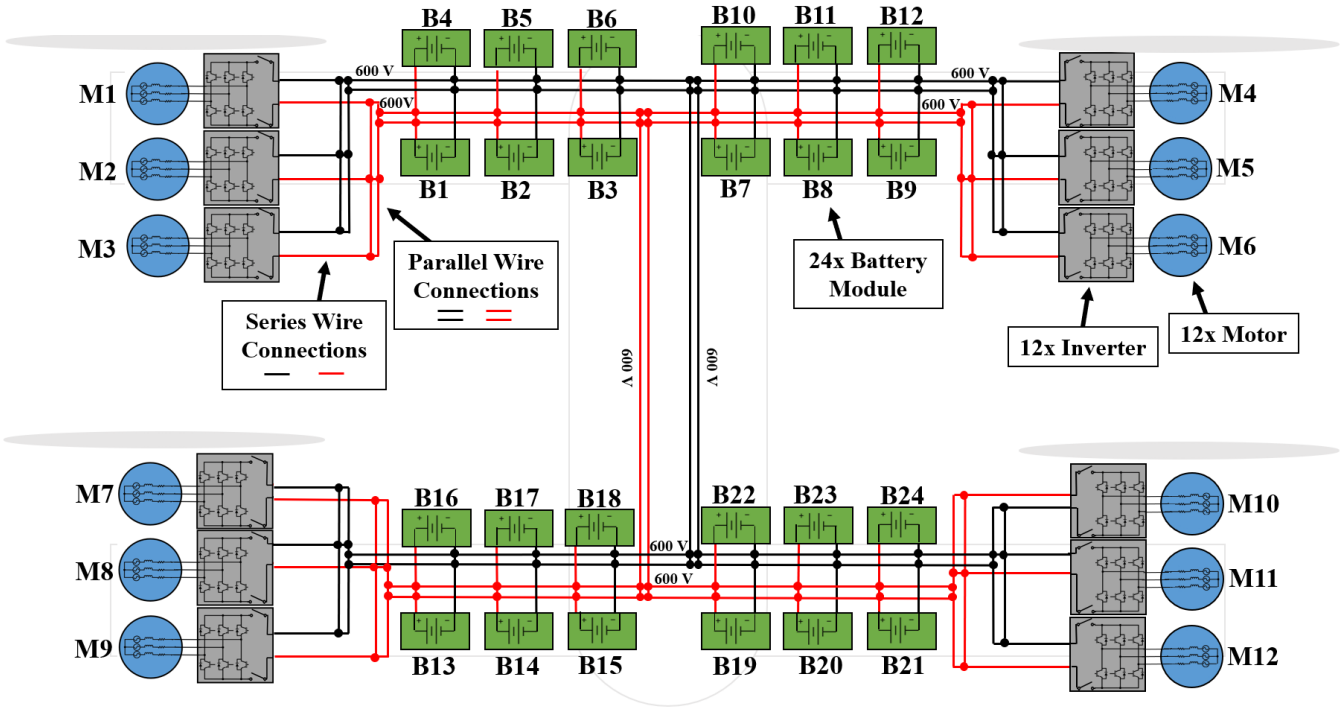

Figure 9.4: Diagram of fault tolerant propulsion system.

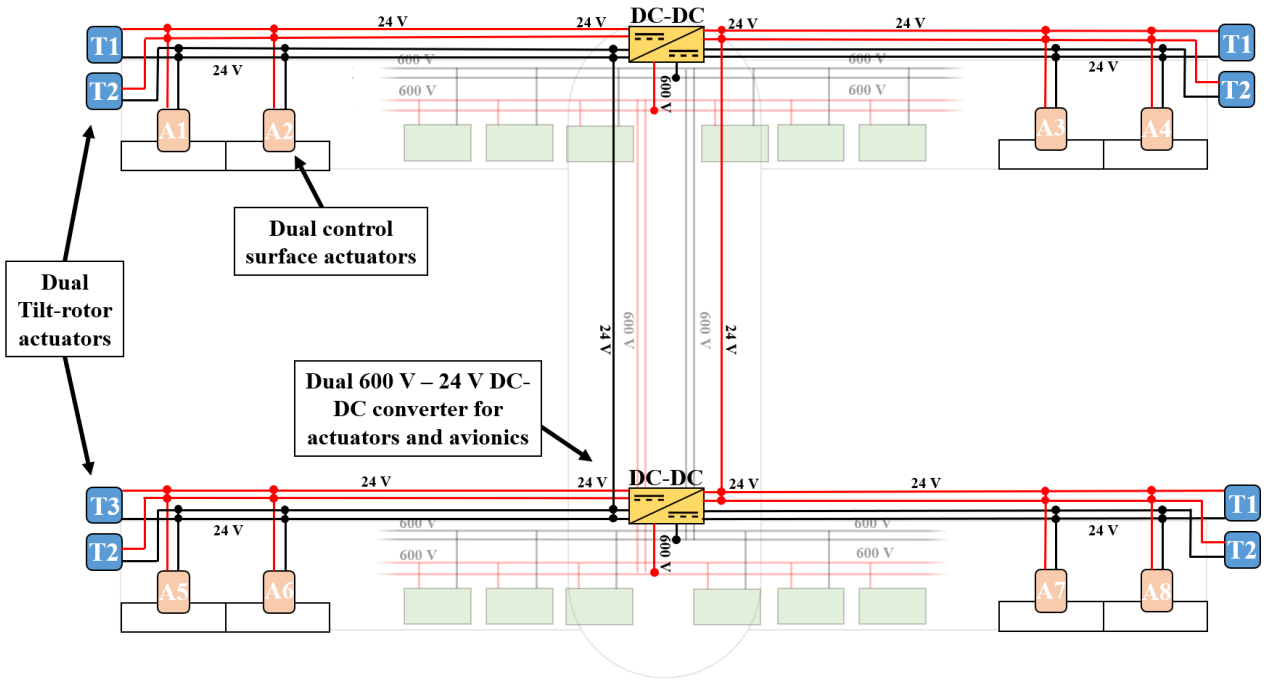

Figure 9.5: Diagram of fault tolerant actuator system

The reliability of components is both a function of time and failure rate. To maximize reliability and reduce failure rate of critical components, an initial burn-in period should be performed and components should be replaced before wearout failures occur [3].

As defined by the RFP, the aircraft must fly to 100 ft altitude which is inside the helicopter dead man's curve. In the extreme case of a failure near the ground and not covered by fault tolerant measures, *Starling* can still glide to the ground due to the two large wings for a reasonably safe touch down.

9.4 Cable Sizing

Primary 600 V and auxiliary 24 V cable gauge was determined based on end of life hover current requirements with tolerance for parallel wire faults. The length of the cables were found based on routing in the fuselage and wings with respect to battery and component (inverters, actuators, etc.) load placement. An additional 5% margin was included for installation purposes. The area of the conductor was then found based on the current for a single cable using a resistivity constant for copper of 1.72×10^{-8} Ωm. The number of strands in the cable was also considered. With greater strands, the cable can be more flexible, but the DC resistance is greater due to air gaps between the strands. In addition, cables with greater strands are more susceptible to vibration and corrosion. Ultimately 30 strand 6 AWG cables were chosen to route power between the two wings and 21 strand 8 AWG were chosen to route power from the batteries in the wing to the inverters. The total conductor weight is then 11 kg (24 lb). With insulation, the total cable weight is 12.1 kg (26.7 lb). Following similar methodology, the total auxiliary cable weight using 21 strand 8 AWG cable is 9.4 kg (21 lb). Thus, the total cable weight is 21.5 kg (47.4 lb).

10 Wing and Pylon Design

The highly efficient wing of *Starling* was designed to match the requirements of the mission profile for both hover and forward flight. Two wings staggered in the front and rear of the aircraft provide three

major advantages: First, the wing area can be increased by a factor of two, thereby increasing the cruise lift-to-drag ratio while still remaining within the same compact space as a single wing design. Second, while in hover, two wings can provide mounting locations for the four rotors without blade overlap and additional structure. Third, the wings are located a safe distance away from the center of gravity where the passenger seating is located, allowing for ease of ingress and egress without wing height interference when boarding. During initial sizing, a wing loading of 20 lb/ft^2 and an aspect ratio of 6 were selected to meet the constraints of the 15.24×15.24 m (50×50 ft) square. However, these parameters do not account for interactions of the front wing with the rear wing. This section provides a detailed description of how the wing design was selected to overcome the complex flow and structural loads incurred throughout helicopter and airplane modes.

10.1 Wing Aerodynamic Design

To determine the specifics of the wing design for both front and rear wings, the following factors were considered: Front and rear wing vertical offset, airfoil geometry, incidence angle, sweep angle, taper ratio, and twist rate. In airplane mode cruise, the wing Reynolds number is on the order of $Re = 3 \times 10^6$ and the Mach number is $M = 0.2$.

Based on Section 3, the NACA2418 airfoil was chosen. Sizing the airfoil for the dimensional chord length, the NACA2418 is capable of fitting over 170 individual 18650 battery cells in a single open cross section as shown in Figure 10.1. This high number of cells keeps the battery pack dimensions small and allows for more flexibility with placement of cells in the wing.

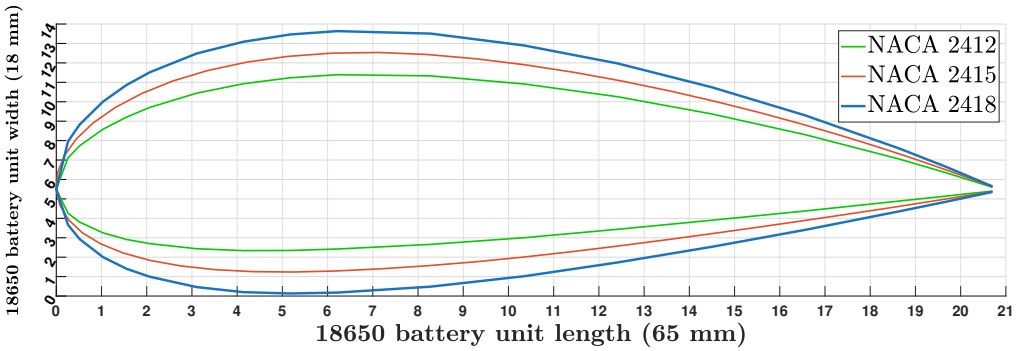

Figure 10.1: Wing airfoil coordinates plotted based on 18650 battery cell length and width

The wings were designed with no sweep for two reasons. First, *Starling* operates at low Mach numbers (M < 0.3) rendering compressibility effects negligible. Second, forward sweep in tilt-rotors is generally employed to give tip deflection clearance margins for gimballed hubs in axial flight. *Starling's* hingeless hubs reduces this requirement significantly and sufficient clearance is given with the extension of the rotor mast in the pylon. The hub plane in airplane mode is 0.46 m (1.5 ft) in front of the wing chord allowing for over 10° of flapping. The wings are untwisted to simplify the structural interface for the wing-mounted tiltrotor hubs. To reduce wing induced drag and improve the lift, a taper ratio of 0.75 was used for both front and rear wings. In order to generate equal thrust and have sufficient clearance for the rotors in hover, the rotors are spaced equally from the center of gravity. Thus, the wing location and fuselage length was largely determined by the rotor radius. In forward flight, the center of gravity shift is found to be negligible because the pylon and rotor weight shifts forward due to the change in pylon angle but the landing gear is pulled up and back. Based on an estimate of the pylon and rotor weight and landing gear weight, the incidence angle of the front and rear wing were chosen to maintain balance relative to the center of gravity, with 50% of the lift generated by the front wing and 50% by the rear.

There is limited published research on the complex aerodynamic interactions between the rotors and wings for a quad-tiltrotor configuration. Sheng and Narramore [33] investigated the Bell-Boeing quad-tiltrotor configuration and found that the downwash generated by the front wing reduced the angle of attack of the rear wing, and thus, affected the lift produced by the rear wing. Zhou et al. [34] characterized a quad-tiltrotor for trim and found the nacelle angle to have a significant effect on the interaction scheme. Thus, to generate a first order understanding of the dynamic pressure loss effect of the front wing on the rear wing, vortex lattice method (VLM) was used to generate a ratio of total wing lift between the front and rear wing as shown in Figure 10.2. At identical angles of attack and increasing vertical offset distance, the impact of the front wing on the rear wing was found to decrease. Thus, greater vertical offset distance is desired from an aerodynamic efficiency perspective. Accounting for structural and spatial constraints, a wing offset of 0.7 m (2.30 ft) was chosen.

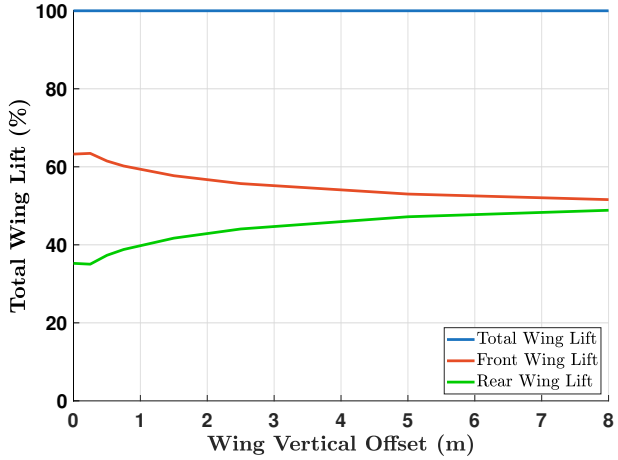

Figure 10.2: Wing lift share between front and rear versus vertical offset

A body pitch angle was selected to be 2.5° in nominal cruise based on aircraft L/D. If higher speeds are desired, this leaves some margin for the body pitch to remain $> 0°$. With a vertical offset of 0.7 m (2.30 ft) selected, the wing lift was compared for varying angles of attack accounting for the loss of dynamic pressure over the rear wing. As determined from Figure 10.3, with a body pitch angle of 2.5 deg, the front wing angle of incidence was selected to be 0° and the rear 2.5° to achieve a 50% to 50% share. In addition, the rear wing was given a positive 5° dihedral angle to improve the dihedral effect and improve stability.

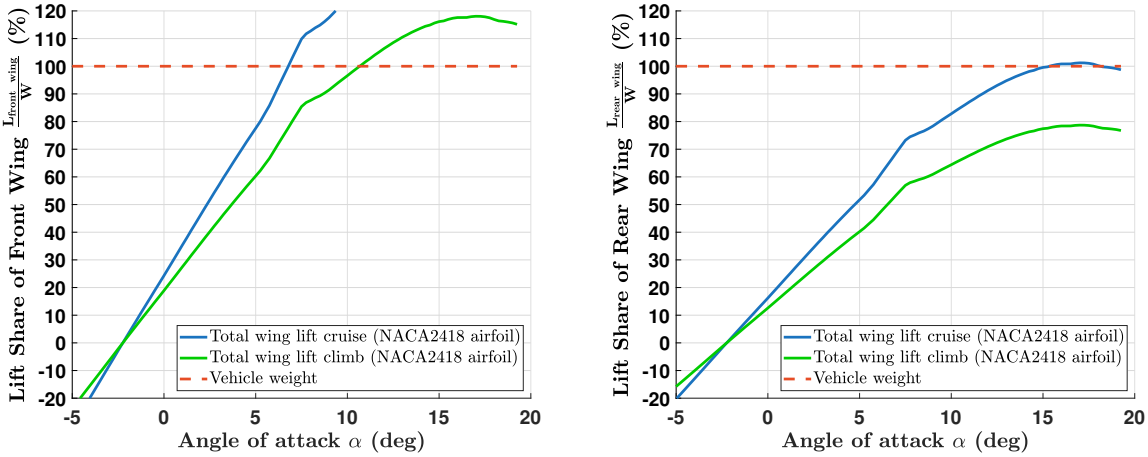

Figure 10.3: Front and rear wing percentage lift share vs. angle of attack

Table 10.1: Front and rear wing key parameters

Parameter	Front Wing	Rear Wing
Planform area	13.12 m^2 (141.2 ft^2)	13.12 m^2 (141.2 ft^2)
Root chord length	1.68 m (5.51 ft)	1.68 m (5.51 ft)
Tip chord length	1.26 m (4.13 ft)	1.26 m (4.13 ft)
Span	8.93 m (29.03 ft)	8.93 m (29.03 ft)
Angle of incidence	0°	2.5°
Taper ratio	0.75	0.75
Dihedral angle	0°	5°
$X_{\text{from C.G.}}$	2.91 m (9.55 ft)	-2.38 m (-7.81 ft)
$Y_{\text{from C.G.}}$	0 m (0 ft)	0 m (0 ft)
$Z_{\text{from C.G.}}$	0.35 m (0.82 ft)	-0.35 m (-0.82 ft)

Once the location and geometries of the wings were defined, the aerodynamic interactions between them were modeled using high-fidelity in-house 3-D RANS CFD solver. The case was setup with a mirror plane at the root of the wings in order to save computational resources. The visualization of the wake of the wings and their interactions can be seen in Figure 10.4. With strong wake interaction of the front wing on the rear, this confirmed the strong dependence of the front wing on the rear wing performance. It can be seen that the vertical separation between the wings is sufficient so that the rear wing is not directly in the wake of the front wing. The vortex lattice method analysis showed that, at their respective angles of attack, the front wing would produce 10% more lift, while CFD predicted 18% more lift produced. This 8% difference in the results can easily be accounted for using small changes in the flaps and therefore does not require changes to the design.

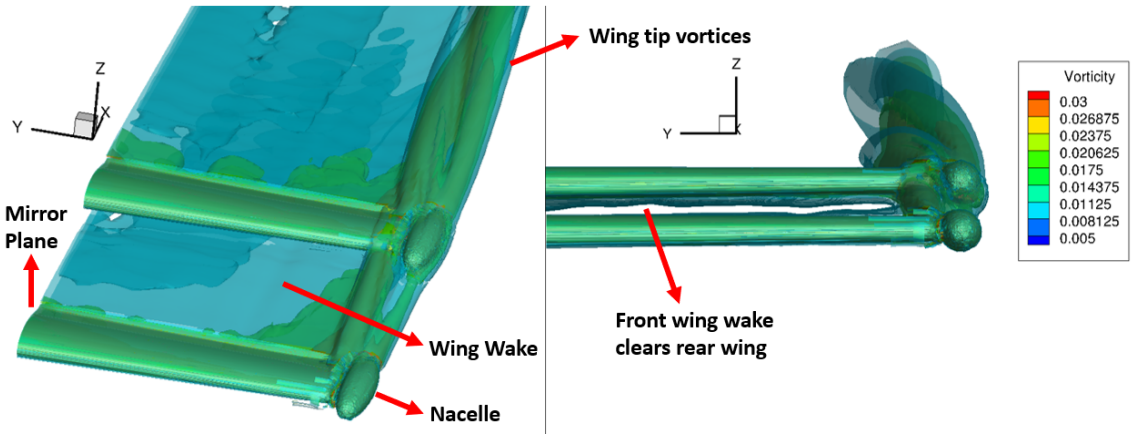

Figure 10.4: Wing and nacelle wake visualization with vorticity iso-surfaces

10.2 Wing Structural Design

The structure of the *Starling* wings is identical with the exception of the dihedral on the rear wing. The main wing spar is a single torque box running continuously between wing tips. The torque box was designed to provide the necessary bending and chordwise stiffness to delay the onset of whirl flutter as well as to support the nominal structural and aerodynamic loading, including the weight of the batteries. A closed cross section box spar is chosen to provide adequate torsional stiffness to delay air resonance. Figure 9.1 earlier showed the internal wing structure and battery placement. A portion of this battery packing overhead is earmarked for supporting structure thus the modules are themselves considered structurally

sound. They are bolted directly to the ribs.

To ensure sufficient space in the wing for placement of the batteries, a smaller spar is required. It is desirable for the batteries to be evenly distributed about the wing elastic axis to ensure less C.G. offset. Therefore, the spar is located from 0.2c to 0.5c, allowing sufficient space towards the leading edge and trailing edge for even battery distribution. This places the center of the torque box at 0.35c near the maximum thickness of the airfoil at 0.3c. With a relatively smaller spar chordwise, additional thickness is required in the top and bottom flanges to achieve adequate chordwise bending stiffness. The wing spar is composed of 26 layers of $\pm 45^{\circ}$ carbon fiber plies to achieve the desired stability margins. The motor inverters are mounted to the leading edge side of the wing spar and the pylon tilting mechanism is mounted inside at the tip.

10.3 Whirl Flutter and Air Resonance

The frequency and damping prediction of the coupled rotor/pylon/wing system was carried out with UMD's new aeromechanics solver [35, 36]. The predictions are shown with respect to airspeed in Fig. 10.5. The modes are labeled with the dominating degree of freedom. Highly damped rotor modes are not included in the figures for readability.

Wing beam (q_1) mode damping shows a peak at 148 kmph (92 mph), but then starts decreasing at higher speeds. Wing chord (q_2) mode first decreases at around 74 – 92.6 kmph (45 – 57.5 mph), after which the damping increases. At 314.8 kmph (195.6 mph), a coupled wing beam/chord mode goes unstable (damping goes negative). At the maximum cruise speed 277.8 kmph (172.6 mph), the damping is more than 3%, which is sufficient for safe flight (Boeing M222 aircraft had only 1.7% damping at 355.6 kmph (221 mph)) [37]. Note the air resonance behavior at high speeds. After 222.2 kmph (138 mph), damping of the wing torsion (p) mode decreases precipitately. This is the proprotor air resonance phenomenon that occurs due to the soft in-plane hub ($\nu_\zeta < 1$ /rev). An in-plane motion is generated at the rotor hub due to the wing torsion (p) motion and this couples with the low frequency lag ($\zeta - 1$) mode.

10.4 Pylon Structure

The pylon structure is designed to be streamlined, compact, and provide the necessary rigidity to transfer the hub forces and moments from the rotor to the wing. The structure, shown empty and assembled with components in Fig. 10.6, is constructed of six bulkheads connected radially with threaded standoffs. The first three bulkheads mount the motors in line so there is no misalignment in the connecting shafts. In between the third and fourth bulkhead is the connection to the tilting mechanism. Additional structure is added here in anticipation of the high loads transferred in hover and edgewise flight. The transmission is mounted directly to this structure and is the defining feature of the nacelle diameter. The fourth and fifth bulkheads secure the transmission to the structure and the sixth is secured to the top of the transmission housing, compressing the upper bearing housing. This housing contains two thrust bearings separated by a flange on the mast for high axial load transfer as well as a large ball bearing for radial force and moment transfer, providing an initial load path prior to the transmission. This alleviates some of the loading through the planetary gearbox reducing noise and increasing lifespan. The final bulkhead is small and positioned near the hub to mount the linear actuators for collective control. The pylon C.G. is only 56 mm (2.2 in) offset from the tilting axis of rotation. Lastly, NACA ducts are incorporated in the pylon skin to provide adequate airflow to the motors for cooling at a low drag penalty [38]. Cutouts in the rear of the pylon allow the air to exit seamlessly.

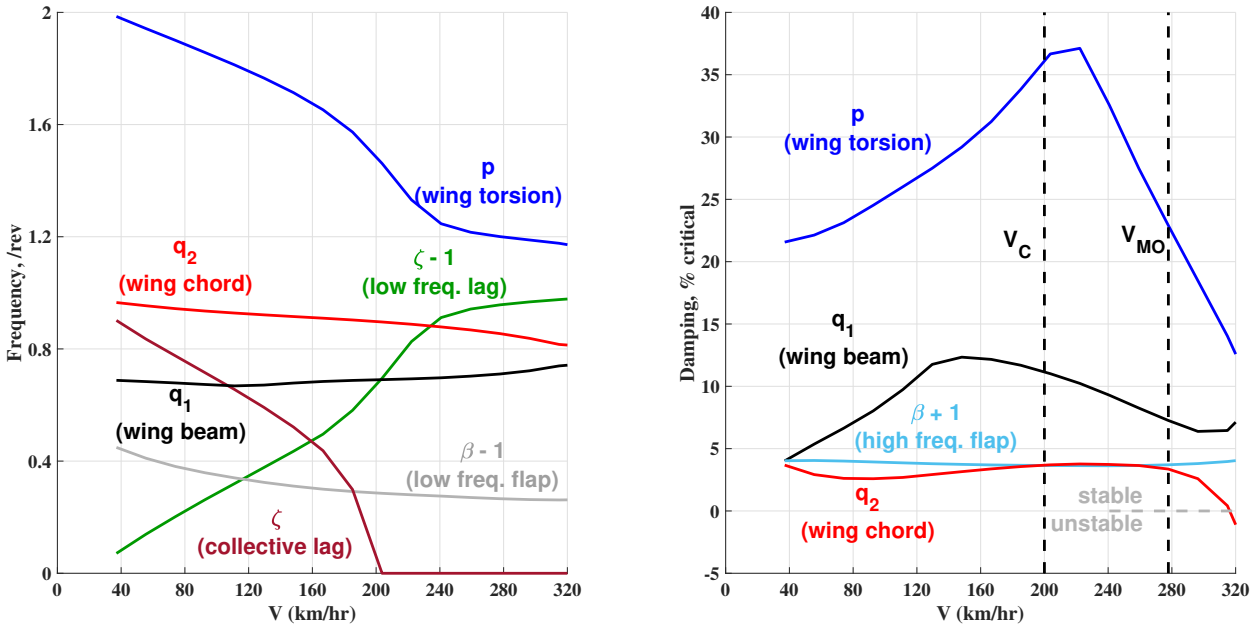

(a) Frequency (b) Damping

Figure 10.5: Wing-pylon stability roots of *Starling* at the cruise rotor speed of 225 RPM

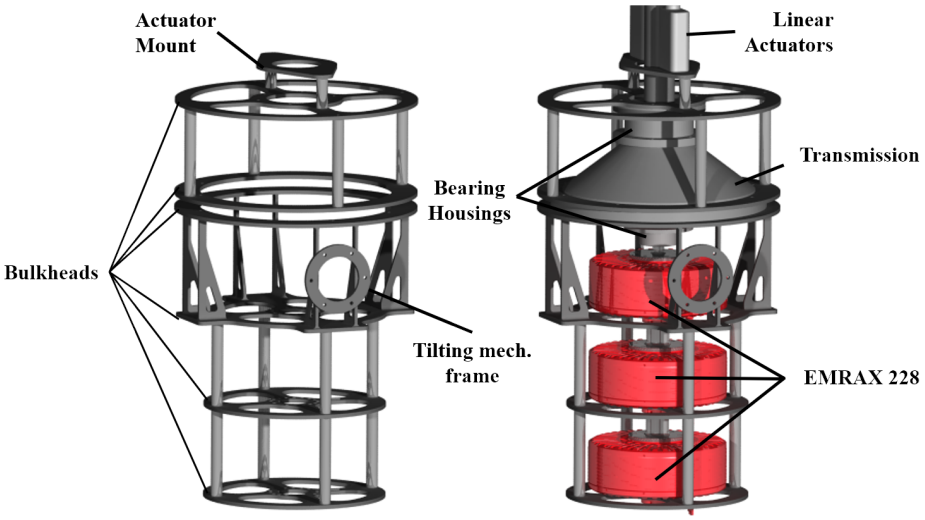

Figure 10.6: Pylon structure with and without components

The innovative tilting mechanism is a UMD modified version of Bell patented technology [39]. It is designed to be assembled from back to front within the wing tip spar as to not compromise the wing structure, shown in Fig. 10.7. The mechanism consists of Al 7075 frames that fit snugly into and are bolted to the wing spar. The torque tube is two pieced with flanged ends when bolted together, compressing two thrust bearings and allowing free rotation with axial load transfer. Teflon coated sleeve bearings are press fit into the Al frames that the torque tube passes through to provide a load path for radial loads and moments to the wing. Redundant stepper motors are installed to drive the actuator drive and spindle, pushing the pylon

down into airplane mode and pulling back up to helicopter mode. The mechanism is designed such that as the spindle rotates, the moment arm changes naturally increasing the torque at the extremes of motion. This device can be disassembled quite easily for routine maintenance and servicing.

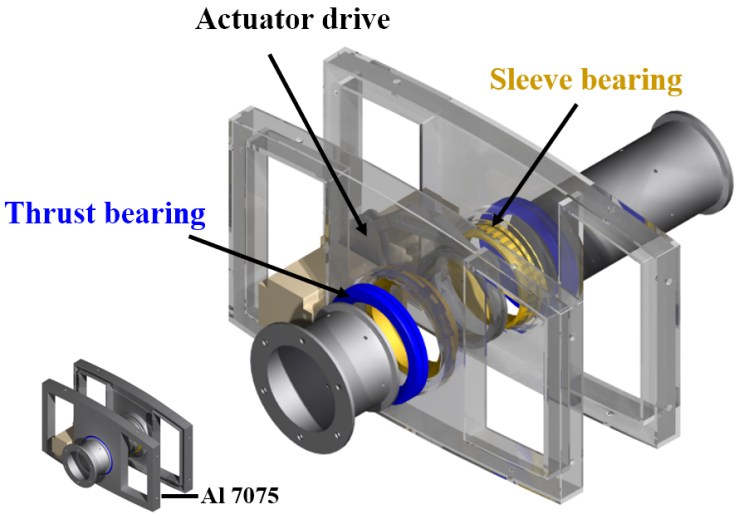

Figure 10.7: Compact wing mounted tilting mechanism

As the tilting mechanism is Bell technology, it is assumed it is capable of transitioning the XV-15 in 12 seconds. With a hover RPM of 565 it is deduced the tilting mechanism can withstand a rate of 113 revolutions. Extrapolating to *Starling* and adding 50% margin to limit blade motion, a full conversion time of 20 seconds is determined.

11 Airframe Design

11.1 Fuselage Structure

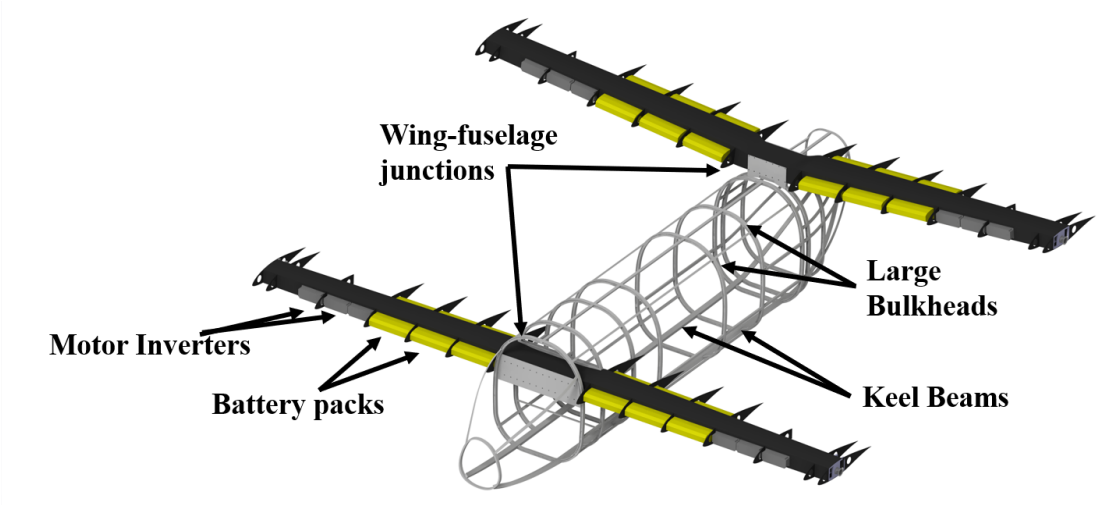

Figure 11.1: Fuselage and wing structure with batteries and motor inverters

The *Starling* airframe is a semi-monocoque structure consisting of several bulkheads, longerons and two keel beams running along the base of the airframe. There are nine large bulkheads spaced throughout the fuselage, with a smaller one in the the front and at the rear. They were spaced based on the location of important components such as the front and rear wing, the cabin space, landing gear, as well as doors and windows. The front bulkhead connects the cockpit to the rest of the fuselage, and the rear bulkhead attaches to the carbon fiber tail. Rigid attachments on the first and second primary bulkheads support the front wing's torque box. The carbon fiber wing is riveted directly to the structural attachment located on the bulkhead itself. Similarly, the rear wing is mounted to the seventh and eighth bulkheads, with the only distinction being the torque box attachment is located on top of the bulkhead as opposed to through the bulkhead, to support vertical offset between the two wings. The model of the airframe was generated using CATIA V5. The structure is designed for a limit maneuvering load factor exceeding a positive limit of 3.5 to a negative limit of -1.0. In hover, the vehicle is designed to withstand horizontal and vertical gust of 30 feet per second as defined by 14 CFR 29, paragraph §29.341. In cruise, the vehicle is designed to withstand horizontal and vertical gust loads as defined by 14 CFR 25, paragraph §25.341.

11.2 Material Selection

Alumninum-Lithium alloys are used for the construction of frames, longerons and keel beams for the fuselage structure. Al-Li alloys are preferred as they are lighter in weight compared to traditional aluminium and are simple to manufacture. Weldalite 0409 is the specific commercially available alloy used for the structural components. The cabin and cockpit floors are manufactured from kevlar and nomex honeycomb. Carbon fiber $\pm 45^{\circ}$ plies are used for the aircraft's outer skin, ingress/egress doors, landing gear doors, and exterior baggage compartments.

With the growing trend making current and future vehicles as environmentally conscious as possible, the aluminum alloys used are recyclable. *Starling*'s airframe is very environmentally friendly, as well as being lightweight, with the material choice also allowing for ease of manufacturing due to their widespread availability. Table 11.1 below compiles materials used in the vehicle.

Table 11.1: *Starling* Material Use

Materials	Usage
Al-Li Alloys	Bulkheads, Longerons, Keel Beams
Kevlar and Nomex Honeycomb	Floors, Carry-on Baggage Compartments
Fiberglass	Rotor Blade
Titanium Alloy	Nacelle Structure, Rotor Mast, Rotor Hub Yoke
Magnesium Alloy	Gearbox Housing
Oleo Pneumatic Type	Landing Gear
Copper	Cabling
Poly-carbonate	Windows
Silicon (PFDs)	Avionics
Bio-polymer foam	Seat Cushions
Epoxy	Paints

11.3 Landing Gear Design

After a study of various landing gear types discussed in Section 4, *Starling* was designed with tricycle retractable landing gear, in order to minimize the flat plate area in cruise, as well as being able to land on pre-prepared surfaces.

Wheel/Tire Sizing

Type III 5.00-4.5 tires were selected for the nose landing gear, while Type VII 16×4.4 were selected for the main landing gear. The nose tires support a maximum static load of $1.138 \times 10^7\ N/m^2$ (1650 psi), while the main gear can support a load of $2.396 \times 10^7\ N/m^2$ (3475 psi). This over-design can allow for freedom in landing orientation, as the loads the tires can carry are more than required for their relative C.G. placements. The nose tire can be inflated to a maximum internal pressure of $5.38 \times 10^5\ N/m^2$ (78 psi), and the main tires $1.276 \times 10^6\ N/m^2$ (185 psi).

Shock Absorber Sizing

Each gear is fitted with single oleo-pneumatic shock absorbers, to satisfy the landing conditions described in the RFP. Raymer [40] provides the following formula for sizing shock absorbers:

$$S = \frac{V_{\text{vertical}}^2}{2g\eta N_{\text{gear}}} \frac{\eta_{\text{T}}}{\eta} S_{\text{T}} \tag{7}$$

S is the oleo stroke, V is the descent velocity (sized using the 6.55 ft/s rate of sink speed in compliance with the RFP), η is oleo efficiency, η_T is tire efficiency, and S_T is stroke length. The results were a stroke length of 3.5 inches, which gave a full oleo strut length of 8.76 inches.

Load-Stroke

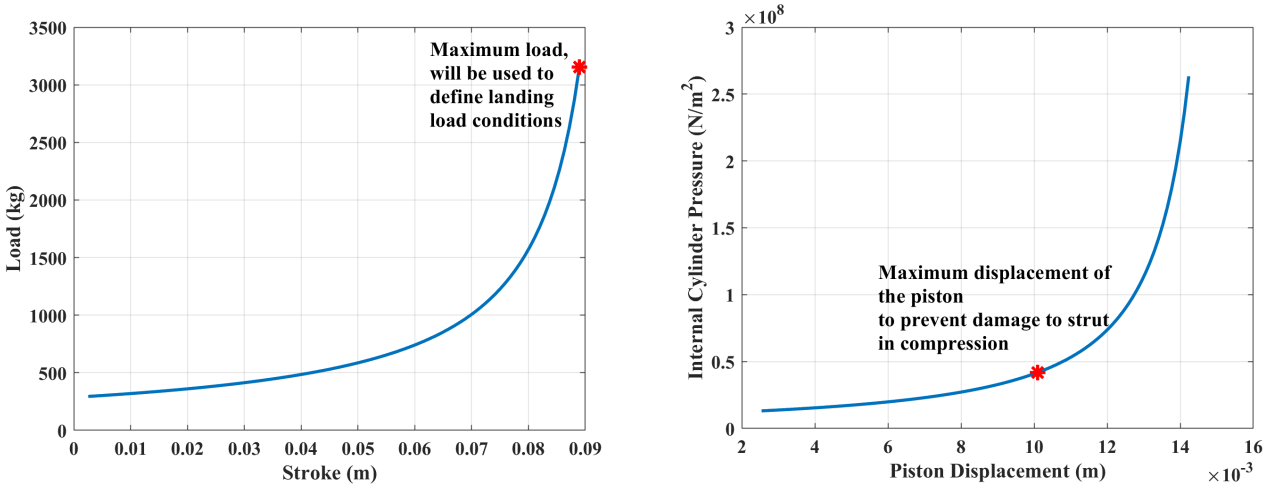

(a) Load on the oleo strut as a function of stroke length (b) Cylinder pressure as a function of piston displacement

Figure 11.2: Wing-pylon stability roots of *Starling* at the cruise rotor speed of 225 RPM

The following is the equation for the pressure during isothermal compression [41]. Converting that pressure to load will result in the relation between load and stroke length, shown above in Figure 11.2(a). The maximum load is 3152.9 kg.

$$P_x = \frac{P_1 V_1}{V_1 - xA} \qquad \text{Where } F = P_x A \tag{8}$$

P_1 is the pressure at the stroke fully extended (in N/m^2), with V_1 being the shock strut volume (in m^3) at the same location, x is the position of the piston (in m) and A the area of the piston (in m^2).

Figure 11.2(b) above shows the pressure inside the strut cylinder as a function of the displacement in the piston. The internal cylinder pressure should not exceed 4.1369×10^7 N/m^2 (6000 psi) to prevent seal leakage during compression, and through this curve the maximum piston displacement is found to be approximately 0.01 meters (0.39 inches) from the static position, where the static position of the strut is 16% of the stroke length.

11.4 Preliminary System Safety Analysis

Shear and moment diagrams for the fuselage under 7 different loading conditions are show below in the following figure, where the loading conditions are as follows: three in flight (cruise pullup and pushover, hover pullup), two gust and two landing.

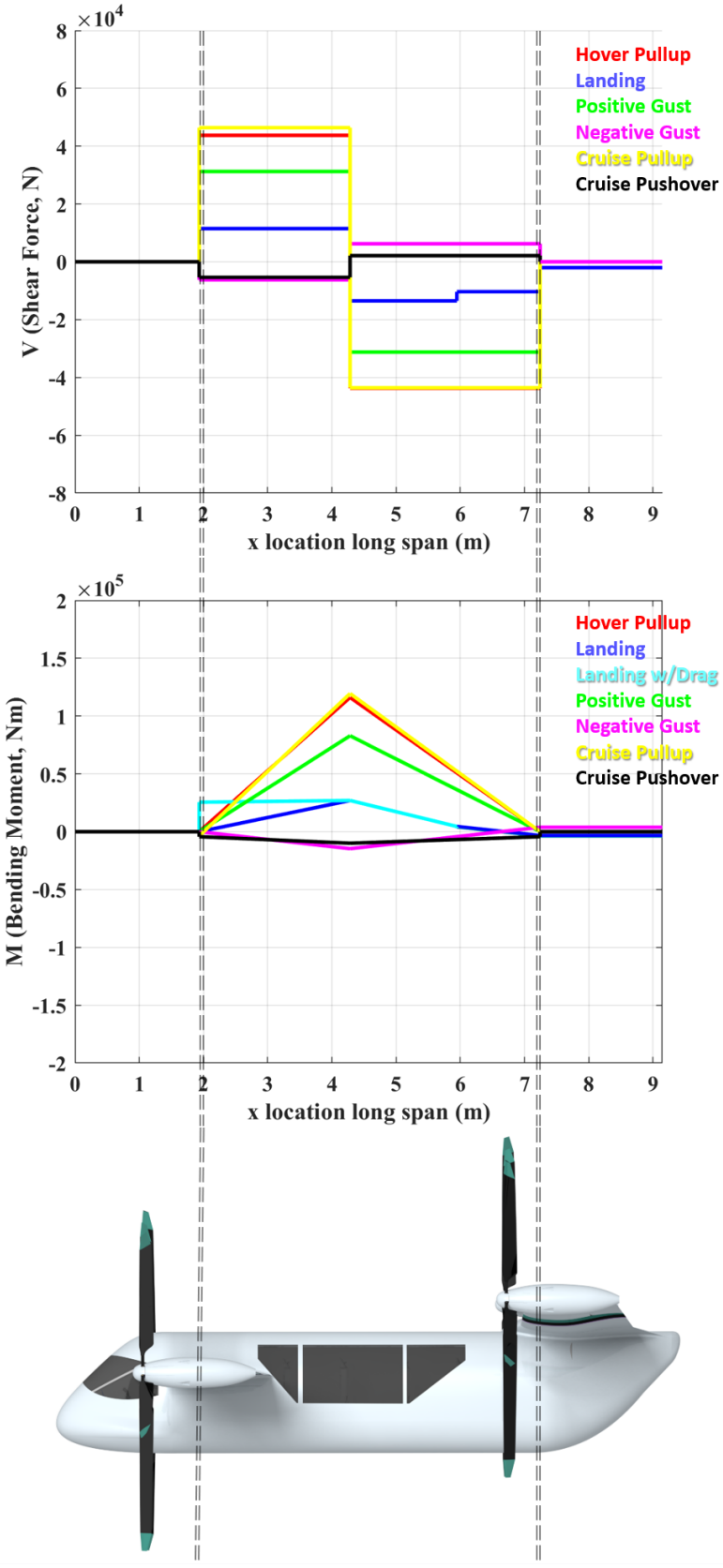

Figure 11.3: Shear and moment diagrams for fuselage under loading conditions

The shear and moment diagrams in Figure 11.3 above indicate that the highest loading occurs in the symmetrical pullup in cruise, at the area corresponding to the wing-fuselage junction. Further structural analysis was conducted in ANSYS to observe the loading on the section, shown in Figure 11.4 below.

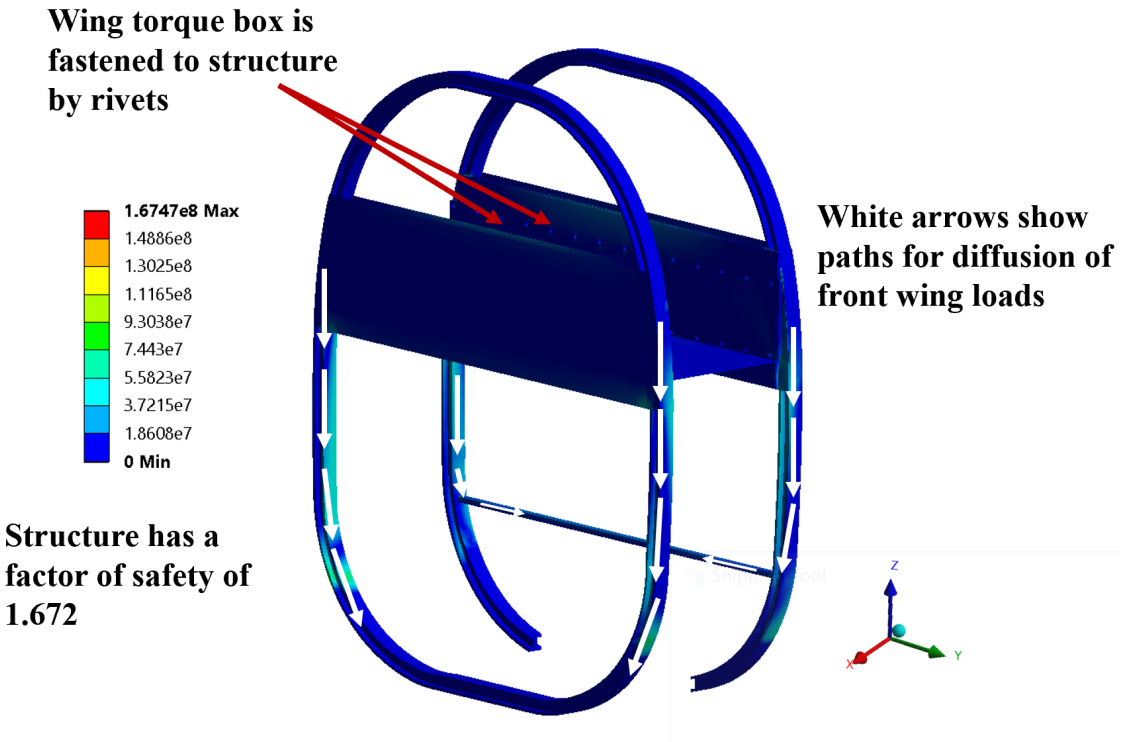

Figure 11.4: Stress analysis of wing-fuselage mounting attachment

12 Weight and Balance

The weight and balance properties of the *Starling* are tabulated in Table 12.1 and Table 12.2.

Table 12.1: *Starling* Weight Breakdown

Component Description	Weight		
	kg	lb	%
Main Rotor Group	**81.864**	**180.479**	**3.25**
Blades	64.54	142.29	2.56
Hub	14.6	32.19	0.58
Spinner	2.724	6.00	0.11
Wing Group	**238.70**	**526.25**	**9.48**
Aft Structure & Skin	83.16	183.33	3.30
Fore Structure & Skin	78.21	172.42	3.10
Flaperons	31.12	68.61	1.24
Wing Fittings	46.22	101.89	1.84
Fuselage Group	**380.53**	**838.92**	**15.10**
Bulkheads	132.08	291.19	5.24
Longerons & Keel Beams	248.45	547.74	9.86
Skin	26.97	59.45	1.07
Nacelle Group	**25.33**	**55.83**	**1.01**
Motor Group	**144**	**317.47**	**5.72**
Drive System Group	**55.92**	**123.28**	**2.22**
Gearbox	36.94	81.43	1.46
Drive Shafts	7.736	17.05	0.31
Rotor Shaft	11.25	24.80	0.45
Power Distribution Group	**581.95**	**282.99**	**24.0**
Battery Weight	478.8	1055.57	19.0
Inverters	90	198.41	3.57
Cabling	21.5	47.4	0.85
Buses	13.15	29.0	. 0.52
Cabin Group	**248.3**	**547.4**	**9.86**
Accessories Group	**66.74**	**147.143**	**2.65**
Cockpit Controls	4.56	10.06	0.18
Avionics & Instruments	62.18	137.08	2.47
Payload Group	**589.67**	**1300**	**23.41**
Maximum Take-Off Weight	**2518.79**	**5552.97**	**100**

Table 12.2: *Starling* Center of Gravity from nose tip and Moment of Inertia's about the C.G.

Config.	Gross Weight [kg]	Center of Gravity [mm]			Mass Moment of Inertia [kg - m^2]					
		x	y	z	I_{xx}	I_{yy}	I_{zz}	I_{xy}	I_{xz}	I_{yz}
Hover	2497.3	4564.3	77.5	1163.5	16042.4	12487.1	26596	-528.2	1666.6	41.1
Cruise	2497.3	4565.3	77.5	1153.5	16193.6	12585.6	26570	-533.1	1748.9	40.1

13 Flight Dynamics and Controls

The unique quad-tiltrotor bi-plane design incorporates a number of stability and controllability features found on other representative aircraft. The Unified Pilot Flight Control framework creates an intuitive pilot experience, reducing pilot workload by maintaining similar functionality throughout all flight modes. An explicit model-following control system was chosen to ensure vehicle responses match closely with commanded pilot inputs. These control features are implemented using a fly-by-wire architecture, further reducing pilot workload and ensuring safe, reliable flight.

13.1 Pilot Command-to-Target Mapping and Modes

The unified pilot flight control methodology was designed to make flying the aircraft intuitive and easy, thereby reducing pilot error. First developed in 1980 and used on the Lockheed Martin F-35 aircraft, unified flight controls are becoming the gold standard for eVTOL vehicles [42]. Unlike a conventional helicopter's collective, cyclic, and pedals, there is one directional controller on the right of the pilot and one inceptor, or collective, on the left. The right hand directional controller controls altitude, attitude, and direction while the left hand inceptor controls longitudinal acceleration. Yaw control is performed by twisting the directional control in the desired yaw direction, instead of pressing foot pedals like in traditional rotorcraft. The unified control mapping and explicit model following framework (see Section 13.4) automatically manage the controls to a desired state, removing the need for the pilot to perform stabilizing control inputs and allowing the pilot to focus solely on commanding the vehicle for the current mission. This architecture significantly reduces pilot workload and decreases the potential for pilot-induced errors. In addition, this control scheme allows the aircraft to be controlled based on costs such as performance, acoustics, and desired agility. The pilot control sticks and layout are shown in Figure 13.1 and Figure 13.2.

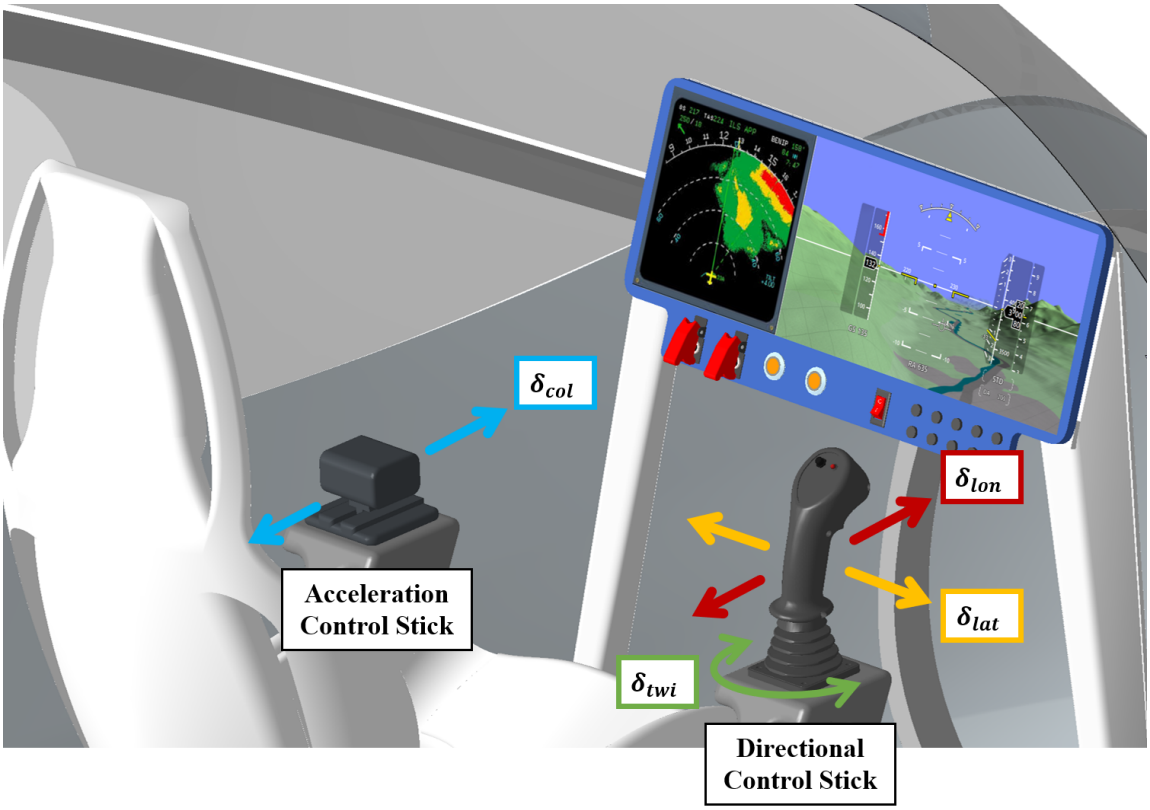

Figure 13.1: Pilot left and right hand inceptor controls

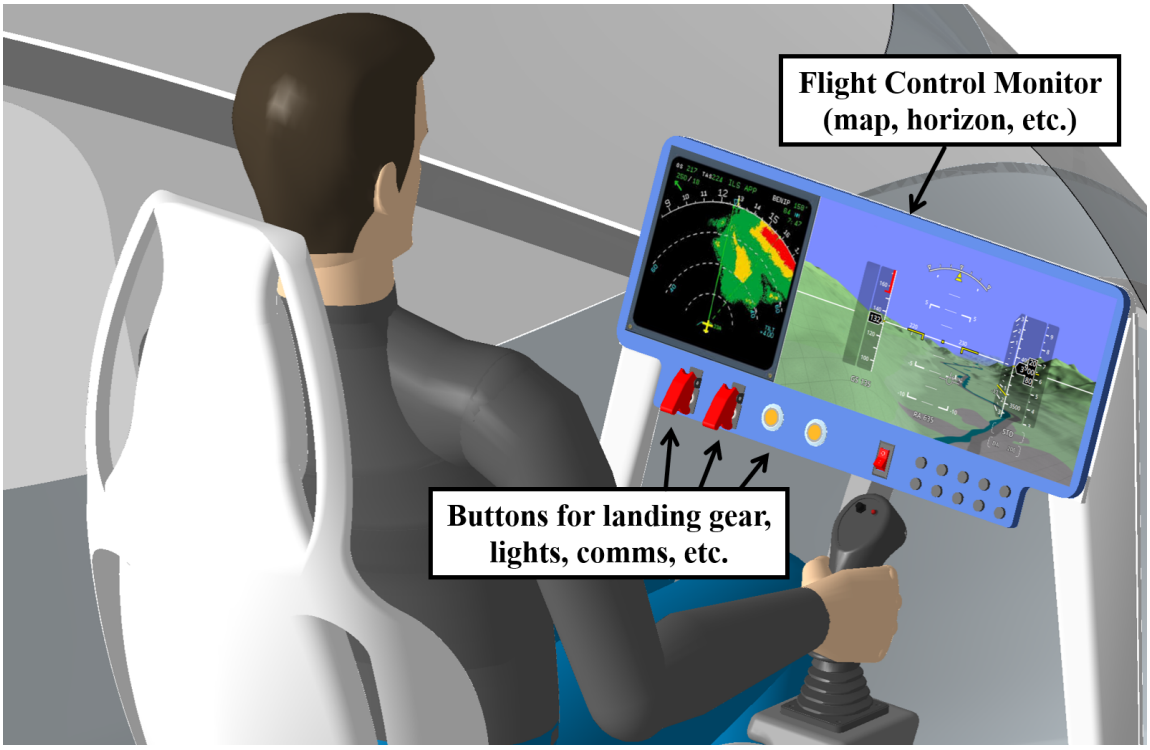

Figure 13.2: Cockpit interior with monitor and flight control interface

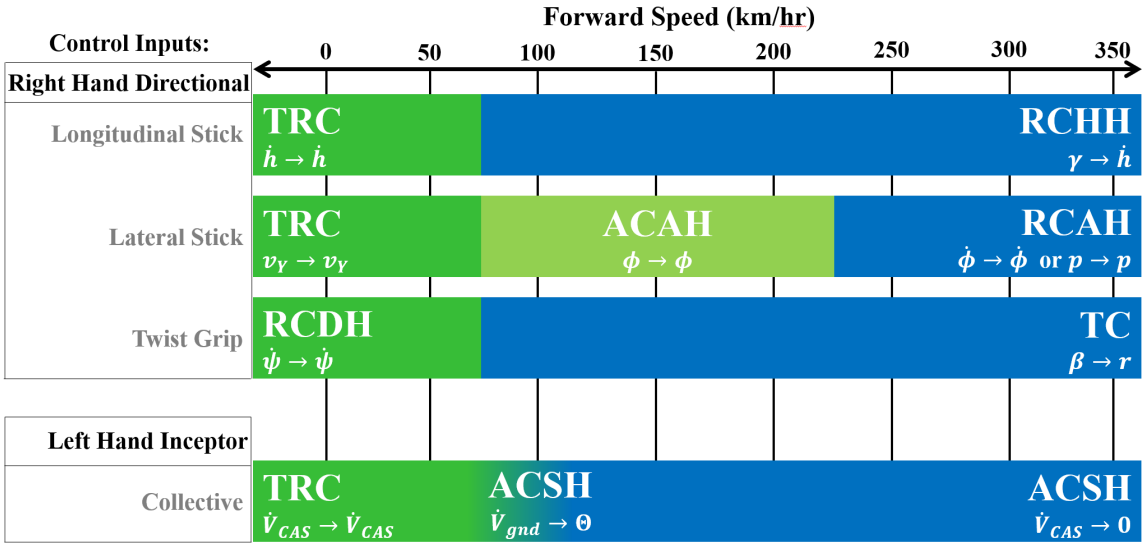

Figure 13.3: Modes and mapping of unified controller commands to target

The modes in flight for the unified controller are speed-dependent, shown in Figure 13.3. The flight modes and mapping from commands to targets are shown for the unified controller in Table 13.1 [43].

For the unified flight control method in hover, longitudinal and lateral stick commands are governed by Translation Rate Control (TRC) mode [43]. Left- and right- directional control stick movements δ_{lat} control the horizontal-lateral speed components v_Y. The twist grip δ_{twi} controls the turn rate $\dot{\phi}$ and is governed by Rate Command Direction Hold (RCDH) mode. Forward and back longitudinal stick inputs δ_{lon} control vertical speed $\dot{h}$ and is also governed by TRC mode. Collective control inputs δ_{col} change longitudinal velocity $\dot{u}_X$. With sustained collective input δ_{col}, the vehicle will transition to forward flight where δ_{col}

Table 13.1: Unified flight controlled variables per flight mode and per axis

Mode	δ_{lon}	δ_{lat}	δ_{twi}	δ_{col}
hover	$\dot{h}$	v_Y	$\dot{\psi}$	$\dot{u}_X$
transition	ϕ	ϕ	β	$\dot{V}_{\text{gnd}}$
forward flight	ϕ	$\dot{\phi}$	β	$\dot{V}_{\text{CAS}}$

controls ground speed $\dot{V}_{\text{gnd}}$ and is governed by Acceleration Command Speed Hold (ACSH) mode. Once in forward flight, δ_{col} controls calibrated airspeed $\dot{V}_{\text{CAS}}$ again in ACSH mode. For directional control in transition and forward flight, left and right directional stick movements δ_{lat} control the bank angle ϕ in transition or roll rate $\dot{\phi}$ in forward flight. Lateral stick inputs are controlled by Attitude Command Attitude Hold (ACAH) mode in transition and then Rate Command Attitude Hold (RCAH) mode in forward flight. Forward and back inputs δ_{lon} affect the flight path angle γ. These longitudinal stick inputs are governed by Rate Command Height Hold (RCHH) mode while in forward flight.

The Unified flight controller is less simplified than other control schemes such as the EZ-Fly approach but more flight physics-based, which makes it more familiar to existing pilots. Furthermore, pilot training curriculum already exist due to the control methods used on existing aircraft like the F-35B Lightning II and can be readily adapted for eVTOL pilot instruction.

13.2 Control Mixing

After the pilot commands a desired vehicle response through the unified flight control inceptors, the *Starling* must behave similar to a helicopter when in hover, similar to an airplane when in forward flight, and it must navigate the transition between flight modes safely throughout conversion. Each of the *Starling*'s soft in-plane hingeless prop rotors are independently controlled using collective blade pitch, and the front and rear wings include plain flap flaperons for control in forward flight. Continuous control mixing is conducted by the Primary Flight Control System (PFCS) using a fly-by-wire architecture (see Section 13.5) to ensure the vehicle responds correctly to pilot inputs, while maintaining stability and remaining within safe operating limits.

In helicopter mode, thrust/power control is accomplished through uniform collective pitch on all four prop rotors. Differential collective pitch on fore and aft prop rotor pairs is used to regulate aircraft pitch, while aircraft roll is controlled through differential collective pitch on right and left prop rotor pairs. Although differential collective control on tiltrotor aircraft has previously been linked to pilot induced oscillations and sluggish response [44], the fly-by-wire control architecture incorporating unified mapping and explicit model following strategies can be tailored to mediate these negative response characteristics. Aircraft yaw is accomplished by differential torque/power on clockwise and counter-clockwise prop rotor pairs. The control actions of the *Starling* in helicopter mode can be seen in Figure 13.4

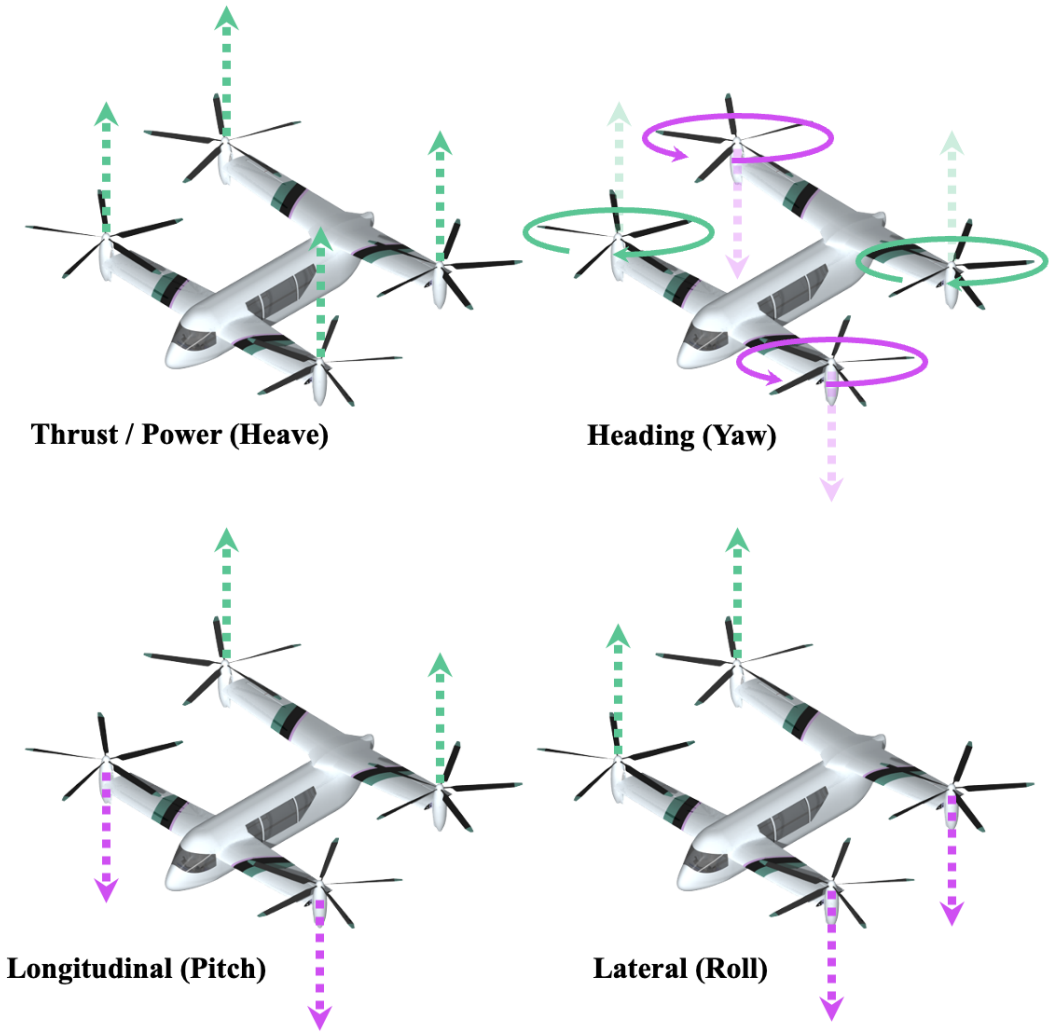

Figure 13.4: Control Mixing Strategy in Hover

In airplane mode, matched and opposing deflections of flaperons induce pitching and rolling moments about the aircraft center of gravity, similar to a traditional fixed-wing aircraft's aileron and elevator control surfaces. Yawing moments can be generated using differential collective on right and left prop rotor pairs in axial flight. However, heading change for fixed wing aircraft is primarily accomplished through rolling motion using deflections of the flaperons[13]. The *Starling*'s rear wings also feature a 5° dihedral, slightly tilting the lift forces of the rear wings towards the fuselage center line. As opposing deflections of the rear flaperons increase/decrease the lift force of the rear wings, the resultant force has a small lateral component which can be used for correcting sideslip angle and for heading trim. The utility of the rear dihedral wing and flaperons is demonstrated in Figure 13.5 (deflections and resulting lift changes are exaggerated for clarity). This method will also generate a rolling moment, which can be easily controlled by generating a restoring/stabilizing rolling moment with the front flaperons. The dihedral rear wing also improves the roll stability of the vehicle, discussed further in Section 13.3.2.

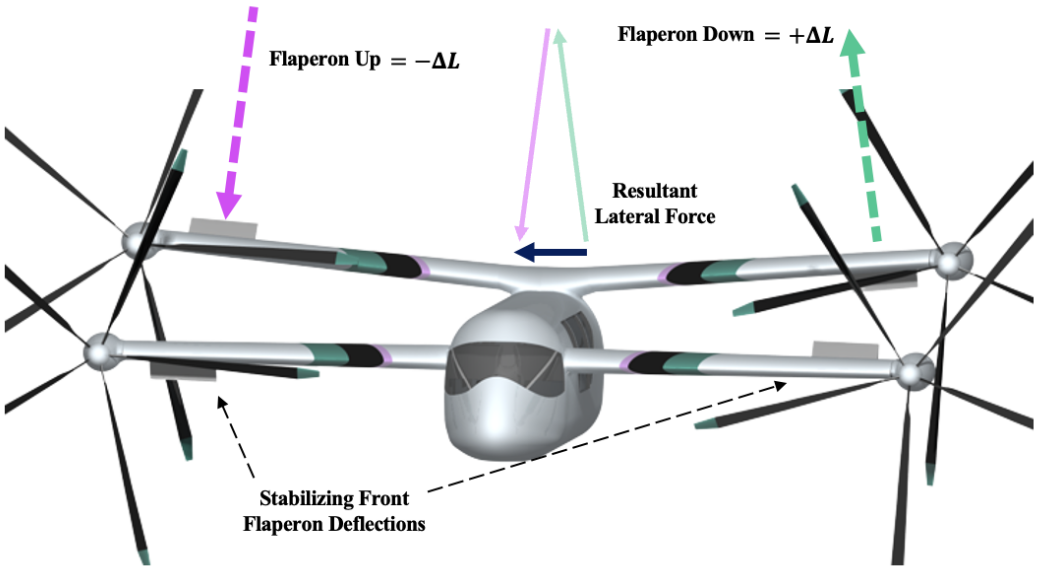

Figure 13.5: Sideslip Mediation and Heading Trim with Rear Flaperons

13.3 Flight Dynamics & Stability

While detailed, non-linear modeling of a vehicle's flight dynamics are required to fully capture the dynamic response of rotorcraft, linear models of rigid body dynamics about trimmed flight conditions can be insightful into the open loop stability of the aircraft. These equations take the form shown in Equation 9, where the states of the rigid body dynamics are $\mathbf{x} = (\, u \; v \; w \; p \; q \; r \; \phi \; \theta \; \psi \,)$, the $\mathbf{A}$ and $\mathbf{B}$ matrices contain the stability and control derivatives, and the prop rotor collectives and flaperon deflections are contained in the input vector $\mathbf{u} = (\, \theta_{75_1} \; \theta_{75_2} \; \theta_{75_3} \; \theta_{75_4} \; \delta_{f_1} \; \delta_{f_2} \; \delta_{f_3} \; \delta_{f_4} \,)$.

$$\dot{\mathbf{x}} = \mathbf{A}\mathbf{x} + \mathbf{B}\mathbf{u} \tag{9}$$

13.3.1 Stability in Helicopter Mode

The *Starling* features two clockwise rotating prop rotors (front left and rear right) and two counter-clockwise rotating prop rotors (front right and rear left). This rotor configuration creates natural anti-torque in steady state flight conditions, removing the need for a tail rotor or other dedicated anti-torque system. Rotorcraft are inherently unstable in hover due to the influence of high order rotor dynamics. With four prop rotors controlling the *Starling* in helicopter mode, unstable modes in the vehicle dynamics are expected. A linear state-space model was developed for the *Starling* in hover (helicopter mode) using an in-house aeromechanics solver, and the resulting hover modes are shown in Figure 13.6 [24]. The open loop modes of the XV-15 experimental tiltrotor are also shown [45]. As expected, the *Starling* is open-loop unstable due to a phugoid pair in the right half of the complex plane. This unstable mode can be easily controlled using the fly-by-wire flight control system (see Section 13.5) and sufficient feedback compensation can ensure that the phugoid pair becomes a stable mode in the closed loop vehicle dynamics.

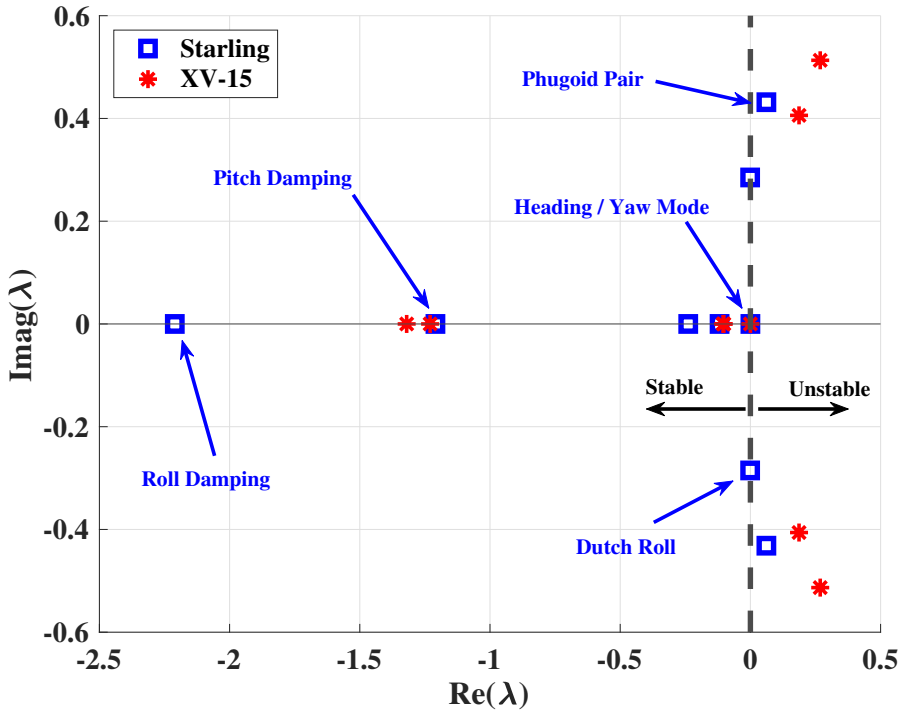

Figure 13.6: The *Starling* Compared to XV-15 Hover Modes

13.3.2 Stability in Airplane Mode

A unique design feature of the *Starling* is the lack of a vertical stabilizer at the tail of the aircraft. Traditional fixed wing aircraft use a vertical stabilizer and rudder to provide lateral stability, prevent sideslip angle, and for fine heading changes. Instead of a vertical and horizontal tail, the *Starling*'s rear wing is at a 5° dihedral to provide these necessary stability functions. This dihedral provides natural lateral and roll stability to the aircraft due to the dihedral effect, where the rear wing generates a restoring rolling moment in the event of sideslip angle, rotating the aircraft back to level flight[13]. This dihedral effect also acts to decrease the severity of spiral and dutch role modes of the *Starling*'s airplane mode flight dynamics[13]. In addition to the dihedral angle, the rear wing is staggered, mounted 0.7 meters higher on the fuselage than the front wing. This ensures that the trailing wake from the front wing does not impinge on the clean airflow over the rear wing, allowing for efficient lift generation on both lifting surfaces. The combination of wing stagger and rear wing dihedral also raises the rear prop rotors (located on the rear wingtips) above the front prop rotors when in the pylon-down configuration. This works to move the rear prop rotors slightly out of the downwash of the front prop rotors. The chosen rotation directions of the four prop rotors, in addition to providing the necessary anti-torque, also works to cancel the wing tip vortices which form on the fore wing. The prop rotor on the front right wing rotates counter-clockwise and the prop rotor on the front left wing rotates clockwise, whereas the vortices at the wing tips curl in the opposing direction. Because both the fore and aft wings generate upward pointing lift forces in level flight, this has the tendency to destabilize the vehicle in pitch [13]. However, with a well designed fly-by-wire control architecture (see Section 13.5) it is believed that this phenomenon can be stabilized using calculated flaperon deflections.

13.4 Control Law Development

The *Starling* eVTOL employs an explicit model following architecture as depicted in Fig. 13.7. As described in Section 13.1, the pilot directs the aircraft to a desired vehicle state using unified control inceptors in the cockpit. The desired dynamic response to reach the commanded vehicle state is specified within the Command Model. Any preferred dynamic response can be specified in the Command Model, and different Command Models can be used in different flight conditions or for multi-mission capability. The feedforward portion of this flight control framework performs a cancellation of the *Starling*'s bare-airframe dynamics using an inverse plant model [11][46]. Ideally, this inverse model should perfectly cancel all modes in the aircraft's plant dynamics, such that the vehicle will explicitly track the response that is defined in the Command Model. However, this is often not feasible, as higher order dynamics contained in aircraft subsystems (rotors, actuators, aeroelasticity, etc.) are difficult to capture in the inverse plant model [46]. Therefore, additional feedback compensation sufficiently stabilizes the dynamics and rejects disturbances. Multiple methods for feedback stabilization are possible within the compensation element of this control framework. Independent design of the Command Model response and feedback stability characteristics provides for a robust, consistent, and predictable vehicle response through all flight conditions and external disturbances.

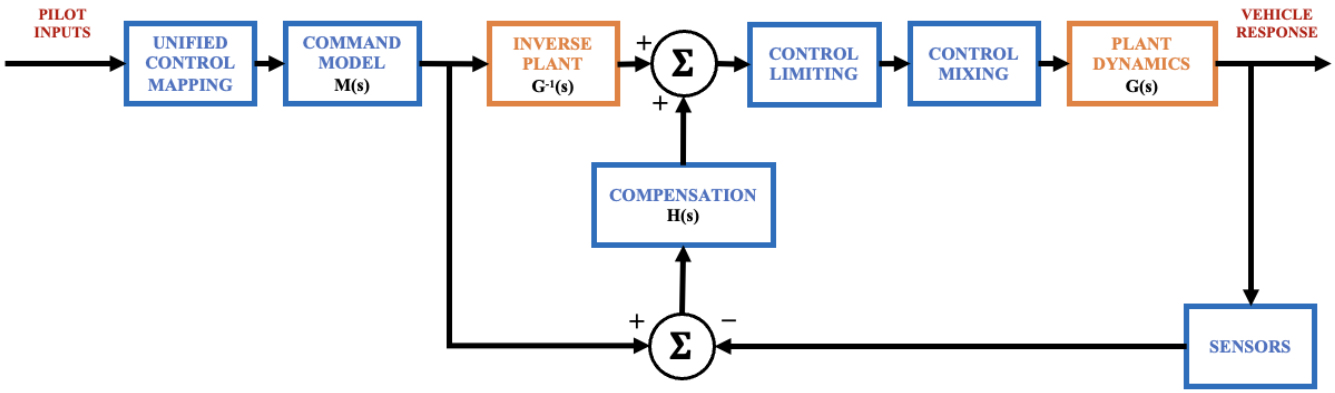

Figure 13.7: Explicit Model Following Control Law

13.5 Fly-by-Wire Architecture

Figure 13.8 shows a schematic for the *Starling*'s digital fly-by-wire (FBW) architecture. The system is designed to minimize pilot workload and maximize reliability. The digital framework combines information from vehicle sensors, redundant flight computers, and pilot inputs to carry out necessary control actuator inputs for desired vehicle dynamic response and to maintain safe flight operation.

The Flight Control Computer (FCC) forms the central feature of the FBW architecture, containing two independent Primary Flight Control Processors (PFCP) which perform identical and concurrent, in-line computations. The Input-Output Processor (IOP) passes the resulting signals to corresponding control actuators and passes feedback into the PFCPs. Signals from the independent PFCPs are compared to ensure agreement, and an appropriate shut down operation is executed in the event that the signals disagree. A separate Automatic Flight Control Processor (AFCP) handles all computations tied to the Automatic Flight Control System (AFCS). By partitioning the PFCPs and AFCP from each other, additional redundancy is built into the FBW system.

The Air Data Computer (ADC) interprets information from an Attitude and Heading Reference System (AHRS), developing aircraft state estimations from IMU, GPS, pitot-static probes, and other navigational equipment measurements. The Flight Management Computer (FMC) conducts path planning and waypoint navigation using commands from the Flight Director (FD). Both are informed by ADC signals and direct sensor measurements in order to provide the AFCS with mission critical planning information, directing the aircraft through various flight modes and operating states.

Additional sensors located within flight critical subsystems send data to Health and Usage Monitoring Systems (HUMS) (see Section 14.9), continuously monitoring the condition of these systems and communicating their health status to the ADC. The ADC links the HUMS with the main FCC, which uses limiting functions to prevent the vehicle from operating outside the bounds of safe system operation. Pilot commands which would push the vehicle or subsystems into unsafe operating conditions are prevented by further control limiting withing PFCS control laws.

In comparison to a conventional flight control system, the digital FBW architecture presented here holds many advantages. This digital system presents weight savings, as there are no mechanical linkages connecting pilot inceptors to control actuators. The digital system is also better equipped for vehicles such as the *Starling* with complex flight dynamics and varying flight modes, as the software and control laws can be formulated to easily change gains and mixing laws during conversion between a large range of flight conditions. Modifications and tuning of the responsiveness of the system is also simpler with a FBW system versus a mechanically linked control system, and higher levels of tolerance and accuracy can be achieved.

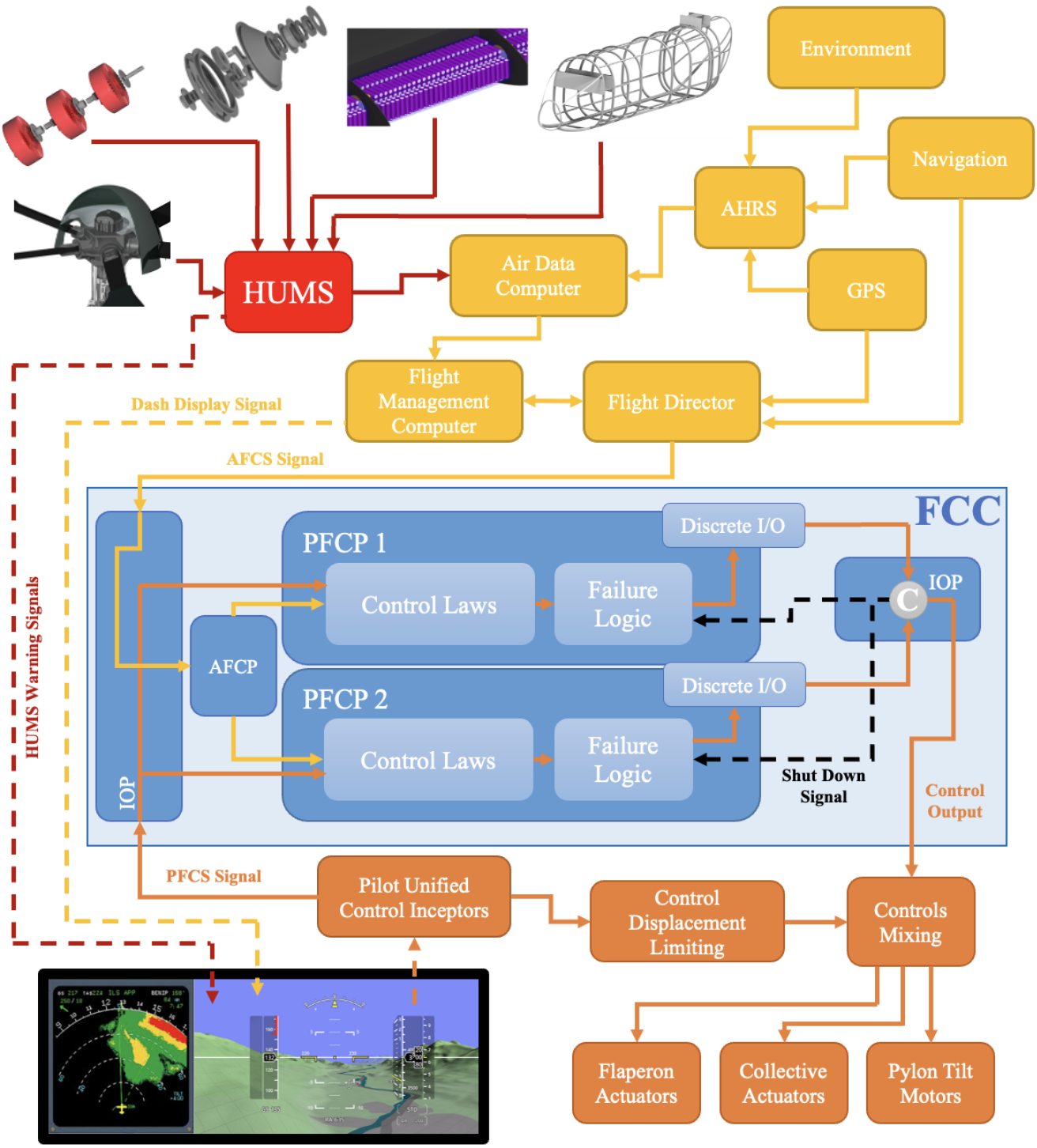

Figure 13.8: Fly-by-Wire Architecture

14 Avionics System

Starling is designed to safely transport passengers between urban hubs, airports, as well as suburban locales. Each location offers its own set of flight challenges, from unique urban gust fields to crowded commercial

air space. Since the entire mission is accomplished by a single pilot, reducing the pilot workload is critical to ensuring mission success. eVTOL aircraft such as *Starling* will not be integrated into the urban airspace unless all risks and dangers can be predicted, controlled, and regulated. Thus, it is critical to have modern Advanced Air Mobility (AAM) avionics that can navigate and operate in congested skies.

14.1 Automatic Flight Control System

Starling is designed to precisely operate in gusty wind conditions and in complex urban environments. An automatic flight control system paired with a unified pilot control system described in Section 13 can significantly reduce workload and keep the pilot focused on accomplishing the mission safely. *Starling* is equipped with a triple-redundant Stability Augmentation System (SAS) and four-axis Automatic Flight Control System (AFCS). A Flight Director and a Flight Management System (FMS) are also equipped to reduce pilot workload. AFCS has authority over all axes including roll, pitch, and yaw in hover and forward flight. This enables the use of TRC, RCDH, ACAH, RCHH, RCAH and TC modes described in Section 13. In addition, the vehicle can be brought to an automated and stabilized hover that maintains position relative to the ground or relative to altitude. This is accomplished using triple redundant electrically heated pitot-static tubes, inertial measurement units (IMU), a GPS, and a radar altimeter. In the event of loss of datalinks or blackout, the aircraft can continue to be safely flown by the pilot visual line of sight. Although the pilot is in full control of the aircraft, autopilot can be used to further reduce pilot workload by controlling the aircraft flight path automatically.

14.2 Vision-Based Autonomous Landing System

Since *Starling* operates in an urban environment, it requires a special landing system. Traditional systems based on GPS, ILS or MLS will not work for the aircraft as they are heavy and designed only for environments around airports with large open airspace. *Starling* might need to actively detect and avoid obstacles while landing. Thus a vision based landing system is used. This is a special requirement of eVTOL aircraft.

The vision system of *Starling* consists of a set of 12 cameras for creating a complete 3D map of its surroundings and the terrain. There are 2 cameras on each side of the aircraft and 4 on the bottom. Each camera based on Sony IMX490 automotive image sensor has 120 degrees field of view and 120 dB dynamic range to avoid motion artifacts. The side cameras are angled to have 30 degrees field of view above horizon and provide stereo-vision capabilities. The 4 cameras on the bottom provide double redundant stereo-vision for landing and can tolerate failure of 2 of them. The cameras help to create a 3D map of objects around the aircraft up to a range of 150 m (492 ft) using a feature based vision algorithm [47]. The algorithm will include corrections for partial occlusion and degraded vision scenarios such as fog, smoke, bright glare, rain, reflection or lack of illumination. Next, using the generated 3D map, a path planner based on optimal control then calculates a trajectory for the aircraft to follow, while avoiding all the obstacles around the landing pad and respecting aircraft dynamics, power and actuator constraints. In piloting mode, this trajectory works as a suggested route for the pilot to follow and is constantly updated every second based on the aircraft current state. The generated 3D map also helps to make the pilot aware of all the obstacles around the aircraft while landing and warns the pilot of potential collisions. The cameras on *Starling* are capable of sensing near-Infrared electromagnetic spectrum and hence can work even in low-light night operations. It should be noted that although the aircraft is designed to be operated by a single pilot, the vision landing system is capable of autonomously steering the aircraft to a safe landing spot in case of emergencies. This is done by mapping the terrain with its cameras, finding a safe landing spot on the terrain based on obstacles and terrain elevation and then using the optimal control based path planned to generate and execute control inputs for safe navigation to the spot.

14.3 Communications System

Communication with Air Traffic Control (ATC) and other aircraft operating in a populated airspace is critical to the success of the mission. The communications module consists of standard equipment such as antennas, receivers, and transmitters that include FM, HF, UHF, and VHF. The pilot will also need to be in constant communication with the passengers and ground support crews at the arrival and departure airports. Thus, the cabin is equipped with speakers and screens to not only communicate with non-disabled passengers, but also visually impaired and deaf passengers.

14.4 Air Conditioning and Heating System

An air conditioning and heating (AC/Heating) system can be included if desired by the purchaser. As shown later in Table 14.1, the addition of an AC/Heating system significantly increases weight and power consumption, reducing the achievable mission range. The *Starling* operates in short-range trips at relatively low altitude, therefore significant variations in ambient temperature are not expected. It is recognized that patients with nerve-related disabilities and damage like multiple sclerosis could have their nervous system functionalities compromised with exposure to extreme temperatures [48], therefore an AC system can be added at the expense of either maximum payload capability or maximum achievable range.

14.5 Landing Gear

The retractable tricycle landing gear includes an electric parking brake and actuation system. The deployment of the landing gear is operated by a switch in the cockpit with a position reading. In the event that the landing gear fails to extend, an alarm sounds notifying the pilot.

14.6 Lights

Light are installed both inside the cabin and on the outside of the aircraft. Besides general cabin lighting, a Helicopter Emergency Lighting System (HEELS) is used to safely guide passengers to the nearest exit in an emergency. Lights are also used on the outside of the aircraft for position and anti-collision which are critical for nighttime flights in densely populated areas with other air traffic.

14.7 Battery Management System

A Battery Management System (BMS) is used to provide protection for over-voltage/low-voltage, over-current, and short circuit. The BMS also balances the module voltages during charge and discharge as well as reports operational status to the pilot. This data is used to track power draw from the battery packs to calculate estimated range and endurance remaining in the pack for the mission based on the present flight conditions such as wind and air density.

14.8 Cyber Security

As a fly-by-wire vehicle, *Starling* requires modern cybersecurity tools to ensure flight safety. Avionics suites in legacy commercial aircraft are highly susceptible to wireless attacks to the unencrypted ADS-B system and GPS jamming and spoofing. Compromises to both directly affect critical portions of the AFCS such as the flight management system, which uses GPS as an input for flight-plan following [49]. Other potential cyberattacks include SCADA (Supervisory Control and Data Acquisition) threats, GPS/LIDAR spoofing, EM interference, Vehicular or Flying Ad-Hoc Networks (VANETs/FANETs) compromises, and acoustics/sonic

[50]. These attacks can create critical problems for safety and operations. *Starling* communication tools come with 128-bit Advanced Encryption Standard (AES) to secure non-GPS communications.

14.9 Health and Usage Monitoring Systems (HUMS)

To ensure systems are operating as they should, Health and Usage Monitoring Systems (HUMS) are used to provide data on flight critical systems. With the complex operating conditions of the aircraft and priority for safety, it is critical to monitor the performance, critical loads, and identify problems early on.

Three distinct processes of the maintenance schedule for eVTOL include:

- **Hard-time:** Preventive maintenance and checks are done at fixed intervals of time.
- **On-condition:** A less rigorous maintenance check of critical components is performed. Suspect components will be inspected and replaced if needed.
- **Condition monitoring:** A non-preventative process where data from all components and systems are monitored and corrective measures are applied where necessary.

Starling is equipped with both on-line and off-line HUMS. For on-line HUMS, the system monitors critical systems such as transient rotor shaft torque, battery cell voltage, and motor heat. The DC-DC converter which produces the FAA-certified 24 V required current and voltage is also measured to ensure auxilary components are not drawing more power than expected. These are monitored in flight and will alert the pilot if sensors detect anomalies. Off-line capabilities include monitoring components as they relate to fatigue life to determine future hard-time overhauls. For instance, battery cycle strain history is stored to determine future replacement times. This data is recorded in flight and later analyzed on the ground. A diagram showing the flow of data through *Starling*'s HUMS is presented in Figure 14.1.

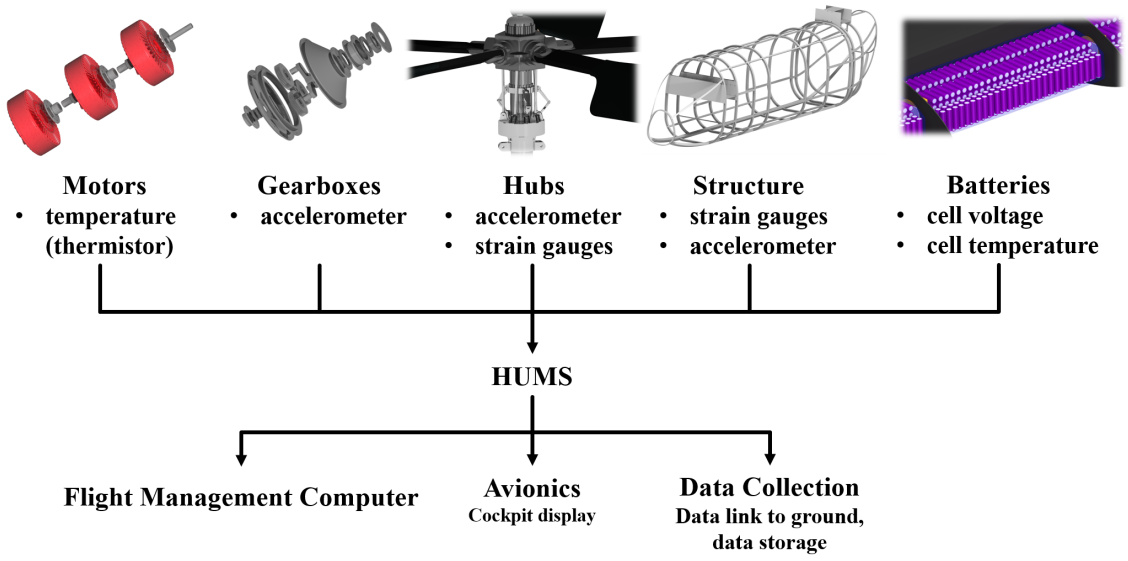

Figure 14.1: Health and Usage Monitoring System (HUMS) flowchart

A breakdown of the *Starling* avionics components and their quantity, manufacturer, weight, and power estimates are presented in Table 14.1. Without the air conditioning and heating units installed, the total weight of the avionics is 62.18 kg and the total maximum continuous power consumption is 1400 W.

Table 14.1: Avionics Breakdown

Name	Quantity	Manufacturer	Net Weight (kg)	Net Power (W)
AFCS	1	n/a	22.68	1000
Flight intercom system	1	Becker Avionics	4.3	120
HUMS sensors	125	n/a	2.5	125
Capacitive touchscreen	1	Honeywell	15	80
Pitot airspeed	3	Honeywell	2.5	9
Angle of Attack	2	Honeywell	2.5	9
IMU	1	Honeywell	1	10
GPS antennas	3	Garmin	0.3	3
Sony IMX490	12	Sony	0.36	10
Transceivers' comm antennas	3	Garmin	0.6	3
Cockpit Voice/Data Recorder	1	Honeywell	6.44	14
Battery Management System	24	n/a	1	2
Collision Avoidance System	1	Garmin	3	15
Radar Altimeter	1	Honeywell	2.29	4
Air Conditioning/Heating	1	RSG	40	1900
Total (w/out AC/Heating)			62.18	1400
Total (w/ AC/Heating)			102.18	3300

15 Acoustics

The *Starling* is designed to operate in urban environments with high population densities. This means that the design has to be as quiet as possible so that it will not be an annoyance to those in the vicinity. In order to achieve this goal, several measures have been taken throughout the design of the aircraft:

1. Low tip speeds in both hover and forward flight.
2. More blades for more evenly distributed thrust on the rotor.
3. Smaller rotors which have a higher blade passing frequency for better blending with typical urban noise.
4. Odd number of blades for reduced resonance between blade acoustic signatures.
5. Phase shifting in rotor rotation for reduced resonance.

In this section the impact of these design decisions is evaluated by predicting the tonal and broadband sound pressure levels produced by the aircraft at the critical flight conditions.

15.1 Noise Mechanisms and Methodology

There are two categories of noise: tonal and broadband.

Tonal Noise

Tonal noise is composed of two different sources, loading and thickness noise. Loading noise is a result of the unsteady aerodynamic loads on the aircraft, while thickness noise occurs due to the air being displaced by the geometry of rotating components. Tonal noise typically occurs at lower frequencies related to the blade passing frequency and its multiples.

The in-house Acoustic Code of the University of Maryland (ACUM) was used to calculate the noise generated by the *Starling*. ACUM propagates tonal noise from surface elements onto the desired set of observers

following the Ffowcs Williams-Hawkings equation. ACUM is capable of using inputs of varied levels of fidelity for acoustic simulations. The most accurate method is to use the complete surface pressure distribution time history, but compact loading in the chord-wise and/or span-wise blade directions can also be assumed. Sectional blade aerodynamic loads from the blade-element momentum theory (BEMT) formulations discussed in Section 6 were used to estimate the rotor tonal noise with compact chord assumption. This method was used for both the hover and cruise conditions. While using BEMT results results in good estimations for isolated rotors, it does not account for the aerodynamic interactions between rotors. Interactions between blades (BVI) are also not accounted for, however the flight conditions for this aircraft involve either hover or axial flow, there will never be substantial BVI.

The locations of the observers for the acoustic analysis of *Starling* were chosen to be the most representative of the experience people will have with the daily operations of the aircraft. Over 700 observers were placed in a hemisphere below the aircraft in order to best understand the distribution of noise at different locations around the rotor.

Broadband Noise

Broadband noise is a result of the interactions between an airfoil and its boundary layer and near wake. This source of noise occurs at a broad range of frequencies, but dominates frequencies much higher than those of the tonal noise. The broadband noise is calculated within ACUM using the Brooks-Pope-Marcolini (BPM) method [51]. The BPM method uses semi-empirical equations to individually estimate six different mechanisms of self-noise which result in the total broadband noise.

15.2 Hover

For the purpose of hover noise estimation, the radius of the hemisphere under the aircraft was chosen to be of 91 m (300 ft), which is approximately equivalent to the altitude of a 30 story building. Placing the landing sites on relatively tall buildings helps mitigate the annoyance caused by the aircraft noise and should not be hard to accomplish in the urban areas for which the aircraft is targeted. The observer locations are depicted in Figure 15.1.

At each of the observer locations shown, the tonal and broadband Sound Pressure Level (SPL) is computed. SPL is the noise at specific frequencies. In order to have a complete picture of the complete sound spectrum, the SPL at all frequencies are integrated to find the Overall Sound Pressure Level (OASPL). Both SPL and OASPL are measured in decibels (dB). Since *Starling* is a quad rotor aircraft, the sound waves from each rotor are added in order to produce the complete acoustic results for the hover condition. The tonal results shown consist almost exclusively of loading noise since the thickness noise is very low and becomes negligible when both sources of noise are added. It can be seen that the maximum tonal noise will be perceived close to the plane of rotation, while the broadband noise is highest directly under the rotor.

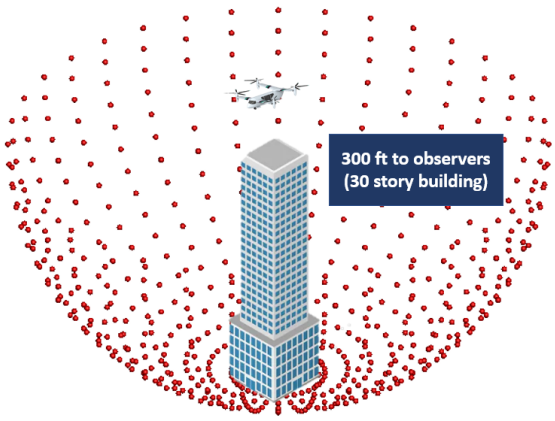

Figure 15.1: 703 observers located in a hemisphere below the aircraft in hover

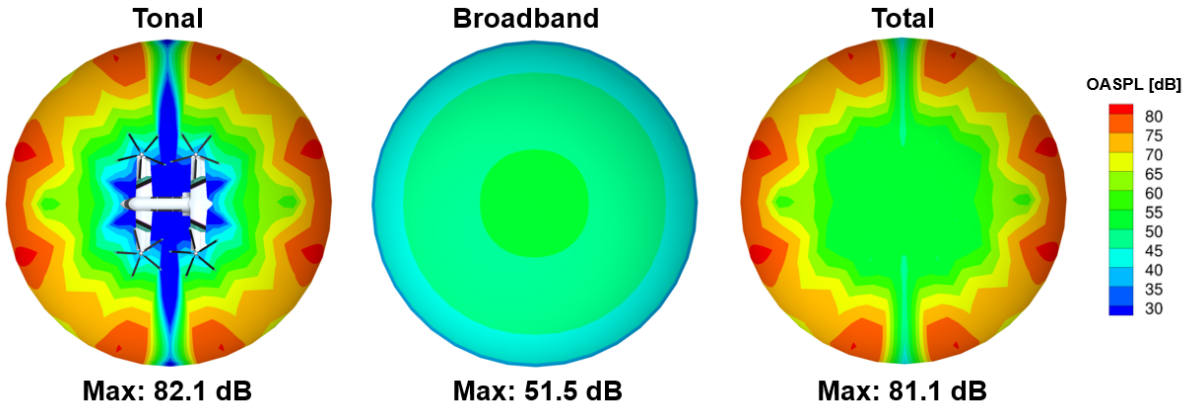

Figure 15.2: *Starling* hover tonal (left), broadband (middle) and total (right) OASPL in dB

Note that, for tonal noise, the relative position of the rotors to each other causes shifting in the phase of the pressure waves from each rotor, resulting in both constructive and destructive wave addition. Since the aircraft has its rotors symmetrically positioned, the noise from the front and rear rotors cancel out at the midpoint. In the regions where the rotor noise resonates there is an increase of 10 dB compared to the maximum noise of an isolated rotor.

The results from the total tonal noise from the four rotors lead to the idea that by shifting the location of the rotors, it could be possible to manipulate the phase shifting of the sound waves. The goal of changing the rotor location would be to decrease the maximum tonal noise at any location at the price of less cancelling of noise at the symmetry plane between the front and rear rotors. Due to physical limitations and the size constraints in the RFP, the largest possible change in location of the rotors is to move one set inboard by 2 ft (0.6 m) and the other set outboard by the same distance. The acoustic results of the asymmetric configuration are shown in Figure 15.3. It can be seen that shifting the position of the rotors increased the total tonal noise by 1 dB, other combinations of change in rotor location were tested as well but the lowest maximum noise remained that of the original symmetric configuration.

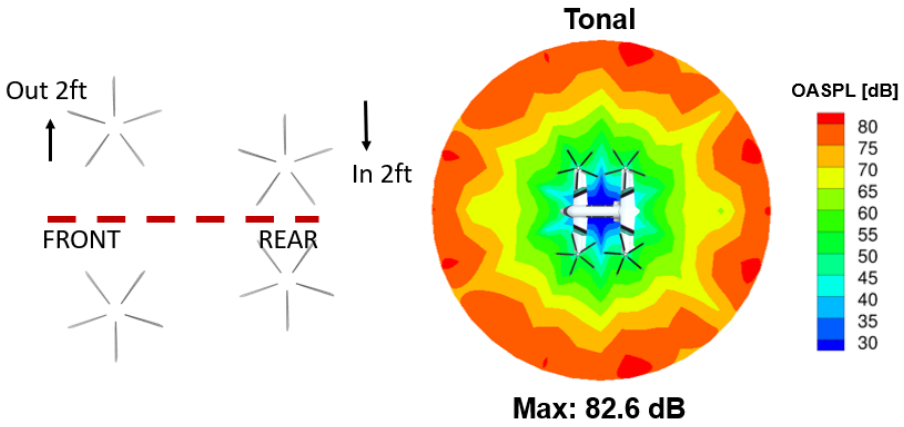

Figure 15.3: Asymmetric configuration hover tonal OASPL in dB

Decibel levels are not the only important characteristic of a sound signal, it is also important to consider the frequency at which the noise occurs. Figure 15.4 shows the SPL distribution in the frequency domain for tonal and broadband noise under 250 Hz. Note that tonal noise occurs only at the first few blade passing frequencies (BPF) while broadband noise continues to increase with frequency. The frequencies at which

sound occurs affect our perception of the noise, and also affects how much energy is lost due to atmospheric attenuation. Sound waves with higher frequencies are more susceptible to attenuation, therefore broadband noise will be attenuated much more than tonal noise. Figure 15.4 shows the attenuation of broadband noise with frequency at a humidity of 10%.

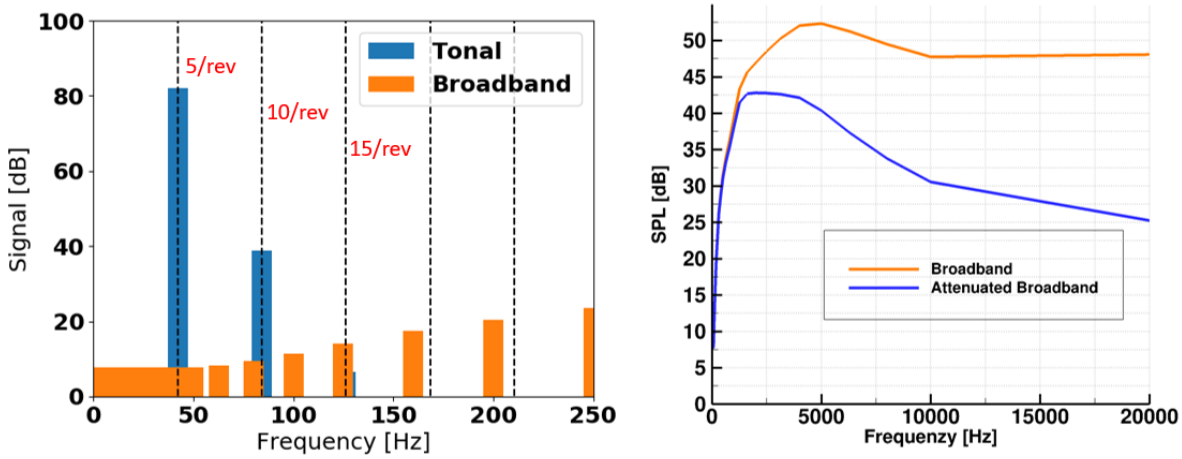

Figure 15.4: Hover SPL for tonal and broadband noise (left), broadband attenuation (right)

The human ear finds some frequencies more annoying than others, so acoustic signals are subjected to an A-weighting in order to give more importance to certain frequencies. The A-weighting affects frequencies lower and higher than 1000 Hz. While the tonal noise of *Starling* is not reduced much by attenuation, it does get reduced by A-weighting since the dominant frequencies are low. Figure 15.5 shows the A-weighting being applied to the attenuated tonal and broadband noise. In this case the tonal noise is reduced more than 30 dB due to its low frequencies. Due to the large decrease in tonal noise, the broadband noise will dominate the A-weighted noise of the aircraft in hover.

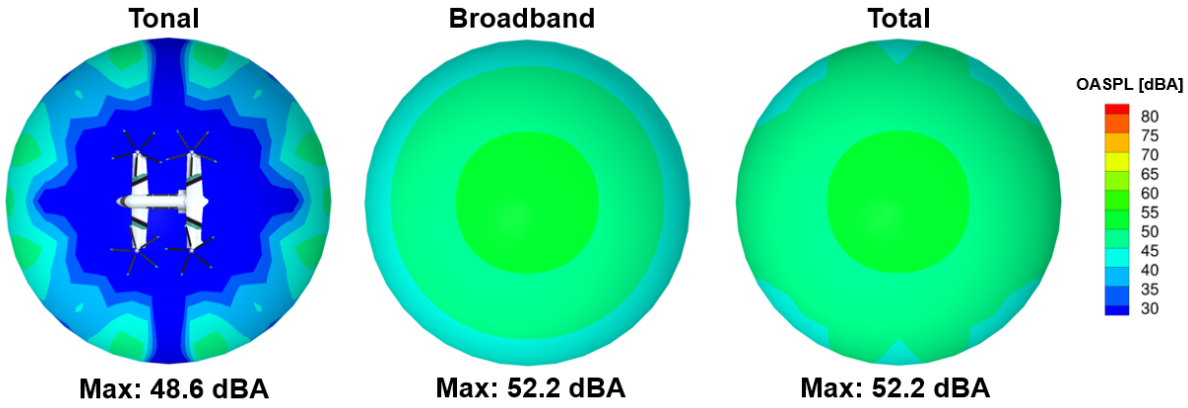

Figure 15.5: *Starling* hover tonal (left), broadband (middle) and total (right) OASPL in dBA

15.3 Cruise

In the cruise condition the observer placement remains similar to that of Figure 15.1 but the radius of the hemisphere is changed to the 610 m (2000 ft) defined in the RFP for cruise.

Starling is designed to reduce the rotor RPM by 55%. This results in the tip speed to be reduced to

60 m/s (200 ft/s) in cruise. This low cruise tip speed combined with the high cruise altitude results in very low noise levels at ground level in the cruise condition. Additionally, the load being carried by the rotor in cruise is only a small portion of the thrust required for hover. Figure 15.6 shows the tonal and broadband OASPL for all proprotors in cruise. Note that the maximum tonal noise is now underneath the aircraft because the plane of rotation has shifted 90 degrees. Similarly, the broadband noise is now maximum behind the aircraft. Note that in this low thrust condition the OASPL for the broadband noise will dominate over the tonal even before an A-weighting is applied. The effects of changing rotor placement were not tested for the cruise condition since the noise levels are already quite low and the large relative distance to the observers makes small changes in position less relevant as sound waves travel.

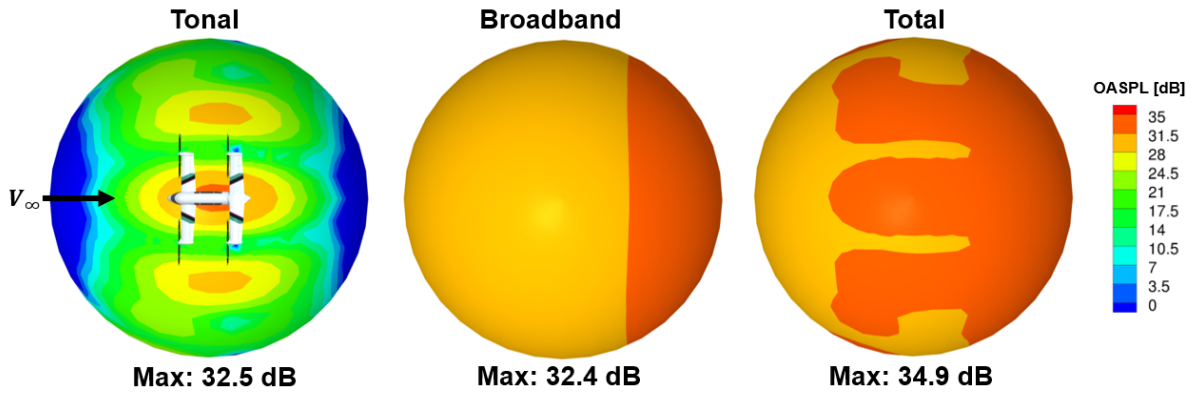

Figure 15.6: Cruise tonal and broadband OASPL

In all the acoustic results so far, the observer noise perception is estimated at an instant in time for a hemisphere under the rotor. In cruise however, this is not representative of the noise experienced by the observer since the aircraft is moving. Figure 15.7 shows the pressure time history and OASPL experienced by a single observer as the aircraft flies over-head in the cruise configuration. The aircraft flies 760 m (2500 ft) horizontally at an altitude of 610 m (2000 ft) with the observer in the middle of the trajectory. The Figure shows that the noise from the aircraft is reduced considerably when it is about 60 m away, so during a flyover, the highest noise levels will only be heard for two seconds since the cruise speed is 60 m/s.

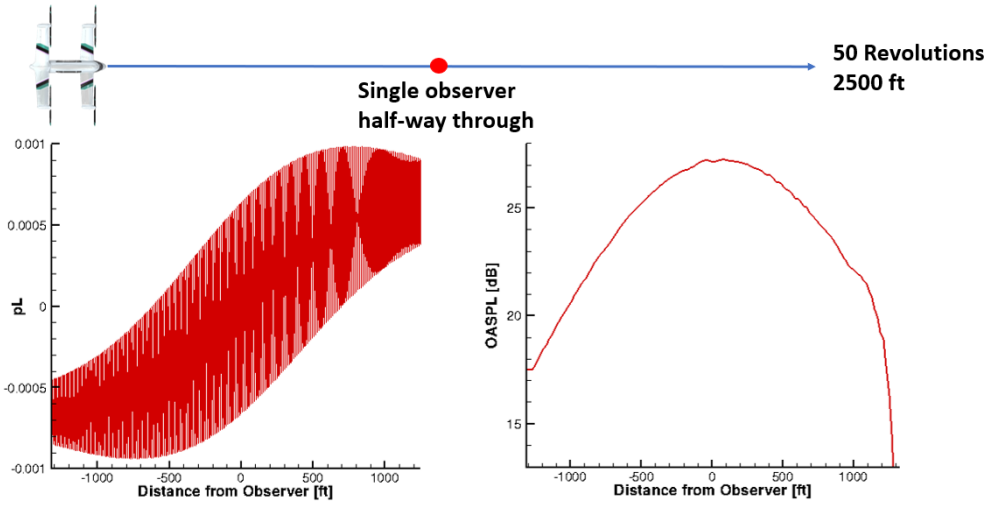

Figure 15.7: Flyover pressure time history (left) and OASPL level (right)

The high cruise altitude means that the effects of sound dispersion as well as atmospheric attenuation will be more significant. Figure 15.8 shows the main SPL frequencies for cruise under 250 Hz. Note that the dominant frequencies are less than half of those in cruise due to the large RPM reduction. The lower blade passing frequency not only implies lower tip speed for lower tonal noise, but also means that the A-weighting will reduce the signal even more than before. Figure 15.8 also shows the attenuation of broadband noise in cruise, it can be seen that the SPL is reduced even at lower frequencies due to the large distance to the observers.

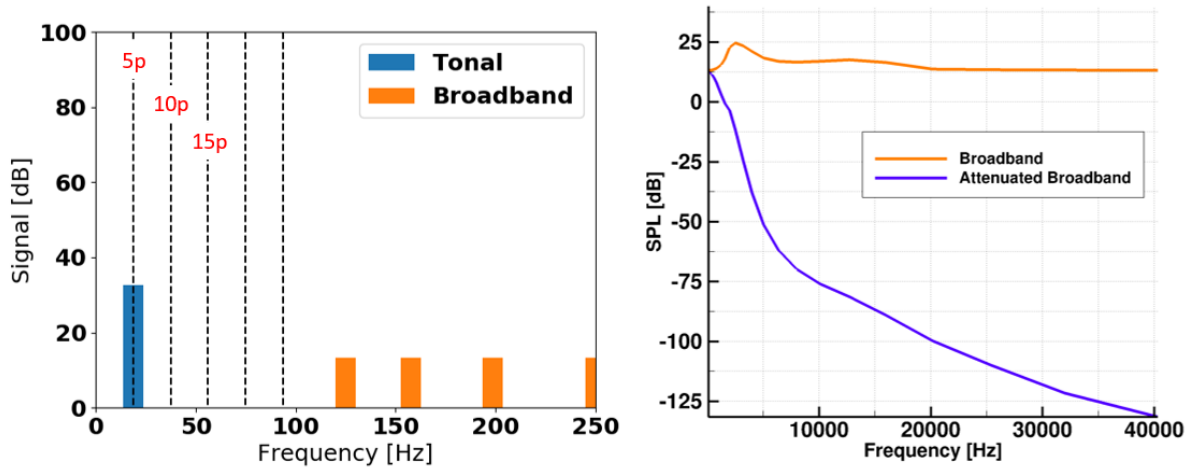

Figure 15.8: Cruise SPL for tonal and broadband noise (left), broadband attenuation (right)

The final attenuated and A-weighted noise results for the cruise condition are depicted in figure 15.9. It can be seen that the A-weighted tonal noise becomes imperceptible in this flight condition due to the low frequency it occurs at. The only contribution to the total noise is the broadband noise, which has a maximum OAPL level of 16 dBA, this means that the aircraft will barely be audible when flying 2000 ft overhead.

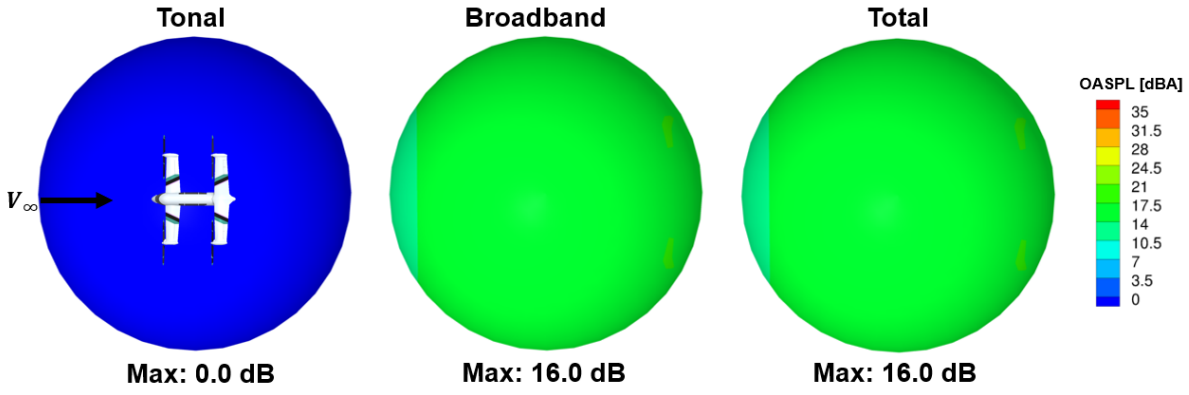

Figure 15.9: Cruise attenuated and A-weighted tonal and broadband OASPL

15.4 Cabin Noise

The comfort of the passengers is paramount, therefore attention is also paid to the noise levels within the cabin during flight. To achieve this, a plane of observers was placed two meters under the rotors to simulate the cabin level. Simulations were performed in cruise since this constitutes a majority of the time spent.

The total OASPL from tonal and broadband noise was calculated and an A-weighting was performed. After the A-weighting the broadband noise became the dominant source. With current sound insulation technologies it is safe to assume that a 20 dB acoustic transmission loss can be assumed throughout the aircraft [52], particularly since these materials work best on the higher frequencies that are unaffected by A-weighting. Figure 15.10 shows the OASPL contours outside the aircraft as well as inside the cabin area where 20 dB transmission loss was assumed. It can be seen that the OASPL around the cabin is about 80 dBA, which results in a 60 dBA cabin noise.

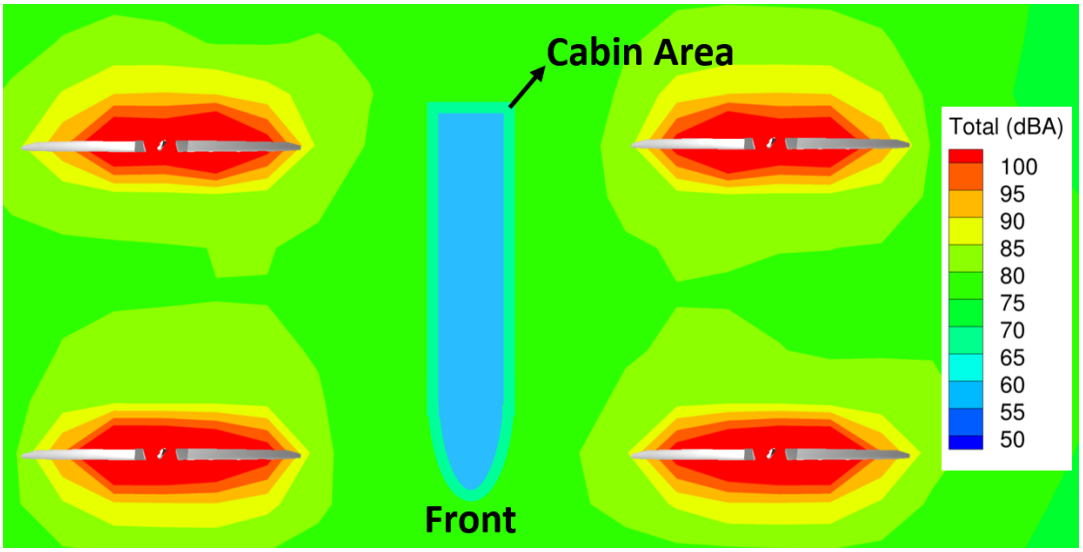

Figure 15.10: Cruise attenuated and A-weighted tonal and broadband OASPL

15.5 Effect of Aerodynamic Interactions on Noise

The methodologies used for acoustic analysis in this section are not able to account for the aerodynamic interactions between the rotors and the wings. The cruise configuration for the *Starling* is a case with high interactions due to the close proximity and relative position of the thrust and lifting components. Because of the importance of these interactions, the BEMT based acoustic analysis presented is an under-prediction of the noise values of this aircraft. Higher fidelity acoustic analysis can be performed to better capture these effects by using 3-D CFD pressure distributions to generate the acoustic surfaces. Figure 15.11 shows the root mean squared (RMS) pressure coefficient values on the lifting and thrusting surfaces of the aircraft for a full revolution. Large 5/rev pressure fluctuations can be seen on the section of the wing directly behind the rotor which will result in loading noise production from the wing. Research has shown that large wings directly behind a rotor can produce equivalent or even larger noise than the rotor itself [53]. Future work in the development of the *Starling* would involve post-processing the CFD simulations performed in this report to better understand the complex acoustics.

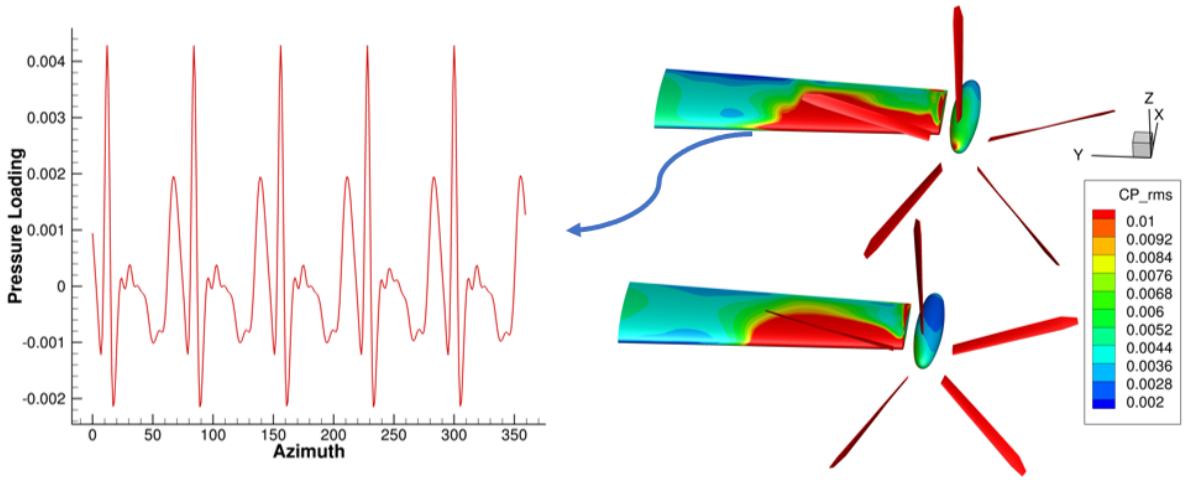

Figure 15.11: Wing pressure loading (left) and surface RMS pressure values from CFD (right)

The *Starling* was designed to perform its mission without disturbing the populated areas it will operate in. The tonal and broadband noise analysis shown in this section has shown that the rotor design allows for quiet operation in both hover and forward flight conditions both in and outside the cabin. More accurate acoustic predictions, in both frequency and magnitude, can be attained with future work using CFD analysis to capture interactional aerodynamics.

16 Vehicle Performance

16.1 High-Fidelity Drag Estimation

The flat plate area of the vehicle is estimated by decomposing it into isolated components and summing their contributions. The vehicle is broken down into a fuselage, two wings, four nacelles, four wing-fuselage junctions, and "Miscellaneous", which accounts for skin gaps, antennae, etc. Drag contributions are estimated as if *Starling* is in cruise. An isolated fuselage body was meshed and analyzed using an in-house 3D RANS solver at a 2.5° body pitch angle. The forward and aft wing contributions are estimated by determining the wetted area of the wings in flight and multiplying by the profile drag coefficient of the airfoil. This airfoil drag changes with angle of attack, so the wings were assessed at their nominal cruise angles of attack of 2.5° forward and 5° aft, respectively. Like the fuselage, 3D RANS was utilized to better estimate the nacelle drag at the respective angles of attack coincident with the wing. The interference drag at the wing-fuselage junctions was estimated using the methodology presented by Prouty [23]. Lastly, an addition for miscellaneous features that increase the total drag of the vehicle is added to account for antennae, skin gaps, etc. The breakdwon is shown in Table 16.2.

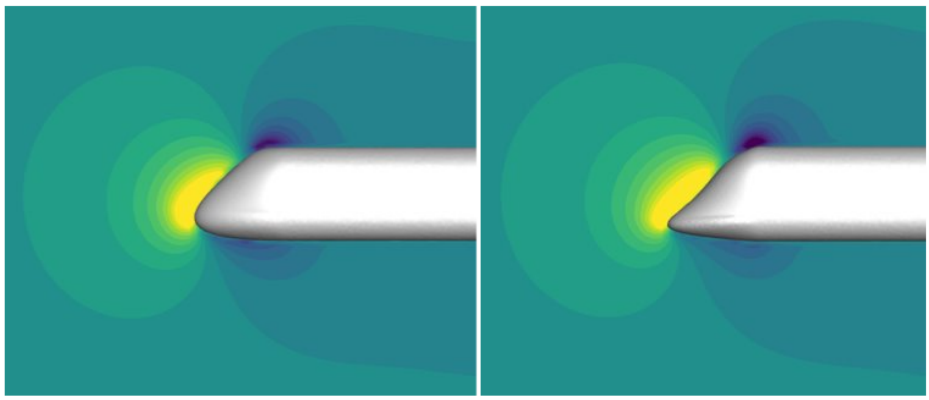

Figure 16.1: Pressure distribution around fuselage for two different nose shapes

Table 16.1: Fuselage Nose Shape Comparison

Nose Shape	Downforce - N (lbf)	Drag - N (lbf)
Round	564.0 (126.8)	431.5 (97.0)
Pointed	641.0 (144.1) +13.6%	460.4(103.5)
+6.7%		

Two different fuselage nose shapes were tested for best performance in cruise, the pressure distribution for both of these cases is shown in Figure 16.1. Table 16.1 shows the lift and drag forces resulting from the two different nose types. The round nose results in both lower drag and downforce. The downforce is caused by the low position of the nose relative to the center of the bode, this trait was kept anyways for practical cabin design and due to the low percentage of the lift that this represents.

Table 16.2: Drag breakdown

Component	Flat Plate Area - m^2 (ft^2)	% Contribution
Fuselage	0.1977 (2.1280)	30.93
Forward wing	0.1336 (1.4379)	20.90
Aft Wing	0.1401 (1.5084)	21.92
Four nacelles	0.0882 (0.9495)	13.80
Four wing-fuselage junctions	0.0331 (0.3564)	5.18
Miscellaneous	0.0465 (0.5000)	7.27
Total	0.6392 (6.8802)	100

The RANS calculations were essential for credible estimate of the fuselage drag which historical values underestimated. The large wing area and additional wing fuselage junctions account for the additional drag on top of the sizing estimate leading to a more realistic Harris factor of 1.97.

16.2 Vehicle Download

Download from the rotor wash in hover is a common factor for all tilt-rotor aircraft. To minimize this, designs often incorporate large trailing edge flaps or ailerons that can deflect out of the way, decreasing the planform area the rotor wake impinges on. The XV-15 hover tests show about 7-8% penalty and high flap deflection modifies the aerodynamics of the wake on the wing, prolonging flow separation and reducing the drag coefficient [54]. *Starling* flaperons span 30% of the wing chord and are designed to deflect down 70° in hover to reduce the wetted planform area of the wing and decrease its drag profile, shown in Fig. 16.2. Momentum theory is used alongside a hover prescribed wake model to determine the wake contraction and

velocity at the wing. Maximum GTOW is assumed along with drag coefficient estimates equal to those obtained experimentally in the XV-15 tests, 1.7 for no flap deflection and 1.3 with flap deflection. With the reduction in frontal area from flap deflection, the download is calculated and shown in Table 16.3 as a percentage of the weight. The results are consistent with 0.658 scale V-22 hover tests conducted that show a minimum download of 7.5% at a flap deflection of 70° to 80° [55]. This analysis substantiates the download estimated during vehicle sizing.

Table 16.3: Download in Hover

Flap Configuration	Download(% Weight)
No deflection	15.34
70° deflection	7.58

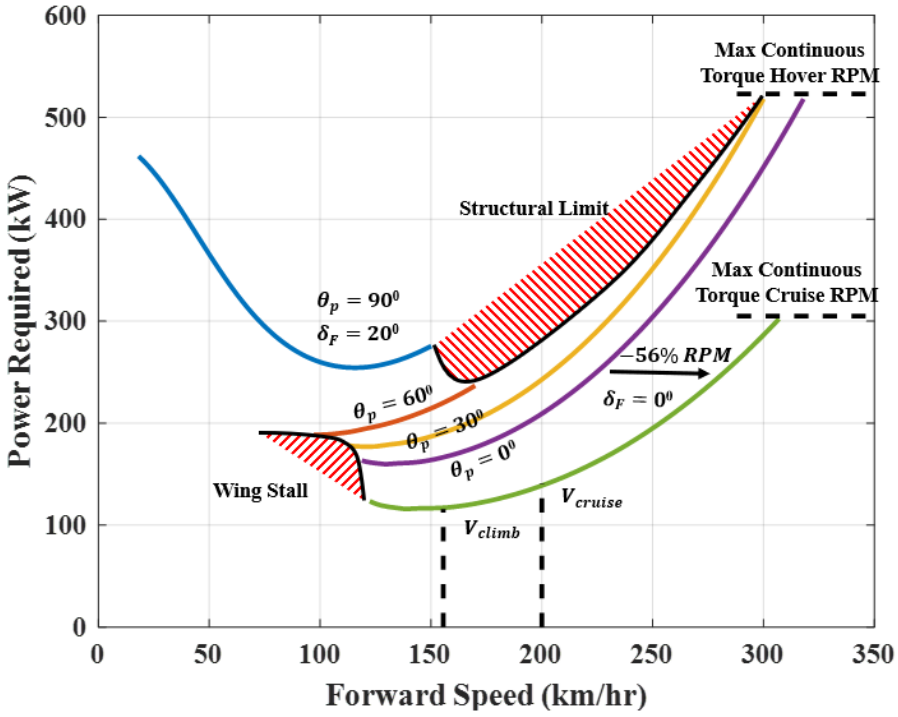

Figure 16.3: Power required variation with pylon conversion in forward flight

16.3 Hover and Cruise Performance

Cruise and conversion analysis was conducted using a solver that trims the rotor and wing lift share and converges to a body pitch at a specified pylon angle. Fig. 16.3 shows the power required with forward speed as the pylons are progressively tilted down. In forward flight up until full conversion to airplane mode, the flaperons are deflected 20° to reduce the stall speed by increasing C_{lmax}. To simulate the hub drag, the flat plate area is increased steadily from 1× the drag estimate at a 0° pylon angle, airplane mode, to 2.5× at a 90° pylon angle, helicopter mode. The left boundary of each curve represents wing stall, except for $\theta_P = 90°$. The right boundary of each curve is either a structural limit or a torque limit from the drive at the relevant RPM. A maximum advance ratio of $\mu = 0.3$ is set to limit the oscillatory loading on the blades and hub in transition. This defines the structural limit shown in the figures. This advance ratio is quite high, but with lower tip speeds is seen at lower forward flight speeds. As the wing takes on more and more of the lift share, the benefit is seen in the reduction in power and increase in L/D (Fig. 16.4). A large increase in L/D is seen from the reduction in RPM which agrees with validated predictions

from the higher fidelity analysis [56], substantiating the simplified model.

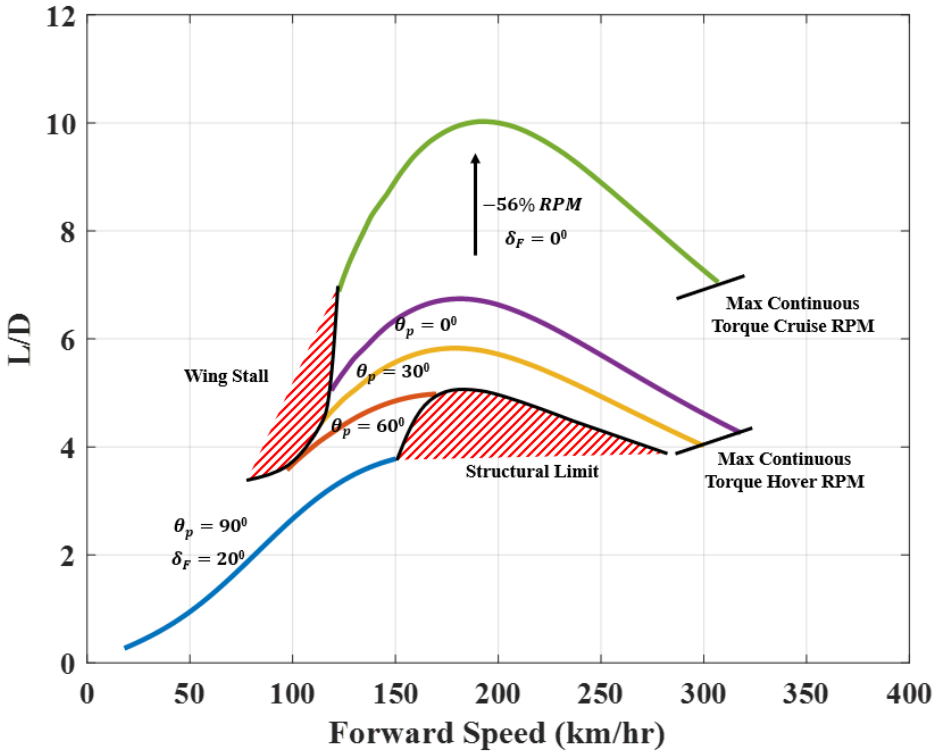

Figure 16.4: Lift-to-drag ratio variation with forward speed and pylon conversion

A nominal cruise speed of 200 km/hr (108 kts) was selected as the cruise speed for max L/D of 10. The climb speed was selected to be at 155 km/hr (83.6 kts) to maximize the achievable climb rate in off nominal conditions. *Starling*'s maximum rate of climb at this airspeed is 7.58 m/s (24.9 ft/s). The nominal rate of climb is 6.8 m/s (22.35 ft/s). The pilot may climb at hover RPM to achieve a higher rate of climb if needed. In this case, the power required at this airspeed is 44% higher, however, the maximum rate of climb increases to 15.45 m/s (50.7 ft/s).

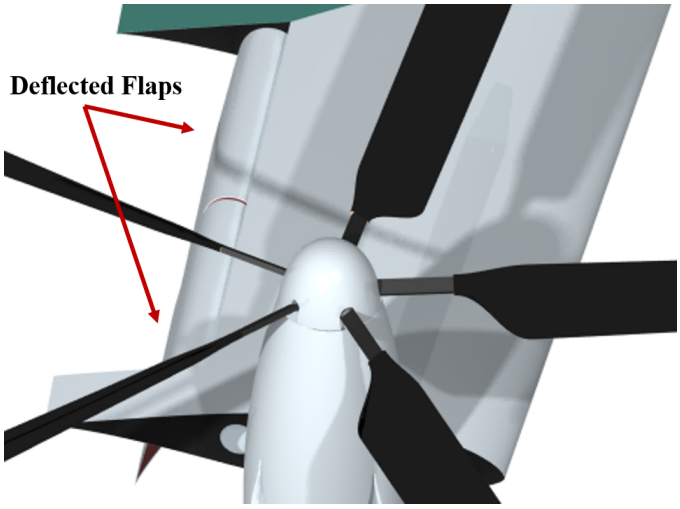

Figure 16.2: Flap deflection to reduce download in hover

16.4 Intrinsic Performance

From the forward flight performance a maximum operating speed is determined, V_{MO} = 277.8 km/hr (150 kts), and the conversion corridor is generated and shown in Fig. 16.5. The conversion corridor displays forward flight speed limits with nacelle angle and the recommended route of conversion. The corridor is bounded at low speed by wing stall and high speed by the structural limitation previously described as well as drive system limits. The blue dots indicate the path of best L/D through the corridor, however this route touches the structural limit giving no margin in the event the pilot must suddenly

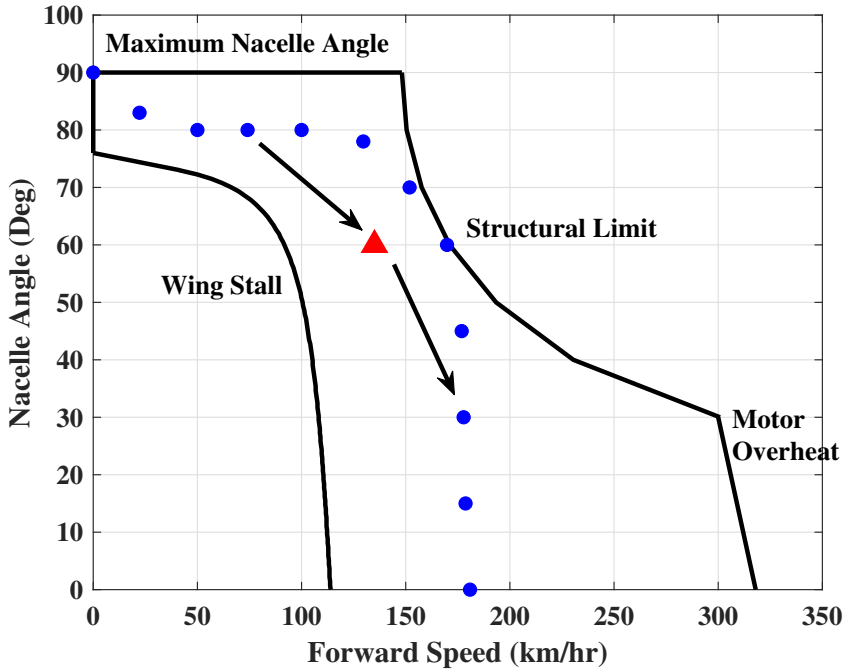

Figure 16.5: Conversion corridor with recommended route

accelerate. Therefore, the red triangle indicates the recommended route through the corridor to provide adequate margins between the stall and structural boundaries.

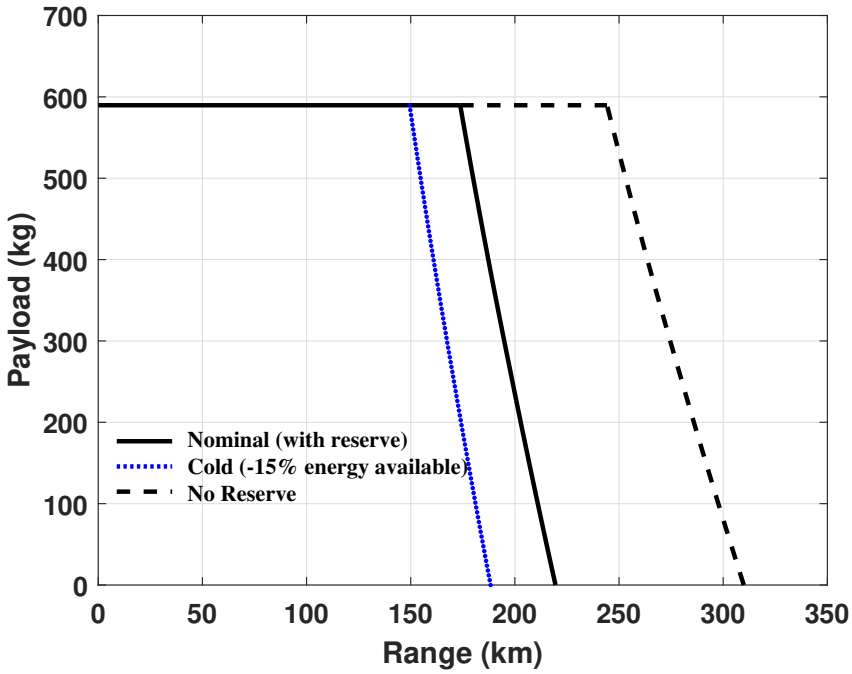

Figure 16.6: Achievable range with varying payload

The *Starling's* excellent range capability can be seen in Fig. 16.6. At maximum payload, an achievable range at nominal operating conditions extends to 175 km (108.7 mi). If necessary, the mission at maximum

payload could be extended to almost 250 km (155.3 mi) if the reserve energy within the batteries is required. Cold weather increases the internal resistance of the batteries, reducing its usable capacity. In this scenario, it is estimated 85% of the total energy (without reserve energy) is available and a range at maximum payload of 150 km (93.2 mi) is still obtainable. Relative to current eVTOL designs, the *Starling* shines in its payload capability, shown in Fig. 16.7, outperforming all market designs.

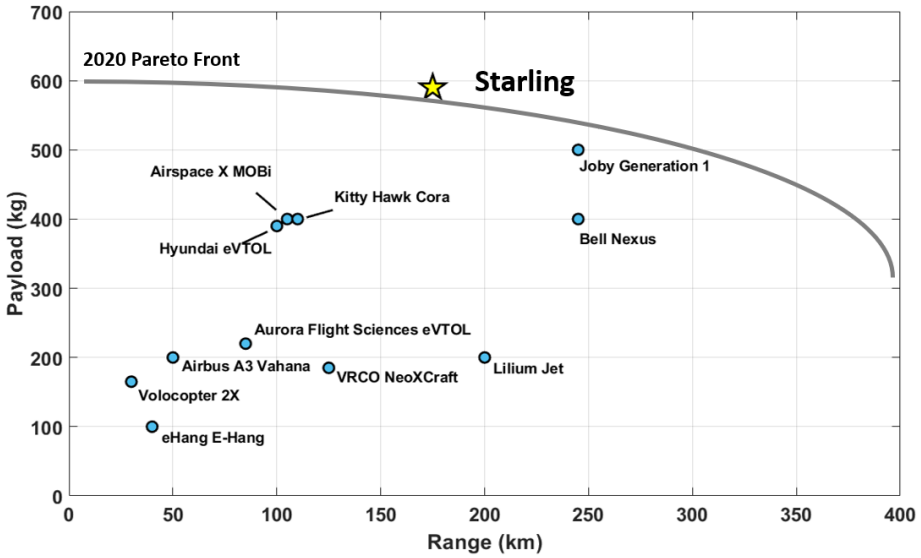

Figure 16.7: Achievable range with varying payload

Starling intrinsic performance is displayed in Fig. 16.8. The maximum takeoff altitude is defined as the altitude at which the maximum continuous power available from the drive system is equal to that required to hover. Similarly, the maximum operating altitude is defined as the maximum continuous power available being that required to maintain a climb rate of 30.48 m/min (100 ft/min) at the forward speed for minimum power in cruise. Despite having the capability to takeoff and operate at altitudes well beyond the design condition, a limit is set on nominal operation at an altitude of 2,438m (8,000 ft) which is the maximum cabin pressure altitude allowed by 14 CFR §25.841. As a result, *Starling* is not equipped with a cabin pressurization system. If absolutely necessary, *Starling* may exceed this altitude up to maximum operating and takeoff conditions so long as an altitude of 4,572 m (15,000 ft) is never exceeded. This limit is not affected by battery loss in capacity.

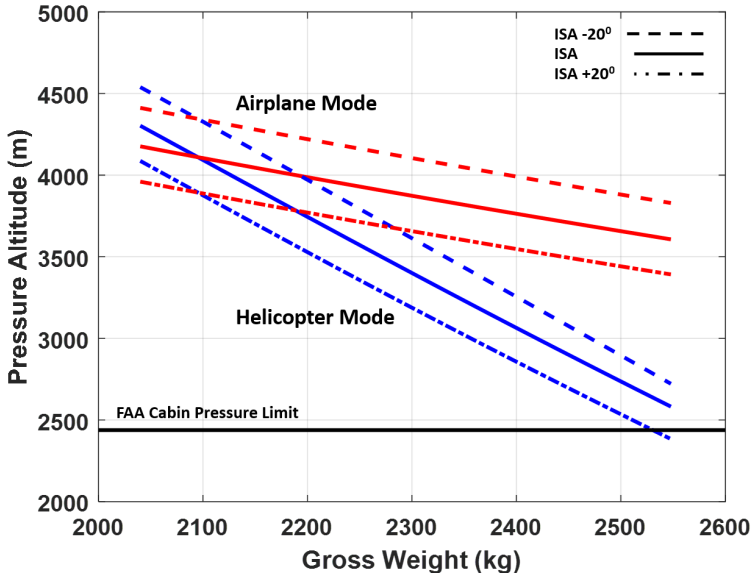

Figure 16.8: Maximum takeoff and operating capability

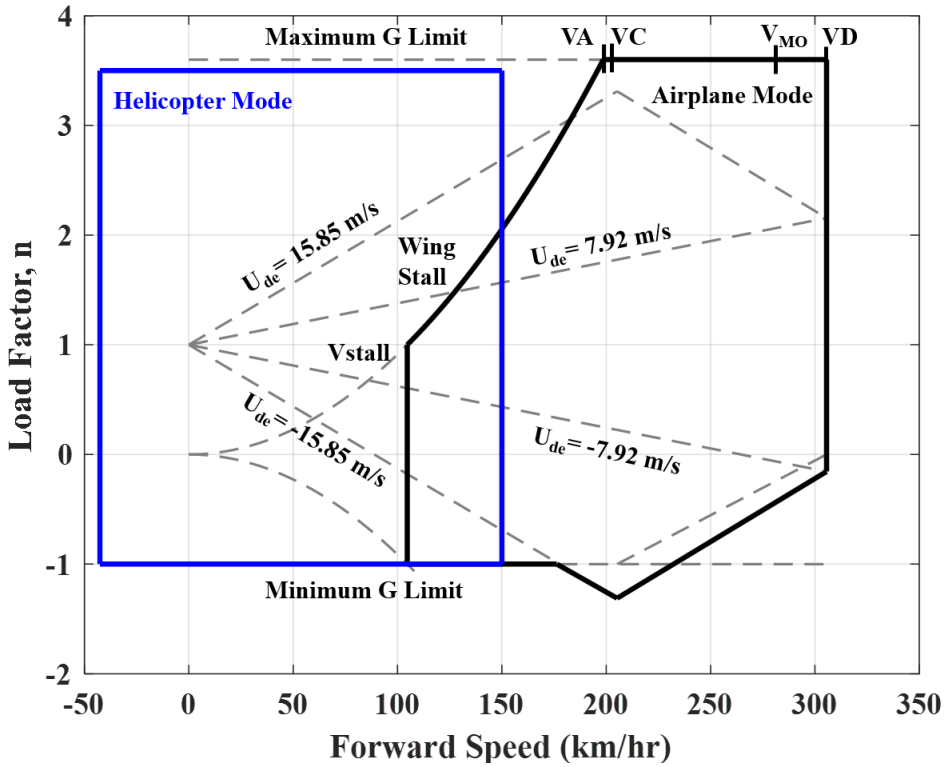

Figure 16.9: Full operation envelope

16.5 Flight Envelope

Two V-n diagrams are needed to capture the diverse operational capability that *Starling* provides. The flight envelope represents the limits of structural capability, one for fully converted airplane mode and the other for helicopter mode, similar to the XV-15 [57]. Fig. 16.9 displays the limit load factors in airplane and helicopter mode on the same figure, primarily bounded by stall limits and limit maneuvering and gust

loads set forth by 14 CFR 25.337 and 25.341, respectively. The gust boundaries are developed through the methodology presented in Gudmundsson [13], identifying the ultimate limit load factor, n_{ult} at every operating speed. The helicopter mode operating regime is much simpler. At such low speeds, the gust loads do not have an impact on the boundaries of this envelope, therefore *Starling* is simply bounded by the maneuvering limit loads set forth in 14 CFR 29.337. *Starling* is capable of flight up to 42.6 km/hr (23 kts) at any azimuth in helicopter mode. Greater forward speeds are achievable as the wings are placed at an incidence angle, so even in helicopter mode *Starling* flies as a lift compounded helicopter. The forward flight speed in helicopter mode is limited by the structural limit presented earlier. These two diagrams together define the full operating regime of *Starling* and the ultimate load factors for loads analysis in each operating condition. Figure 16.10 presents the variation of gross weight with load factor. Increasing the structural tolerance to the loads it can support increases the gross weight. A heavier, stronger structure is correlated with one that can handle higher loads.

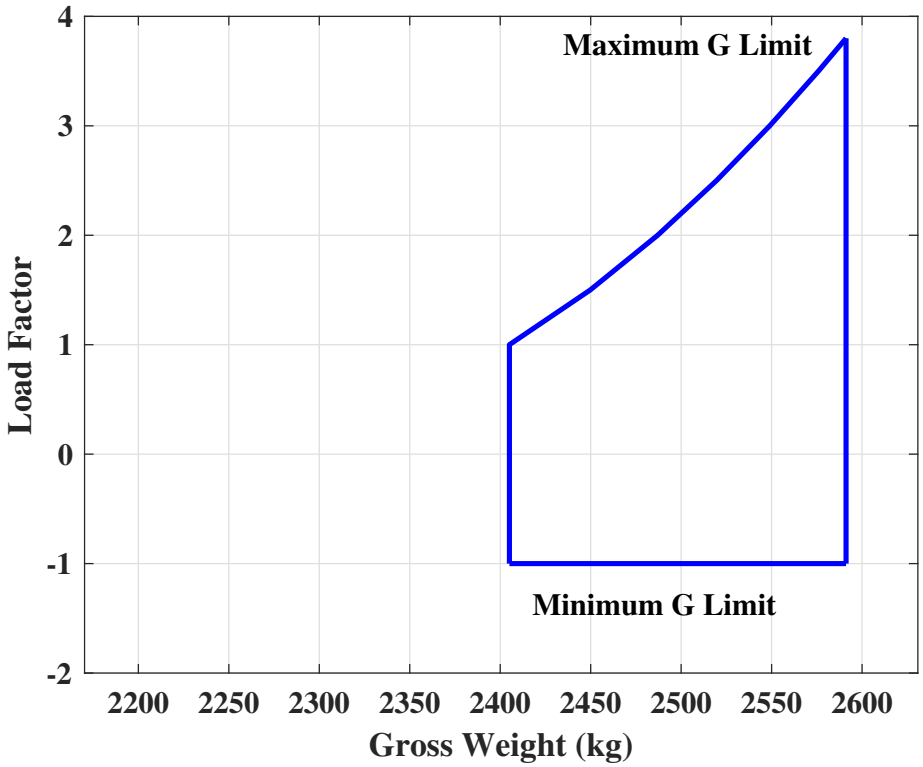

Figure 16.10: Limit maneuvering load factor vs. gross weight

17 Cost Analysis

Using the NDARC cost estimation procedure, *Starling's* cost was broken up into three categories: purchase price, maintenance cost, and operating cost. All three methods are constructed using empirical prices for existing aircraft and historical maintenance costs. As a commercial vehicle, additional analysis was provided to establish a path toward profitability.

17.1 Aircraft Flyaway Cost

The aircraft purchase price was estimated using a high-fidelity model by Robert Scott [58]. The Scott rotorcraft cost model utilizes parametric equations to estimate the cost of individual components. The higher fidelity model allows for eVTOL specific costs, such as brushless motors and batteries, to be included directly. The Scott model predicts the unit flyaway price to within 9.3% error for military aircraft and 36.0% for civil helicopters.

The flyaway cost of the aircraft is defined as:

$$C_{\text{FA}} = \chi(F_i c_{\text{FA}}) + C_{\text{comp}} \tag{10}$$

c_{FA} is the flyaway cost of the vehicle and is modified by technology factor χ and inflation factor F_i.

$$c_{\text{FA}} = c_{\text{pq}} + c_{\text{int+SE}} + c_{\text{profit}} \tag{11}$$

The unit flyaway cost c_{FA} is a summation of the prime equipment production, integration & systems engineering, and profit costs. The prime equipment production cost consists of all of the costs for aircraft components. For commercial and civil aircraft, $c_{\text{int+SE}}$ and c_{profit} are found as a percentage of the prime equipment production cost.

$$c_{\text{int+SE}} + c_{\text{profit}} = f c_{\text{pq}} \text{ where } f \approx 0.25 \tag{12}$$

eVTOL companies, particularly Joby, are able to reduce their vehicle's flyaway cost in large part due to cooperative efforts with its major investors. In addition to investing $394 million into Joby, Toyota Motors also shared "its expertise in manufacturing, quality and cost controls" to aid in development and production of the S4, which significantly reduces the cost of the vehicle. Based on this information, a technology factor of $\chi = 0.5$ was used with the assumption that *Starling* would undergo a similar procedure. From this analysis, *Starling* is estimated to have a flyaway cost of **$2,450,000**.

17.2 Maintenance Cost

Maintenance cost includes the labor cost of periodic maintenance as well as the costs for replacement parts. This cost value is calculated using empirical equations by Harris [59]. The number of man-hours for maintenance is estimated as $M_{\text{labor}} W_E^{0.78}$, where M_{labor} is a labor constant that we assume 0.0017 for best practice. The maintenance cost per flight hour is calculated as:

$$C_{\text{maint}} = \chi F_i (c_{\text{pats}} + c_{\text{engine}} + c_{\text{major}}) + C_{\text{labor}} \tag{13}$$

where C_{maint} is the cost in dollars per hour, χ is the technology factor, and F_i is the inflation factor. Based on these calculations, *Starling* has a total maintenance cost of **$771/hr** with $\chi = 0.5$.

17.3 Operational Cost

The operational costs includes costs pertaining to crew, depreciation, insurance, maintenance, and financing. The operating cost is calculated using Equation 14.

$$C_{\text{OP}} = T_F C_{\text{maint}} + C_{\text{crew}} + C_{\text{dep}} + C_{\text{ins}} + C_{\text{fin}} \tag{14}$$

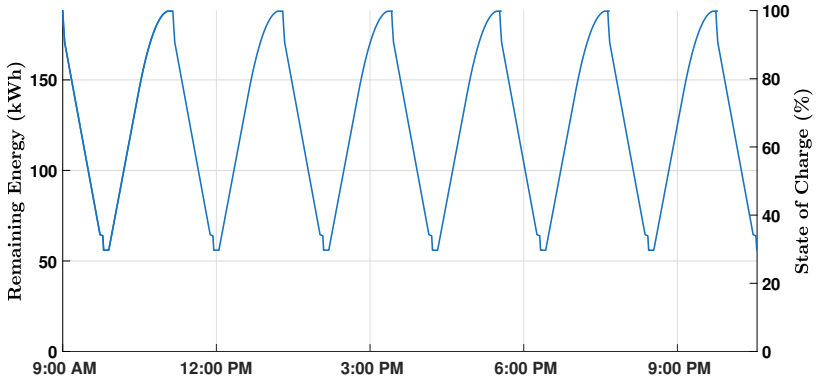

Figure 17.1: *Starling* can complete seven 160.9 km (100 mi) trips in one day with a 250 kW charge rate

Figure 17.1 shows that *Starling* can complete 7 trips in one day, which roughly estimates out to 2,555 trips in a year. With this in mind, the operating cost for *Starling* is **$2,974,000**. Each mission costs **$1,164.18**, or about **$7.24/km ($11.64/mi)**. Per passenger, the cost per mile is **$1.81/km ($2.91/mi)**.

The total life-cycle cost is the summation of the flyaway and the operational cost and is calculated to be **$61,935,000** assuming 2,555 trips over 20 years.

18 Multi-Mission Capabilities

Starling has a robust design that can be easily adapted for other critical missions as outlined in Figure 18.1.

(a) Fire fighting on mountain

(b) Search and rescue in flood

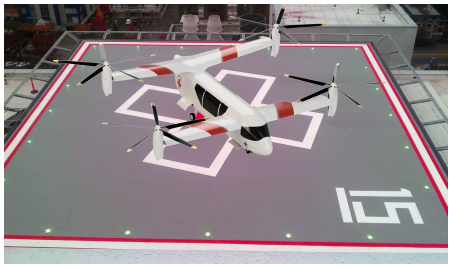

(c) Medevac at city center hospital

(d) Anti-poaching efforts in Kruger National Park

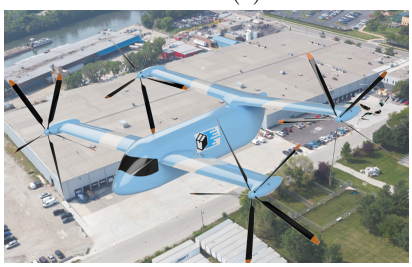

(e) Cargo delivery to and from warehouse

Figure 18.1: Multi-Mission Capabilities

18.1 Fighting Wildfire

Starling can be modified to succeed in firefighting capabilities. The aircraft's avionics package can be upgraded to a fully autonomous one, and this upgrade would allow *Starling* to carry upwards of 0.59 kL (155.8 gal) of water within its fuselage. Its cruise speed allows it to reduce water refill turnaround time. Its lifecycle cost makes it a cost-efficient option for fire-fighting departments to adapt into existing fleets.

18.2 Natural Disasters and Humanitarian Crisis

The threat of global warming increases the prevalence and intensity of natural disasters in the United States. These events cause significant damage and massive displacement of humans in the areas they affect. *Starling* is designed to carry a payload greater than existing eVTOL so it deliver supplies to affected areas. Its low downwash makes it a good option for human rescue. The 12 cameras that *Starling* uses for autonomous landing can also be repurposed to aid in searching and identifying natural disaster victims. Its quadrotor configuration makes it good at rejecting gusts in disaster areas.

18.3 Medevac

Starling can leverage several design aspects to allow it to be a good vehicle for flight. Its high payload capability allows the aircraft to transport several patients to nearby hospitals. Its optimization for cruise allows for a low trip time from pick-up to hospital.

18.4 Wildlife Conservation

Several key features of *Starling* make the vehicle a natural fit for wildlife conservation efforts. Its low acoustic signature allows conservationists to approach poachers with limited detection and disturbance to wildlife. *Starling* also produces zero emissions, which preserves the health of the biological ecosystem. Its use of unified flight controls makes piloting intuitive and reduces the pilot's workload, thus decreasing the time for conservation ranger training.

18.5 Aerial Delivery

Many current strategies for last-mile delivery are designed to carry heavy payloads via ground transport; however, these methods are inefficient for deliveries of smaller payloads at lower ranges, such as warehouse-to-warehouse delivery. As a result, a well-defined niche market for short- and mid-range delivery opens up for eVTOL like *Starling* to successfully fill in. *Starling* boasts a low maintenance cost and long fatigue life that extends its operational longevity. As mentioned in Section 14.1, *Starling* can be outfitted with autonomous navigation avionics package. Removal of the human pilot allows for *Starling* to carry 589.7 kg (1,300 lb) of packages between warehouses.

19 Summary

The University of Maryland Graduate Design Team designed *Starling*, a quad-tiltrotor eVTOL that equitably caters to all kinds of passengers, to meet all of the vehicle and operational requirements set forth in the Request for Proposal for an eVTOL Air Taxi for Passengers for Reduced Mobility (PRMs) for the 2022 Vertical Flight Society Design Competition. *Starling* is designed to be highly efficient to achieve flight distances at much greater payload weights than existing eVTOLs.

1. Variable speed proprotor design allows for a 55% reduction in tip speed to achieve both strong hover and cruise efficiency.
2. The cabin is reconfigurable at will to accomodate either 4 able-bodied passengers or 2 PRMs without the need of specialty hardware.
3. Three stacked motors per rotor provide a fail-safe motor design that has zero impact on aircraft opertion and functionality in case of the loss of one motor.
4. Novel pylon tilting mechanism that allows it to fit comfortably inside the wingbox without compromising the wing structure.
5. Two-wing design allows for 50-50 lift share at low wing loading in cruise, leading to a compact design that enables larger rotors.
6. Unified flight control makes learning to fly the aircraft intuitive by reducing pilot-induced errors.
7. Numerous safety design considerations, such as low download, low fuselage, and batteries places away from the cabin, built-in to ensure absolute safety for all passengers.

References

[1] Chretien, P., "The Quest for the World's First Electric Manned Helicopter Flight," *Vertiflite*, Vol. 58, No. 2, March-April, 2012, pp. 38–42.

[2] Schneider, D., "Helicopters Go Electric," *IEEE Spectrum*, Vol. 49, No. 1, January, 2012, pp. 11–12.

[3] Shi, F. and Brockschmidt, A., "Fault Tolerant Distributed Power," *Proceedings of Applied Power Electronics Conferences, 1996*, Mar. 3 – 7, 1996.

[4] Datta, A. and Johnson, W., "Powerplant Design and Performance Analysis of a Manned All-Electric Helicopter," *Journal of Propulsion*, Vol. 30, No. 2, February 2014, pp. 490–505.

[5] Jonas, A., "eVTOL/Urban Air Mobility TAM Update: A Slow Take-Off, But Sky's the Limit," *Morgan Stanley Research*, May 2021.

[6] Shell and Deloitte, "Decarbonizing Aviation: Cleared for Take-off," *Royal Dutch Shell*, 2021.

[7] Saaty, R., "The Analytic Hierarchy Process—What It is and How It is Used," *Mathematical Modelling*, Vol. 9, No. 3-5, 1987, pp. 161–176.

[8] Pugh, S., *Total Design: Integrated Methods for Successful Product*, Cambridge University Press, 1st ed., 1991.

[9] Rizzi, S. A., "Urban Air Mobility Noise: Current Practice, Gaps, and Recommendations," NASA-TP 5007433, 2020.

[10] Maurya, S. K., Chopra, I., and Datta, A., "Steady and Unsteady Hover Test of a Lift Compounding Rotorcraft," *AIAA SciTech 2022 Forum*, San Diego, CA, Jan. 3–7, 2022.

[11] Lopez, M., Tischler, M., Juhasz, O., Gong, A., Sanders, F., Soong, J., and Nadell, S., "Flight Test Comparison of Gust Rejection Capability for Various Multirotor Configurations," *75th Vertical Flight Society Annual Forum*, Philadelphia, PA., October 6 – 8, 2019.

[12] Johnson, W., "NDARC: NASA Design and Analysis of Rotorcraft," NASA-TP 2015–21875, Apr. 2015.

[13] Gudmundsson, S., *General Aviation Aircraft Design: Applied Methods and Procedures*, Elsevier Inc., 2nd ed., 2014.

[14] Walpole, S. C., Prieto-Merion, D., Edwards, P., Cleland, J., Stevens, G., and Roberts, I., "The weight of nations: an estimation of adult human biomass," *BMC Public Health*, 2012.

[15] Ampofo, A. G. and Boateng, E. B., "Beyond 2020: Modelling Obesity and Diabetes Prevalence," *Diabetes Research and Clinical Practice*, Vol. 67.

[16] Center for Disease Control, "Adult Obesity Prevalence Maps," `https://www.cdc.gov/obesity/data/prevalence-maps.html`.

[17] Bousman, W. G., "Airfoil Dynamic Stall and Rotorcraft Maneuverability," NASA-TM 209601, Jul. 1 2000.

[18] Song, Z., Li, K., Cai, Z., and Wang, Yingxun Liu, N., "Modeling and maneuvering control for tricopter based on the back-stepping method," *Chinese Guidance, Navigation and Control Conference*, 2016.

[19] Zolbayar, B.-E., *Investigation of noise from electric, low-tip-speed aircraft propellers*, Master's thesis, The Pennsylvania State University College of Engineering, State College, PA, August 2018.

[20] Johnson, W., "A Quiet Helicopter for Air Taxi Operations," NASA-TN 76202, Jan. 23, 2020.

[21] Ryseck, P., Chopra, I., Singh, R., Glover, E. D., and Lopez, M., "Steady and Transient Hover Performance Investigation of Electric Medium-sized Variable-RPM Rotor," *78th Vertical Flight Society Annual Forum*, Fort Worth, Texas, May 10–12, 2022.

[22] Stoll, A. and Bevirt, J., "Development of eVTOL Aircraft For Urban Air Mobility At Joby Aviation," *78th Vertical Flight Society Annual Forum*, Fort Worth, Texas, May 10–12, 2022.

[23] Prouty, R. W., *Helicopter Performance, Stability, and Control*, Krieger Publishing Company, Inc., 1st ed., 1986.

[24] Gul, S. and Datta, A., "Whirl Flutter Test of the Maryland Tiltrotor Rig: Prediction and Validation," *AIAA SCITECH 2022 Forum*, San Diego, CA, May 2022.

[25] Leishman, J. G., *Principles of Helicopter Aerodynamics*, Cambridge University Press, 2nd ed., 2006.

[26] McCroskey, W. J., "The Phenomenon of Dynamic Stall," NASA-TM 81264, Mar. 1 1981.

[27] Leishman, J. G., "Dynamic stall experiments on the NACA 23012 aerofoil," *Experiments of Fluids*, Vol. 9, 1990, pp. 49–58.

[28] Datta, A., "X3D – A 3D Solid Finite Element Multibody Dynamic Analysis for Rotorcraft," *American Helicopter Society Technical Meeting on Aeromechanics Design for Vertical Lift*, San Francisco, CA, January 20-22, 2016.

[29] Gaffey, T. M. and Wernicke, K. G., "In-Plane Out-of-Plane Flapping Prop-rotor Frequency Decoupling," U.S. Patent 3,494,706, Feb. 10, 1970.

[30] Maisel, M. D., Giulianetti, D. J., and Dugan, D. C., "The History of the XV-15 Tilt Rotor Research Aircraft: From Concept to Flight," NASA SP- 2000-4517, 2000.

[31] Liu, Y., Liu, L., Liu, G., Wu, L., Liu, C., and Yue, Y., "Layout Method of Damping Material for Gearbox Based on Acoustic Contribution," *Xibei Gongye Daxue Xuebao/Journal of Northwestern Polytechnical University*, Vol. 37, No. 4, August 2019, pp. 757–766.

[32] Baksa, S. and Yourey, W., "Consumer-based Evaluation of Commercially Available Protected 18650 Cells," *Batteries*, Vol. 4, 3, pp. 1–8.

[33] Sheng, C. and Narramore, J. C., "Computational Simulation and Analysis of Bell Boeing Quad Tiltrotor Aero Interaction," *Journal of the American Helicopter Society*, Vol. 54, No. 4, October 2009, pp. 1–15.

[34] Atsushi, O., Satoko, A., Shota, N., Atsushi, K., Atsushi, K., and Masaru, U., "Flight control systems of a quad tilt rotor Unmanned Aerial Vehicle for a large attitude change," *IEEE International Conference on Robotics and Automation (ICRA)*, 2015.

[35] Gul, S. and Datta, A., "Aeroelastic Loads and Stability of Swept-Tip Hingeless Tiltrotors Toward 400 knots Flutter-Free Cruise," *77th Vertical Flight Society Annual Forum*, Virtual, May, 2021.

[36] Gul, S. and Datta, A., "Fundamental Understanding and Prediction of Loads and Stability of a Full-scale Hingeless Tiltrotor," *AIAA SciTech Forum*, Virtual, Jan., 2021.

[37] The Boeing Company - Vertol Division, "V/STOL Tilt Rotor Aircraft Study - Volume II: Preliminary Design of Research Aircraft," NASA CR 114438, 1972.

[38] de Almeida, O., Souza, P. R. C., and da Silveira, B., "Numerical Investigation of a NACA Air Intake for a Canard Type Aircraft," *International Journal of Advanced Engineering Research and Science (IJAERS)*, Vol. 4, 2017.

[39] Haynes, D. and Smith, A., "Compact Tiltrotor Pylon-Conversion Actuation System," U.S. Patent 7,913,947 B2, Mar. 29 2011.

[40] Raymer, D. P., *Aircraft Design: A Conceptual Approach*, AIAA Education Series, AIAA, 3rd ed., 1999.

[41] Mainuddin, A., Abubakar, S. S., Mohammad, F. S., Abdul, F. B., and Jagadeesh, B., "Preliminary Design of Aircraft Landing Gear Strut," *International Journal of Innovative Research in Technology*,

Vol. 4, 2018.

[42] Xin, M., "Unified nonlinear optimal flight control and state estimation of highly maneuverable aircraft," *Aerospace Science and Technology*, Vol. 37, Aug. 2017, pp. 70–80.

[43] Lombaerts, T., Kaneshige, J., and Feary, M., "Control Concepts for Simplified Vehicle Operations of a Quadrotor eVTOL Vehicle," *AIAA Aviation 2020 Forum*, Virtual, Jun. 15–19, 2020.

[44] Edmunds, R. and Vangaasbeek, J., "Pilot modeling and control augmentation for the XV-15 in in-ground-effect hover," *17th Fluid Dynamics, Plasma Dynamics, and Lasers Conference*, p. 1892.

[45] Kleinhesselink, K. M., *Stability and Control Modeling of Tiltrotor Aircraft*, Master's thesis, The Graduate School of the University of Maryland, College Park, College Park, MD, August 2007.

[46] Frost, C. R., Hindson, W. S., Moralez, E., and Tucker, G. E., "Design and Testing of Flight Control Laws on the RASCAL Research Helicopter," *American Institute of Aeronautics and Astronautics*, 2009.

[47] Shastry, A., Datta, A., and Chopra, I., "Feature-Based Vision For Stochastic Motion Tracking Under Partial Occlusion," *78th Vertical Flight Society Annual Forum*, Fort Worth, Texas, May 10–12, 2022.

[48] Society, N. M. S.

[49] Kessler, G. C., "Aviation Cybersecurity: An Overview," Aug. 15 2018.

[50] Johnson, D. P., "Civil Aviation and Cybersecurity," 2013.

[51] Brooks, T., Pope, D., and Marcolini, M., "Airfoil Self-Noise and Prediction," NASA-RP 1218, Jul. 1989.

[52] Yuan, C., Bergsma, O., and Beukers, A., "Sound Transmission Loss Prediction of the Composite Fuselage with Different Methods," *Applied Composite Materials*, Vol. 19, 865-883, Jan. 28, 2012.

[53] Dilhara, J., Jung, Y., and Baeder, J., ""CFD andAeroacoustic Analysis of Wingtip-Mounted Propellers," *Vertical Flight Society 76th Annual Forum Proceedings*, Virtual, October, 2020.

[54] McCroskey, W. J., Spalart, P. R., Laub, G. H., Maisel, M. D., and Maskew, B., "Airloads on Bluff Bodies, with Application to the Rotor-Induced Downloads on Tilt-Rotor Aircraft," NASA-TM 84401, Sept. 1983.

[55] Felker, F. F., Shinoda, P. R., Heffernan, R. M., and Sheehy, H. F., "Wing Force and Surface Pressure Data from a Hover Test of a 0.658-Scale V-22 Rotor and Wing," *NASA-TM*, Vol. 102244, Feb. 1, 1990.

[56] Ng, W. and Datta, A., "Hydrogen Fuel Cells and Batteries for Electric-Vertical Takeoff and Landing Aircraft," *Journal of Aircraft*, Vol. 56, No. 5, Oct. 2019, pp. 1–18.

[57] Maisel, M. D., Borgman, D. C., and Few, D. D., "Tilt Rotor Research Aircraft Familiarization Document," NASA-TM x-62407, Jan. 1975.

[58] Scott, R., "A Design-Centric Evaluation of Multi-Fidelity Cost Modeling Approaches," *Fourty-Fourth Europeon Rotorcraft Forum*, Delft, The Netherlands, 2018.

[59] Harris, F. D., "Introduction to Autogyros, Helicopter, and Other V/STOL Aircraft," NASA-SP 2012-215959, Oct 2012.